

TECHNISCHE UNIVERSITÄT MÜNCHEN

Fakultät für Chemie

Lehrstuhl für Technische Chemie II

**Pore entrance kinetics in nano-sized  
ZSM-5 zeolites**

Martin Baumgärtl

Vollständiger Abdruck der von der Fakultät für Chemie

Der Technischen Universität München zur Erlangung des akademischen Grades eines

**Doktors der Naturwissenschaften (Dr. rer. nat.)**

genehmigten Dissertation.

Vorsitzender: Prof. Dr.-Ing. Kai-Olaf M. Hinrichsen

Prüfer der Dissertation:

1. Prof. Dr. Johannes A. Lercher
2. Prof. Dr. Ulrich K. Heiz

Die Dissertation wurde am 26.03.2021 bei der Technischen Universität München eingereicht und durch die Fakultät für Chemie am 26.07.2021 angenommen.



*“An expert is a person who has made all the mistakes.  
that can be made in a very narrow field.”*

*— Niels Bohr*



# Acknowledgements

Over the course of the last couple years, I have experienced the help of a great number of people, without whom, this thesis would not have been possible. In the following lines, I want to take the opportunity to express my gratitude to some of the most important ones.

First of all, I want to thank Prof. Dr. Johannes A. Lercher for the opportunity to be part of his group. Johannes, thank you for your guidance and support throughout the thesis. You gave me the scientific freedom to follow my own ideas and supported me with your expertise whenever needed. Thank you for providing the scientific infrastructure and financial freedom to purchase whatever I needed (although I was quite minimalistic in that regard). I especially want to thank you for the numerous opportunities to visit national/international conferences, which is not a given in other research groups. I will never forget my trip to IZC in Perth.

I want to express my sincere gratitude to Apl. Prof. Dr. Andreas Jentys for his support over the last years. Andy, thank you for putting me on one of your favorite projects, for your time discussing scientific data and for correcting my manuscripts. Your opinion was always very much appreciated. It was always worth coming to your office, not only concerning scientific input, but also for interesting talks, e.g., the evolution of data storage from punched cards to SSDs.

Moreover, I want to thank my colleagues and friends I found throughout the years at TC2. Thanks for (non-)scientific discussions, for cheering me up in stressful moments and for all kinds of activities outside! the lab. I enjoyed working with each one of you: Ferdinand Vogelgsang, Manuel Weber-Stockbauer, Felix Kirchberger, Teresa Schachtl, Verena Höpfl, Andreas Ehrmaier, Daniel Melzer, Roland Weindl, Edith Berger, Lara Milakovic, Laura Löbbert, Yang Zhang, Wanqiu Luo, Christoph Denk, Takaaki Ikuno, Ruixue Zhao, Alexander Wellmann, Niklas Pfriem, Mirjam Wenig, Insu Lee, Martina Aigner, Lennard Wahl, Xi Chen, Guanhua Cheng, Philipp Fischer, Fuli Deng, Rachit Kare, Lingli Ni, Jakub Pazdera, Karen Resende, Aimen Shahpal, Lei Tao, Yong Wang, Iris Yu and Wei Zhang.

I also want to thank the Bachelor (Michael Huber and Niklas Pflaum) and Master students (Florian Zand) I supervised during my dissertation time. Thank you for your work and dedication to the project.

I want to express my gratitude to the administrative and technical staff at TC2. To Steffi and Katja for their overview on and management of all sorts of appointments. To Bettina for conjuring contracts, paying bills, and correcting my dilettantishly filled forms. To Andreas for his patience with my ancient setup, upgrading it to USB 1.1 and nostalgic talks about the advantages of Floppy Discs. To Martin for analyzing my samples by AAS and to Xaver, for technical support in every respect.

Finally, I am deeply grateful to my parents Ingrid and Helmut, to my sister Magdalena and my brother Korbinian for their support and encouragement throughout my entire life. Thank you for always standing by my side, listening to my problems, and giving good advice. This thesis would not have been possible without you!

# Abbreviations

<b>Acronym</b>	<b>Description</b>
AHFS	Ammonium hexafluorosilicate
a.u.	Arbitrary units
BAS	Brønsted acid site, Bridging hydroxyl group
BBU	Basic building unit
BEA	Zeolite Beta
BET	Brunnauer, Emmet, Teller
CBB	Composite building blocks
FAU	Faujasite
FCC	Fluidized catalytic cracking
FER	Ferrierite
IR	Infrared
IUPAC	International Union of Pure and Applied Chemistry
IZA	International Zeolite Association
LC	Large crystal
LAS	Lewis acid sites
MFI	Mobile number five (Zeolite)
MOR	Mordenite (Zeolite)
MTO	Methanol to olefins
NMR	Nuclear magnetic resonance
PO	Pore openings
PTFE	Polytetrafluoroethylene
SBU	Secondary building unit
r.d.s.	Rate determining step
SEM	Scanning electron microscopy
T-atom	Tetrahedrally coordinated atom
T'BP	Tri-tert-butyl phosphine
ZSM-5	Zeolite Socony Mobile 5

# Nomenclature

<b>Letter</b>	<b>Description</b>	<b>[Unit]</b>
$A_{crystal}$	Surface area of the crystallite	[m <sup>2</sup> ]
$A_{unit\ cell}$	Surface area of the unit cell	[m <sup>2</sup> ]
$A_{FR}$	Amplitude of FR experiment	[a.u.]
$c_{sat}$	Saturation concentration	[mol·g <sup>-1</sup> ]
$c_{eq}$	Equilibrium concentration	[mol·g <sup>-1</sup> ]
$D_{Kn,eff}$	Effective Knudsen diffusivity	[m <sup>2</sup> ·s <sup>-1</sup> ]
$D_{vis}$	Diffusivity in viscous flow	[m <sup>2</sup> ·s <sup>-1</sup> ]
$D_{Kn}$	Knudsen diffusivity	[m <sup>2</sup> ·s <sup>-1</sup> ]
$D$	Diffusion coefficient	[m <sup>2</sup> ·s <sup>-1</sup> ]
$d_p$	Pore diameter	[m]
$j$	Fickian flux	[mol·m <sup>-2</sup> ·s <sup>-1</sup> ]
$F_{SF}$	Mobility factor for single file diffusion	[mol·m <sup>-2</sup> ·s <sup>-1</sup> ]
$G^\circ$	Gibbs free energy	[kJ·mol <sup>-1</sup> ]
$H^\circ$	Standard enthalpy	[kJ·mol <sup>-1</sup> ]
$H_{app}^\ddagger$	Apparent transition state enthalpy	[kJ·mol <sup>-1</sup> ]
$H_{true}^\ddagger$	True transition state enthalpy	[kJ·mol <sup>-1</sup> ]
$f$	Frequency	[s <sup>-1</sup> ]
$K$	Equilibrium constant	[-]
$k_B$	Boltzmann constant	[J·K <sup>-1</sup> ]
$k_{+1}$	Forward equilibrium constant (1. Order)	[s <sup>-1</sup> ]
$k_{-1}$	Backward equilibrium constant (1. Order)	[s <sup>-1</sup> ]
$k_{ads}$	Rate constant for adsorption process (1. Order)	[s <sup>-1</sup> ]
$k_{des}$	Rate constant for desorption process (1. Order)	[s <sup>-1</sup> ]
$l$	Distance between two sorption sites	[m]
$M$	Molecular weight	[g·mol <sup>-1</sup> ]
$m$	Mass	[g]
$N_{open./crystal}$	Number of pore openings per crystallite surface	[-]
$p_0$	Standard partial pressure	[Pa]

$p_A$	Partial pressure of component A	[Pa]
$q_{rot}$	Rotational partition function	[-]
$q_{vib}$	Vibrational partition function	[-]
$R$	Ideal gas constant	[J·mol <sup>-1</sup> ·K <sup>-1</sup> ]
$r_{ads}$	Adsorption rate	[mol·g <sup>-1</sup> ·s <sup>-1</sup> ]
$r_{des}$	Desorption rate	[mol·g <sup>-1</sup> ·s <sup>-1</sup> ]
$r_{coll}$	Collision rate	[mol·m <sup>-2</sup> ]
$S^\circ$	Standard entropy	[J·mol <sup>-1</sup> ·K <sup>-1</sup> ]
$S_{BET}$	BET surface area	[m <sup>2</sup> ·g <sup>-1</sup> ]
$T$	Temperature	[K]
$t$	Time	[s]
$\langle u \rangle$	Mean gas velocity	[m·s <sup>-1</sup> ]
$V$	Volume	[m <sup>3</sup> ]
$V_{ads}$	Volume adsorbed	[m <sup>3</sup> ]
$V_{mono}$	Volume of a monolayer	[m <sup>3</sup> ]

<b>Symbol</b>	<b>Description</b>	<b>[Unit]</b>
$\alpha$	Sticking coefficient	[-]
$\delta_{in}$	Characteristic FR in phase function	[-]
$\delta_{out}$	Characteristic FR out phase function	[-]
$\varepsilon$	surface permeability	[m·s <sup>-1</sup> ]
$\varepsilon_p$	Porosity factor	[-]
$\eta$	Viscosity	[kg·m <sup>-1</sup> ·s <sup>-1</sup> ]
$\eta_{FR}$	Frequency response transport parameter	[-]
$\theta$	Site coverage	[-]
$\lambda$	Mean free path of a molecule	[m]
$\tau_p$	Tortuosity factor	[-]
$\tau_j$	Mean time between two succeeding jumps	[s]
$\tau_{surf}$	Mean residence time of a molecule on surface	[s]
$\varphi$	Phase lag	[-]
$\omega$	Angular frequency	[s <sup>-1</sup> ]



## Abstract

Transport under reactive and non-reactive conditions during xylene gas phase isomerization on MFI is influenced by the coverage of the external surface. The rate determining pore entrance rate of xylenes correlates directly with the coverage of the transported molecules on the external surface. For mixtures of *p*- and *m*- or *o*-xylene, the transport rate is reduced by the competitive adsorption of *m*-xylene at the pore entrance. The higher adsorption constant of *m*-xylene and lower barrier to enter the pore reduces hindrance of the *p*-xylene adsorption rate with increasing temperatures.

## Kurzzusammenfassung

Der Transport unter reaktiven und nicht reaktiven Bedingungen bei der Gasphasenisomerisierung von Xylol auf MFI wird durch die Bedeckung der äußeren Oberfläche beeinflusst. Die Poreneingangsrate von Xylenen korreliert direkt mit deren Bedeckung auf der äußeren Oberfläche. Bei Mischungen von *p*- und *m*- oder *o*-Xylol wird die Transportrate durch die Adsorption von *m*-Xylol am Poreneingang reduziert. Die höhere Adsorptionskonstante von *m*-Xylol und die geringere Barriere zum Eintritt in die Pore reduziert die Behinderung der *p*-Xylol-Adsorptionsrate mit steigenden Temperaturen.

# Table of Contents

Acknowledgements .....	I
Abbreviations.....	III
Nomenclature.....	IV
Abstract.....	VII
Kurzzusammenfassung.....	VII
Table of Contents .....	VIII
<b>1. Zeolites in General.....</b>	<b>1</b>
1.1. Composition and crystal structure .....	1
1.2. Zeolite acidity .....	5
1.3. Confinement effects in zeolites .....	7
1.3.1. Structure induced selectivity .....	7
1.3.2. Reactivity and acid strength.....	8
1.4. Framework type MFI .....	11
<b>2. Fundamentals of Sorption.....</b>	<b>13</b>
2.1. Langmuir theory .....	14
2.2. Sorption kinetics – sticking coefficient.....	20
2.3. Multilayer adsorption .....	21
2.4. Site characterization by adsorption .....	23
2.4.1. Acidic sites.....	23
2.4.2. Interaction with substrate molecules.....	24
<b>3. Transport in Porous Materials .....</b>	<b>25</b>
3.1. Molecular diffusion .....	27
3.2. Knudsen diffusion.....	28
3.3. Viscous flow .....	29
3.4. Surface and pore diffusion .....	30
3.5. Single file diffusion .....	31
3.6. Surface barriers .....	32
<b>4. Applied Methods for Transport Measurements .....</b>	<b>34</b>

4.1.	Fast time-resolved infrared spectroscopy.....	34
4.2.	Frequency response.....	39
4.3.	Desorption curves.....	42
5.	Scope of the Thesis.....	44
6.	Understanding Transport Steps in Xylene Mixtures in ZSM-5 Zeolites .....	45
6.1.	Introduction .....	46
6.2.	Experimental section.....	48
6.2.1.	Materials.....	48
6.2.2.	Physicochemical characterization.....	48
6.2.3.	Concentration of pore openings .....	49
6.2.4.	Selective deposition of <i>m</i> -xylene .....	50
6.2.5.	Fast time-resolved IR spectroscopy .....	51
6.2.6.	Frequency response measurements.....	52
6.3.	Results and discussion .....	54
6.3.1.	Physicochemical characterization.....	54
6.3.2.	Concentration of pore openings .....	54
6.3.3.	Fast time-resolved IR spectroscopy .....	55
6.3.4.	Frequency response measurements.....	57
6.4.	Conclusion .....	67
6.5.	Supporting information .....	68
6.6.	Associated content.....	74
7.	Influence of Acid Sites on Xylene Transport in MFI Type Zeolites.....	75
7.1.	Introduction .....	76
7.2.	Experimental section.....	77
7.2.1.	Materials.....	77
7.2.2.	Physicochemical characterization.....	77
7.2.3.	Fast time-resolved IR spectroscopy .....	79
7.2.4.	Determination of pore entrance rates .....	80
7.3.	Results and discussion .....	81
7.3.1.	Physicochemical characterization.....	81
7.3.2.	Concentration of pore openings .....	81
7.3.3.	<i>p</i> -Xylene sorption .....	82
7.3.4.	<i>m</i> -Xylene isotherms for sorption on external surface.....	83

7.3.5.	<i>p</i> -Xylene transport.....	86
7.4.	Conclusion.....	92
7.5.	Supporting information.....	93
7.6.	Associated content.....	97
<b>8.</b>	<b>Surface Effects determining Transport in Binary Xylene Mixtures.....</b>	<b>98</b>
8.1.	Introduction.....	99
8.2.	Experimental section.....	101
8.2.1.	Materials.....	101
8.2.2.	Physicochemical characterization.....	101
8.2.3.	Fast time-resolved IR spectroscopy.....	102
8.3.	Results and discussion.....	104
8.3.1.	Physicochemical characterization.....	104
8.3.2.	Concentration of pore openings.....	105
8.3.3.	Binary sorption of xylenes.....	105
8.4.	Conclusion.....	117
8.5.	Supporting information.....	118
8.6.	Associated content.....	120
<b>9.</b>	<b>Concluding Summary.....</b>	<b>121</b>
<b>10.</b>	<b>Abschließende Zusammenfassung.....</b>	<b>123</b>
	References.....	125
	List of Figures.....	139
	List of Tables.....	145

# 1. Zeolites in General

## 1.1. Composition and crystal structure

Zeolites are crystalline, microporous tectosilicates, primarily consisting of  $\text{SiO}_4$  tetrahedrons (basic building unit, BBU). [1] These BBUs are interconnected by corner sharing oxygen atoms to form polyhedrons, (secondary building units, SBU, Figure 1.1), which then arrange into larger, structurally well defined, composite building units (CBUs). Combining various CBUs gives access to a wide range of three-dimensional crystal structures with different pore sizes and locations. Currently the International Union of Pure and Applied Chemistry (IUPAC) and the International Zeolite Association (IZA) have accepted 252 structurally different zeolites and assigned a three-letter code to each structure. [2, 3] However, these are only a subsection of the huge number of theoretically feasible structures exceeding the number of observed structures by at least two orders of magnitude. [4] Figure 1.2 shows a selection of widely used zeolite framework types and the CBUs they consist of.

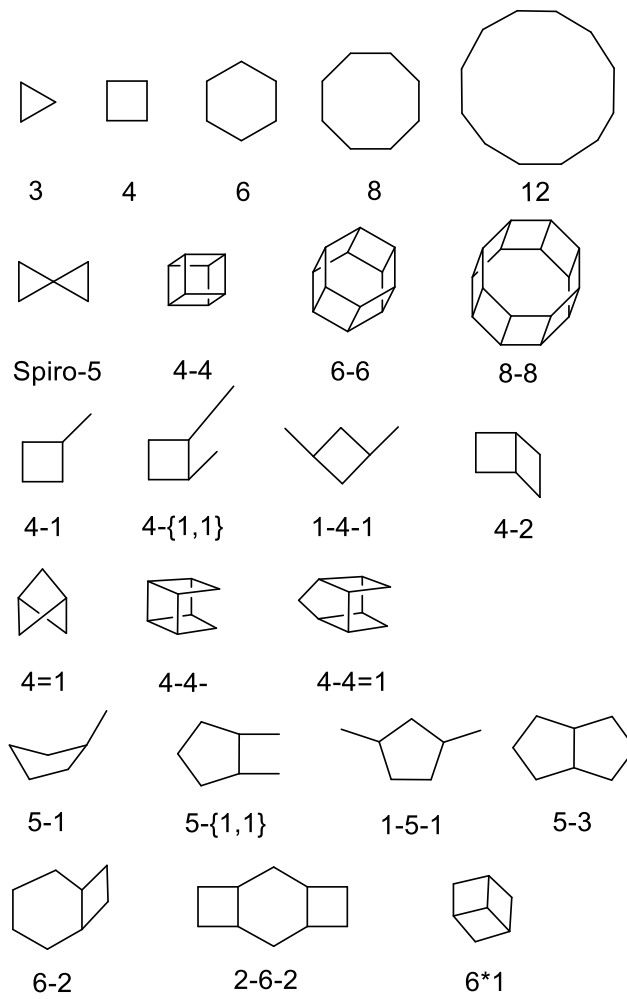


Figure 1.1: Selection of secondary building blocks adapted from Baerlocher et al.  
 [1] The corners thereby represent T-atoms, the bonds oxygen bridges.

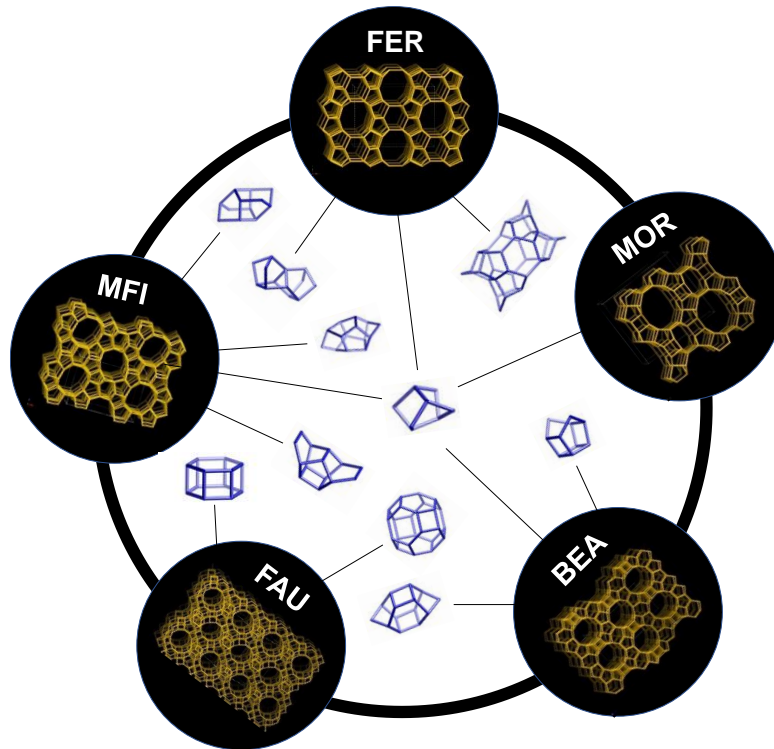


Figure 1.2: Selection of industrially important zeolite framework types and the composite building blocks they are built of. [2, 3]

Having a crystalline structure, zeolites feature a structurally defined pore size distribution, usually in the range of aromatic and aliphatic hydrocarbons. [5] Therefore, zeolites are ideally suited for acting as selective adsorbents and shape selective catalysts for applications where the selectivity is determined by the pore geometry. The pore diameter and the size of the intersections is defined by the number of tetrahedrally coordinated atoms (T-atoms) in one ring. Depending on the framework type, rings between 4 and 14 T-atoms are common, often referred to as 4-14 membered rings (Figure 1.3). Nevertheless, also larger pore sizes are feasible with 20 and 24 membered rings (SYT, CLO and IFU structures). [1]

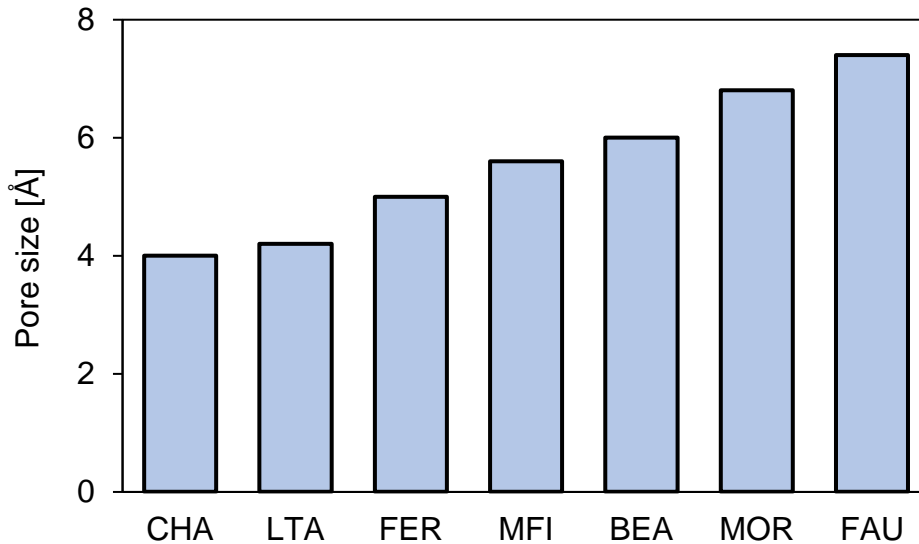


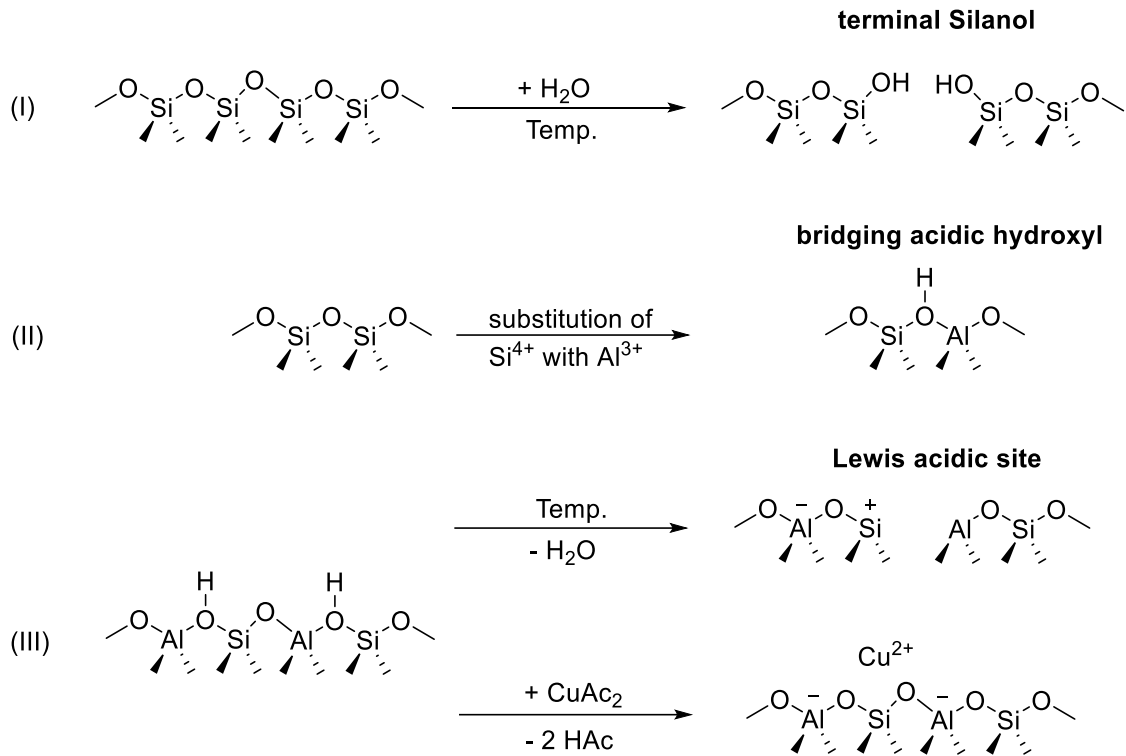
Figure 1.3: Average pore size of commonly used zeolite frameworks. [2, 3, 6, 7]

Zeolites are used as catalysts in various chemical processes due to their physical and chemical properties such as mechanical and thermal stability, high surface area, shape selectivity and an entropically controlled reaction environment. The broad range of applications for zeolites is based on the vast variety of well-defined structure types. [1] By choosing the right zeolite structure and composition, key parameters such as pore size and acid site concentration can be chosen according to their field of application. Common zeolite catalyzed processes are fluidized catalytic cracking (FCC) [8-10], methanol to olefins (MTO), [11-13] alkylation [14, 15] and isomerization reactions [16-18] as well as selective reduction of  $\text{NO}_x$  in exhaust gas of Diesel engines. [19, 20] Using zeolite membranes further allows an effective separation of gas mixtures. [21, 22] Other applications of micro- and mesoporous materials are as insulation, [23-25] vibration reduction [26] or filtration systems [27]. Due to their economic and environmental advantages compared to their traditionally used counterparts, porous materials are well established as catalysts, catalyst supports and sorbents particularly within the chemical industry. [28-31]

## 1.2. Zeolite acidity

Brønsted or Lewis acidic sites are the catalytically active sites for a large range of reactions involving zeolites. [32] Acidity in zeolites is created by isomorphous substitution of the  $\text{Si}^{4+}$  atoms by  $\text{Al}^{3+}$  in the framework. The resulting negative charge is compensated by an organic or inorganic cation. [33, 34] Brønsted acid sites (BAS, proton donor) are generated when the negative charge is compensated by a proton (Scheme 1.1 (II)). To form Lewis acid site (LAS, electron acceptor), the negative charge must be either balanced by an alkali or earth alkali ion, or the dehydration of a BAS (Scheme 1.1 (III)). Elevated temperatures can also lead to the removal of aluminum from the framework, which is then deposited in the zeolite channels as octahedrally coordinated aluminum oxide. [35] The effective acid strength of the material depends on the chemical composition and structure of the zeolitic material. [36, 37] Due to the higher electronegativity of silicon compared to aluminum, stronger BAS will occur on isolated  $\text{AlO}_4$ -tetrahedra. Therefore, high BAS concentrations tend to decrease the strength of the individual sites compared to isolated  $\text{SiOHAl}$  sites. [5, 38, 39]

The composition of zeolites can in general be described by the formula  $\text{M}_{x/m}[(\text{AlO}_2)_x(\text{SiO}_2)_y](\text{H}_2\text{O})_w$ . Herein,  $m$  represents the charge of the neutralizing cation and  $w$  the number of water atoms present. The Si/Al ratio is given by  $y/x$ . The acid site concentration can be set by the Si/Al ratio, with an upper limit for the aluminum content defined by the stability of the regarding framework type. As the direct linkage of Al atoms connected as Al-O-Al is not stable (Loewenstein's rule), the lower limit for the Si/Al ratio is one. [40] However, some framework types suffer from stability issues at much lower aluminum contents. For example, MFI type frameworks are known to be unstable below Si/Al=10. [41]

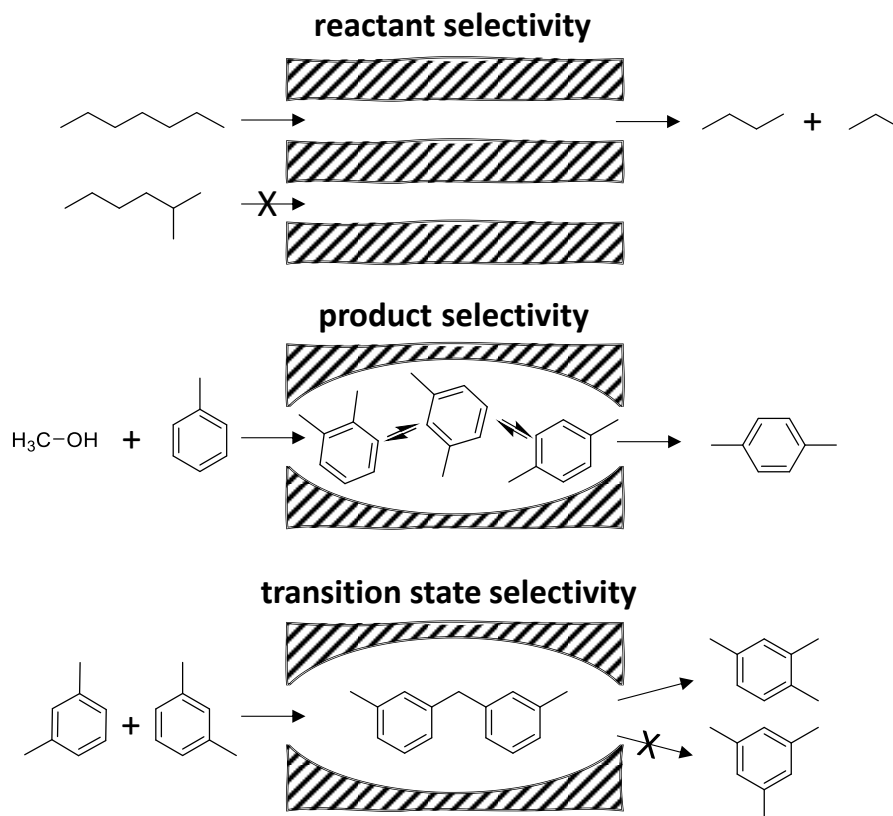


Scheme 1.1: Formation of (I) terminal silanol groups by hydration under elevated temperatures, [42] (II) bridging hydroxyl groups (SiAlOH, BAS) by substitution of  $\text{Si}^{4+}$  with  $\text{Al}^{3+}$  and charge compensation by a proton. Formation of Lewis acid sites (III) can occur at elevated temperatures via dehydration or charge compensation with an alkali or earth alkali ion. [43]

## 1.3. Confinement effects in zeolites

### 1.3.1. Structure induced selectivity

The possibility to introduce selectivity by confined pore space is one of the main advantages for zeolites and separates them as catalysts from other porous materials. The ability for shape selective catalysis can be attributed to three different effects (Scheme 1.2): A) sterically constrained substrate is excluded to enter the catalytic site due to the narrow pore diameter. This principle is called reactant selectivity and is utilized in dewaxing processes as well as for molecular sieves and membranes to separate substrate mixtures. [44-46] B) Product selectivity, in which bulky products, formed inside the pore network, cannot leave the pores due to sterical reasons. Typical examples are xylene alkylation and isomerization reactions, [5, 47, 48] where bulky meta- and ortho- isomers are restrained from leaving the pores, while the kinetically smaller *p*-xylene can depart easily. C) When certain products are favored over others due to the formation of a sterically less demanding transition state in the confined environment of the pore network, transition state selectivity is applied. This principle is utilized in transalkylation reactions.



Scheme 1.2: Schematic illustration of different shape selectivities induced by zeolite pores.

### 1.3.2. Reactivity and acid strength

Besides excluding molecules from the pores space and controlling transition states by the pore geometry, the effective acid strength as well as the reaction rate is affected by the confined environment of the pore space. Sorption of molecules on a surface relies on the interplay between repulsive short range (Pauli type) and attractive long range (van der Waals type) interactions (Lennard-Jones potential). For physisorption of hydrocarbons on a flat surface, larger molecules will in general adsorb stronger due to building up van der Waals forces over a larger area. However, due to the limited space and surface curvature of the internal surface for nanoporous materials, large molecules may not be able to find the energetic minimum between attractive and repulsive interactions and therefore be restricted or even excluded from the pores. Consequently, molecules having the best “match” within the pore space will adsorb preferentially. [49-51] Such an optimized system will enhance the reaction rate, as shown by

Derouane et al. By plotting the turnover frequencies for *n*-pentane cracking on different zeolite frameworks against pore size, an optimal pore diameter in the range of *n*-pentane (5.8 - 6.0 Å) was observed (Figure 1.4). [49, 50]

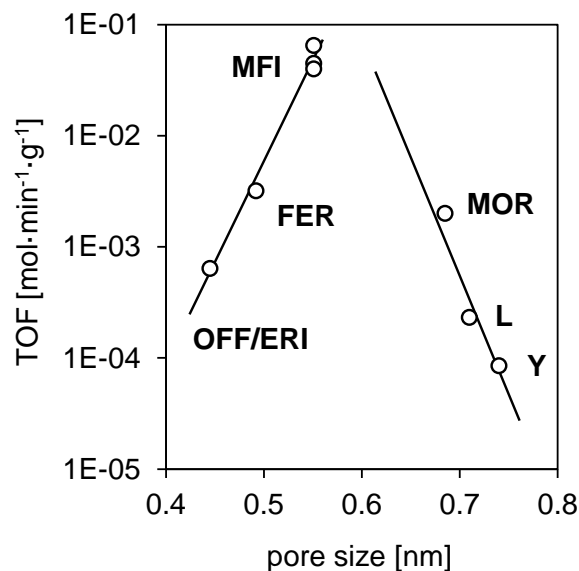


Figure 1.4: Turnover frequencies for *n*-pentane cracking on various zeolites as a function of pore size. Data adapted from [49].

In the same way, the interaction of molecules with acidic sites located in the pore space can be restricted by the interplay of pore geometry and molecule size, leading to a reduced effective acidity of the zeolitic material in respect to that molecule. This effect can be observed from shifts of hydroxy bond vibrations during adsorption via infrared spectroscopy. The interaction of a molecules with the proton of a hydroxy group will weaken the O-H bond and shift the absorbance of the observed stretching vibration to a lower wavenumber (lower energy). A stronger interaction will thereby lead to a stronger perturbation of the bond and to a larger shift in the infrared spectra. Due to sterical constraints for larger molecules in the pore space, hydroxy groups located inside the pores (mainly SiOHAl groups for zeolites) observe a smaller shift than would be expected for non-hindered adsorption on externally accessible sites. This size effect can be illustrated in a Bellamy-Hallam-William plot, which correlates the shift for externally accessible hydroxyl (SiOH) and internal (SiOHAl) groups for the adsorption of probe molecules (Figure 1.5). [52-54]

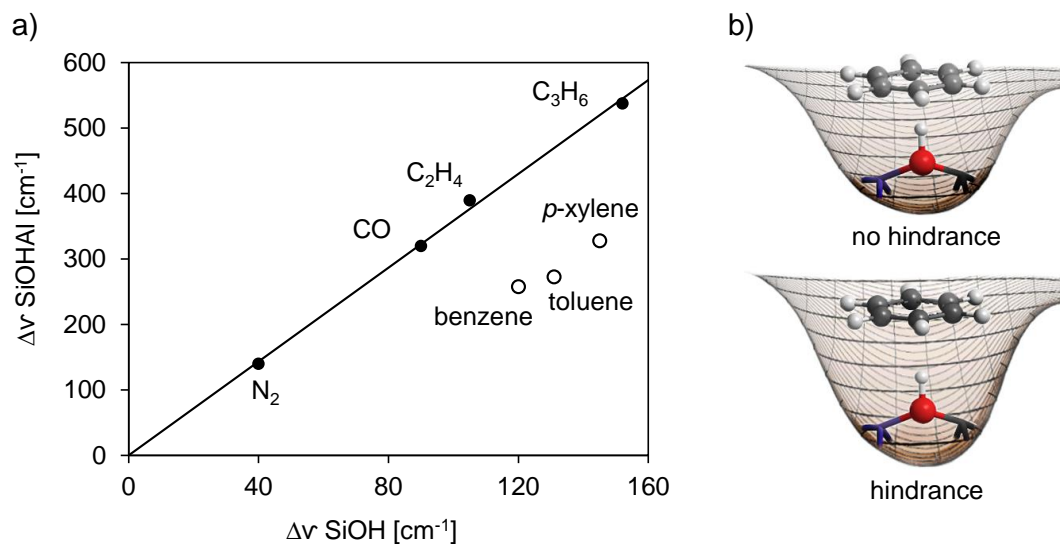


Figure 1.5: a) Shift of OH stretching vibrations of SiOH and SiOHAl (HZSM-5) for adsorption of various molecules. Summarized data from [52, 54]. b) Sterical constraints of pore influencing distance of interaction between benzene and SiOHAl group.

## 1.4. Framework type MFI

The focus of this thesis is based on transport studies in MFI type zeolites. Therefore, a closer look at this framework type is given in this section. In the early 1970s, the first synthesis of this framework structure under the name ZSM-5 was described by W. Haag at the Mobile Oil Corporation (Zeolite Socony Mobil-5). [55]

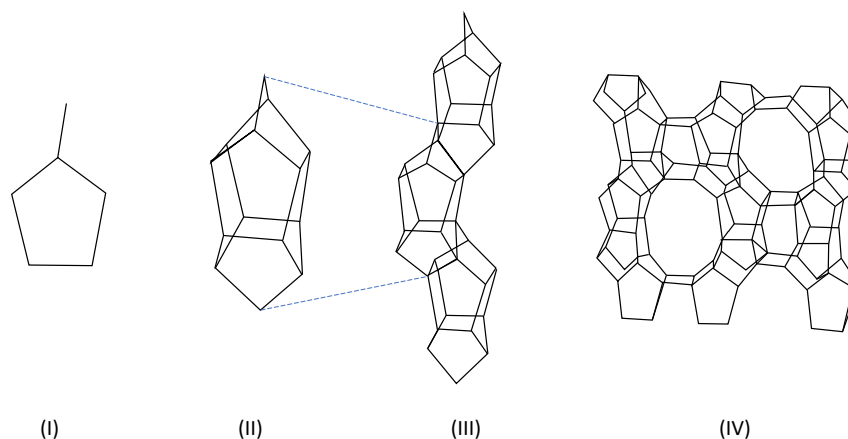


Figure 1.6: The MFI framework is built of (I) Type 5-1 SBUs, which form larger composite building blocks (II). Interconnection of these CBBs results in (III) pentasil chains and (VI) layers of tetrahedra. [56]

The unit cell consists of 196 T-atoms (Figure 1.6) forming an orthorhombic structure with a 3-dimensional channel system. [57] Out of these 196 T-sites, 12 distinct sites can be distinguished. [58, 59] Within the structure, two channel types, straight and sinusoidal channels, oriented perpendicular to each other are formed (Figure 1.7). Both channels consist of 10 membered rings with similar size. While the slightly elliptical straight channel has a cross section of 0.53 x 0.56 nm, the dimensions of the sinusoidal channel are 0.51 x 0.55 nm. At the crossing points of straight and sinusoidal channels, larger intersections with a diameter of 0.89 nm are formed. [1, 60]

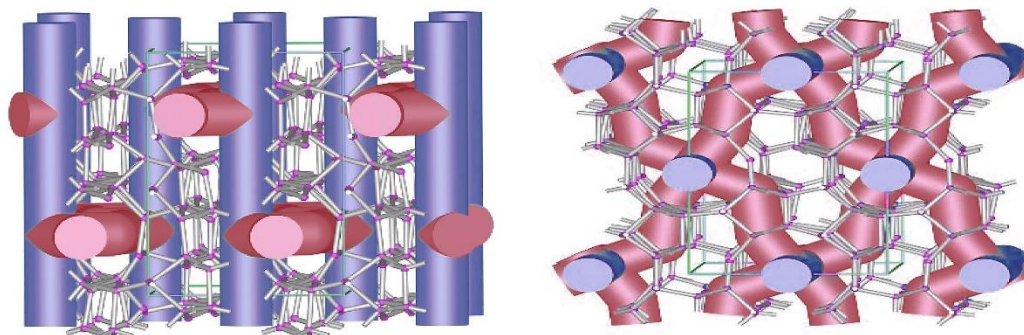


Figure 1.7: Schematic representation of the MFI framework with straight (blue) and sinusoidal (red) channel. [56]

While originally developed for the selective production of synthetic gasoline, [61] the MFI framework was rapidly applied for other shape selective reactions such as alkylation and isomerization reactions. [17, 62] Nowadays, MFI structured zeolites are one of the most applied materials in the petrochemical industry, arising from their excellent thermal stability and their pore size in the range of aromatic hydrocarbons. [36] Besides Al substituted materials, purely silicious MFI (Silicalite-1) is used as membrane for separation and purification of organic mixtures. [63, 64] The possibility to incorporate other three and four valent heteroatoms into the framework offers the potential of designing zeolites for novel catalytic applications. Titanium incorporated Silicalite-1 (TS-1) is a highly efficient catalysts for selective oxidations, such as epoxidation of alkenes, ammoxidation of ketones, and hydroxylation of phenols. [65-67] Ga exchanged HZSM-5 zeolites are known to show high selectivity to aromatics in the catalytic conversion of olefins and paraffins. [68-70] Copper and Iron exchanged HZSM-5 are excellent catalysts for the selective catalytic reduction (SCR) of  $\text{NO}_x$  by ammonia, which plays a major role in emission reduction for transportation. [71, 72]

## 2. Fundamentals of Sorption

The binding of a molecule (adsorbate) from the vapor or liquid phase onto a solid surface (adsorbent) is called adsorption. This surface phenomenon is in general attributed to an attractive interaction of the adsorbate with the solid surface, which competes with the cohesive energy of the adsorbate itself. [73] Thermodynamically, an exothermic adsorption process is required to compensate for the reduction in freedom of motion of adsorbing molecules (loss in entropy) to obtain an exergonic driving force (negative  $\Delta G^\circ$ ). Depending on the nature of interaction between adsorbent and adsorbate, a differentiation between physisorption (by London–van der Waals forces) and chemisorption (chemical bonding forces) is common. While physisorption is non-specific for a surface, chemisorption is a site-specific interaction. Although, this differentiation is useful for classifying sorption processes according to their binding strength, a sharp distinction between physisorption and chemisorption is not always possible. [74] When a substance in gas phase is adsorbed on a solid surface or its pore space, the uptake depends on the number of adsorption sites, the temperature, the partial pressure of the vapor and the strength of interaction between vapor and solid surface. For a constant temperature, the correlation between uptake and pressure can be expressed as sorption isotherm. [75, 76]

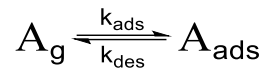
Investigating the sorption of molecules on a surface not only gives access to a variety of parameters characterizing the nature of the surface itself, but also providing information about the interaction of the surface with substrate molecules. By choosing suitable sorption molecules and conditions in combination with analytical methods like infrared spectroscopy or gravimetric measurements, a great variety of information like surface area, pore volume, sorption site concentrations and strength can be obtained.

## 2.1. Langmuir theory

The Langmuir adsorption theory was published by Irving Langmuir in 1916 [77] after studying the adsorption of gases on metal surfaces. The model is widely applied for sorption equilibria between gas phase molecules and solid surfaces. The model is based on the following fundamental assumptions: [75]

- a) Only one molecule can adsorb on one sorption site, resulting in a monolayer on the surface at full coverage.
- b) Adsorption is equally likely on each sorption site and does not depend on the surface coverage. Thus, the heat of adsorption (and therefore also the rate constants for adsorption and desorption process) stays constant throughout the whole sorption process.
- c) No molecule – molecule interactions are absent. Therefore, the probability for a molecule to desorb is independent of the surface coverage and the gas pressure.

Considering an equilibrated state of a substance A between gas phase and adsorbed state:



at equilibrium, the rates of adsorption and desorption are equal. The rate constants are denoted  $k_{ads}$  and  $k_{des}$  for the adsorption and desorption process, respectively. [32] In this case, the rate of adsorption on the surface is a function of the normalized partial pressure  $p_A = \frac{p}{p_0}$ , the adsorption rate constant  $k_{ads}$  as well as the concentration of free sorption sites  $(1 - \theta_A)c_{A,sat}$ . [75]

$$r_{ads} = k_{ads} \cdot p_A \cdot (1 - \theta_A) \cdot c_{A,sat} \quad (2.1)$$

As no molecule – molecule interactions of species A are considered in the Langmuir model, the desorption rate linearly correlates with the surface concentration of A and the desorption rate constant.

$$r_{des} = k_{des} \cdot \theta_A \cdot c_{A,sat} \quad (2.2)$$

Considering the equilibrated state,  $r_{ads} = r_{des}$  leading to Equation 2.3

$$k_{ads} \cdot p_A \cdot (1 - \theta_A) \cdot c_{A,sat} = k_{des} \cdot \theta_A \cdot c_{A,sat} \quad (2.3)$$

Solving for the surface coverage:

$$\theta_A = \frac{k_{ads} \cdot p_A}{k_{des} + k_{ads} \cdot p_A} \quad (2.4)$$

Introducing the equilibrium constant  $K_A = \frac{k_{ads}}{k_{des}}$  leads to the classic expression of the Langmuir formalism (Figure 2.1):

$$\theta_A = \frac{K_A \cdot p_A}{1 + K_A \cdot p_A} \quad (2.5)$$

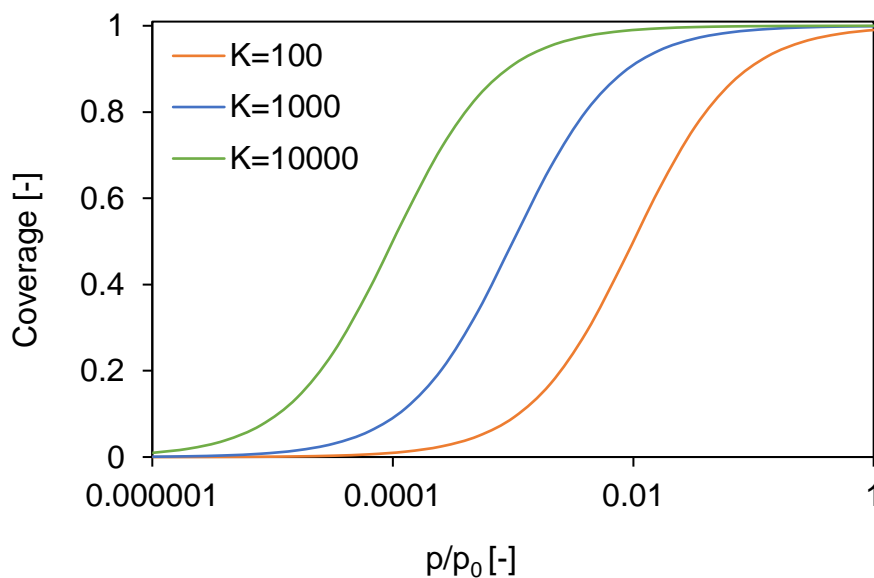


Figure 2.1: Langmuir adsorption isotherms for equilibrium constants of 100 (orange), 1000 (blue) and 10000 (green).

For low pressures,  $K \cdot p$  becomes much smaller than 1, leading to a linear relation between  $\theta$  and  $p$ , which is denoted as the Henry region.

The equilibrium constant, and therefore the coverage in equilibrium depends on the change in standard enthalpy  $\Delta H^\circ$  and entropy  $\Delta S^\circ$  between free and adsorbed state of a molecule which is defined according to van't Hoff: [32, 78]

$$K = e^{-\frac{\Delta H^\circ}{RT}} \cdot e^{\frac{\Delta S^\circ}{R}} \quad (2.6)$$

Therefore, stronger interactions between adsorbing molecules and the surface (larger  $\Delta H^\circ$ ) result in a larger equilibrium constant and a steeper isotherm at lower pressures. As the classic Langmuir equation (Equation 2.5) only considers one adsorbing species on equal sorption sites, extensions to this formalism have been proposed to describe experimentally obtained sorption data including more than one distinct sorption site or multiple adsorbing species.

If more than one sorption sites  $i$  are available for a molecule A, the coverage of A on the surface is defined by the weighted sum of the coverages on the individual sites  $i$  (Figure 2.2). [79]

$$\theta_A = \frac{\sum_i \frac{K_i \cdot p_A}{1 + K_i \cdot p_A} \cdot c_{i,sat}}{c_{sat}} \quad (2.7)$$

With  $c_{i,sat}$  being the saturation concentration (monolayer) for species A on adsorption site  $i$  and  $c_{sat}$  the overall saturation concentration  $c_{sat} = \sum_i c_{i,sat}$ .

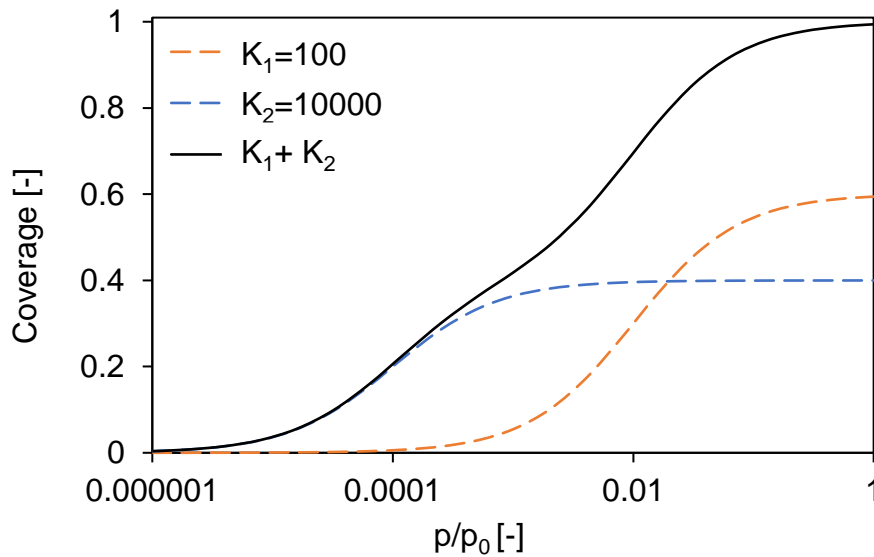


Figure 2.2: Dual site Langmuir adsorption model with sites 1 (orange) and 2 (blue). The concentration of sites is stated as  $c_1:c_2 = 3:2$ .

If two or more species are competing for one sorption site, a competitive Langmuir approach is required (Figure 2.3). Then, the coverage of species A on one specific site is determined according to Equation 2.8. [75]

$$\theta_A = \frac{K_A \cdot p_A}{1 + K_A \cdot p_A + K_B \cdot p_B + \dots + K_i \cdot p_i} \quad (2.8)$$

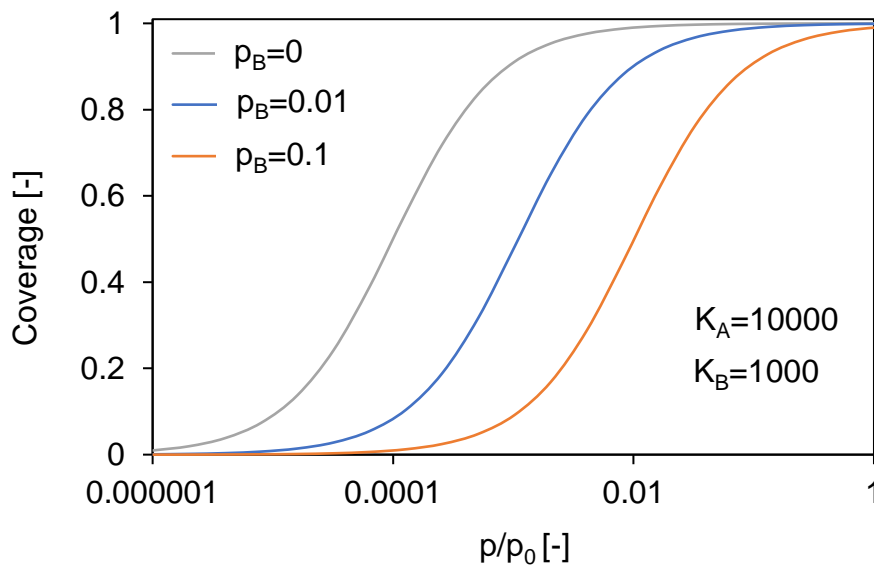


Figure 2.3: Competitive Langmuir adsorption for molecules A and B. A constant partial pressure of B with increasing partial pressure of A is applied.

Despite the common usage of the Langmuir model in the zeolite community, the assumptions made are not applicable for a broad range of materials. Except for rare cases, most solid surfaces are heterogeneous, and adsorption on these sites results in different adsorption energies. [80] As the sites interacting strongest with the adsorbate are occupied at lowest pressures, a gradual decrease in heat of adsorption is expected with increasing partial pressure. The usage of a multi-site Langmuir model can describe this behavior, but a precise knowledge of all different sorption sites is required. On high-surface materials such as silica or activated carbon, adsorption can be highly energetically heterogeneous. Especially for microporous materials, the strength of interaction with absorbing molecules can vary considerably with the location in the pore. A well-suited model for describing such behavior is the Polanyi adsorption potential theory. Developed in 1916 by Polanyi, [81] the model has been extended to a wide range of gas- and liquid-phase systems. It is based on calculating adsorption equilibria through changes in chemical potential between molecules in gas- (or liquid) phase and adsorbed on a surface. [80, 82]

One of the main assumptions of the Langmuir model is the constant heat of adsorption with increasing occupation of equal adsorption sites, which results from ideal gas theory of non-interacting molecules. While this assumption holds true for weakly interacting molecules like noble gases, molecules strongly interacting with each other or adsorption sites will change the chemical potential of the adsorbing environment for further adsorbing molecules. The Freundlich model was developed to account for the non-linearity in adsorption heat with concentration of adsorbate on an energetically heterogeneous surface. Its general form is given by:

$$Q = K_f \cdot C^n \quad (2.9)$$

where  $Q$  is the uptake per mass adsorbent,  $K_f$  the Freundlich constant, and  $C$  the concentration of adsorbate at equilibrium.  $n$  is the Freundlich exponent and is a measure for the intrinsic heat of adsorption. In contrast to the Langmuir model, Equation 2.9 does not approach linearity at low  $C$ , nor is it fixed to a limiting

adsorption capacity for a saturating  $C$ . The Freundlich model is thus more a mathematical approach for describing adsorption on energetically heterogeneous surfaces, rather than an actual physical model. [80, 83, 84]

## 2.2. Sorption kinetics – sticking coefficient

For the adsorption of a gas phase molecule A on a surface, a collision with this surface is required. Thereby, the probability for that molecule to successfully adsorb on that surface into a weakly bound physisorbed state is proportional to the number of collisions with the surface as well as the strength of interaction between molecule and surface. Therefore, the adsorption rate of the molecule A on the surface is defined as the product of a collision frequency  $r_{coll}$  and sticking coefficient  $\alpha$ , which addresses the probability of a successful collision with the surface. [75, 85]

$$r_{ads} = r_{coll} \cdot \alpha \quad (2.9)$$

For ideal gases, the collision frequency can be expressed by the partial pressure  $p_A$ , the molecule mass  $m$  and the temperature  $T$ , which according to the Boltzmann distribution define the mean gas velocity  $\langle u \rangle$  of a molecule. [78]

$$r_{coll} = \frac{\langle u \rangle}{4} \cdot n = \frac{p_A}{\sqrt{2\pi mRT}} \quad (2.10)$$

### 2.3. Multilayer adsorption

The concept of multilayer adsorption was developed by Brunauer, Emmett and Teller 1938 and is valid for molecules with weak sorbate – sorbent interactions such as nitrogen or noble gases on siliceous surfaces. This theory postulates, that one layer of molecules acts as adsorption sites for the following layer (Figure 2.4). Thereby, the number of possible adsorption layers is not limited, as each layer has the same heat of adsorption and can be treated like a monolayer for Langmuir adsorption. [86] The surface coverage is defined as:

$$\theta_{BET} = \frac{V_{ads}}{V_{mono}} = \frac{1}{1-C} \cdot \frac{C \cdot p}{1 + (C-1) \cdot p} \quad \text{with } C = e^{\left(\frac{\Delta H_{1 ads} - \Delta H_{2 ads}}{RT}\right)} \quad (2.9)$$

With  $V_{ads}$  being the adsorbed volume on the surface,  $V_{mono}$  the volume needed to form one monolayer and  $C$  expressing the change in enthalpy of adsorption between the first and second sorbate layer. Equation 2.9 can be linearized yielding the classical BET equation: [87]

$$\frac{p}{V_{ads} \cdot (1-p)} = \frac{1}{C \cdot V_{mono}} + \frac{(C-1) \cdot p}{C \cdot V_{mono}} \quad (2.10)$$

By plotting  $\frac{p}{V_{ads} \cdot (1-p)}$  against  $p$  (Equation 2.10), BET surface areas can be determined based on a known adsorbed volume and the surface area occupied by one molecule. It should be mentioned that the BET analysis is not designated for microporous materials and should be treated with great care when dealing with such.

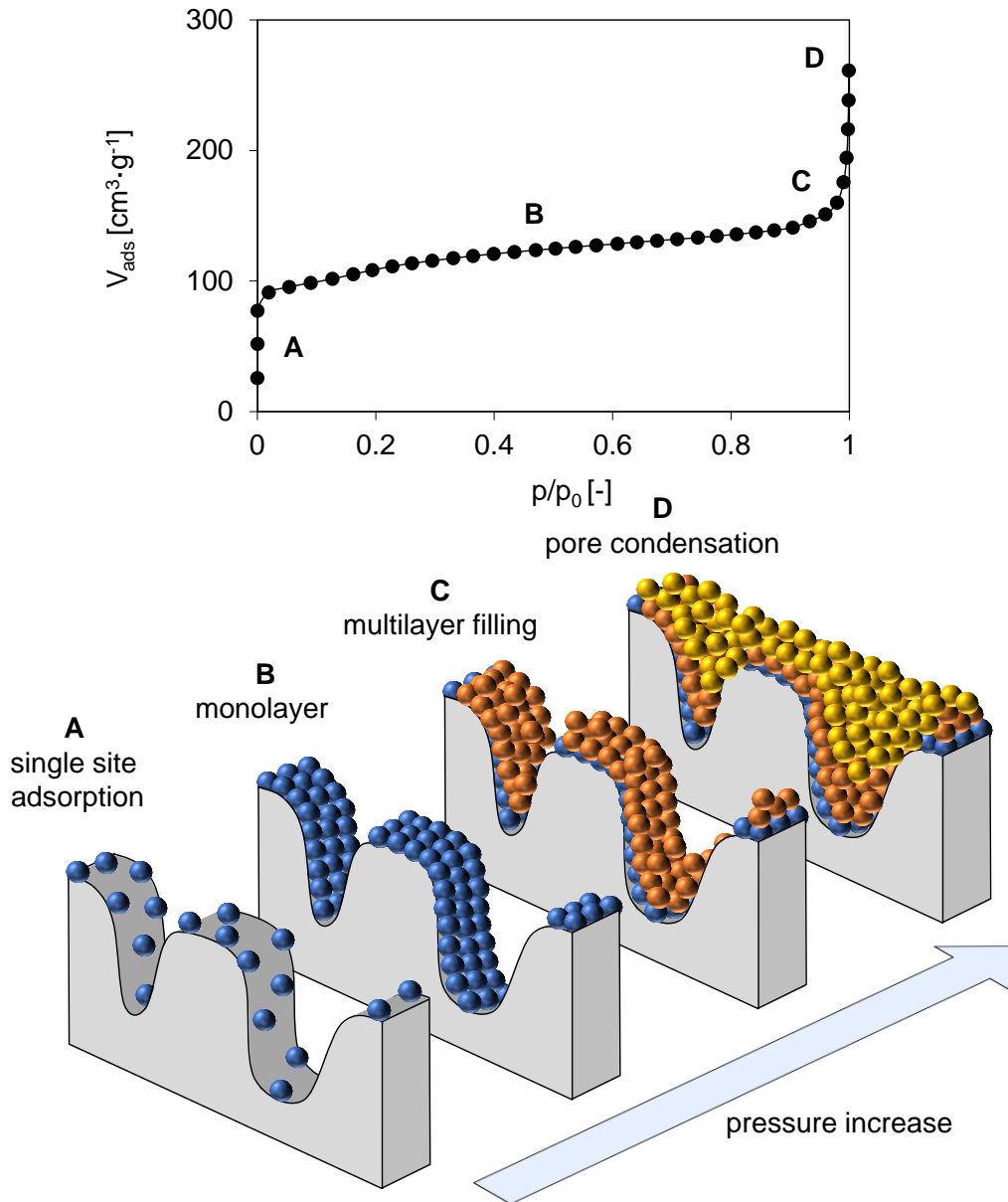


Figure 2.4: Nitrogen adsorption isotherm and illustration of surface coverage with increasing adsorbent pressure. Complete pore condensation is not reached for this example. [88]

## 2.4. Site characterization by adsorption

Adsorbing probe molecules on surfaces is a common concept for characterizing surfaces and gathering information about the concentration and properties of surface sites. In the following, especially characterization methods used for zeolite surface characterizations are discussed.

### 2.4.1. Acidic sites

Due to the importance of acid sites for various catalytic applications, determining their site concentration and location is of great importance. Acid site concentrations are typically determined by titration (as chemisorption) with basic probe molecules like ammonia or pyridine using Infrared or mass spectrometry for quantification. [89-91] As the basic probe molecules are strongly bound to the acidic surface sites, desorption only occurs at elevated temperatures in vacuum. Thereby, the desorption temperature is a measure for the acidic strength of the site and depends on the location and the chemical environment within the pores.

Besides concentration and strength of acid sites, also the location within the zeolite is of major interest. Especially for applications that rely on shape selective catalysis, externally accessible sites can significantly change the product selectivity. Externally accessible sites can be determined by using bulky probe molecules, like the sterically hindered tri-tert-butyl pyridine for small to medium sized pores (like MFI). Due to the kinetic diameter clearly exceeding the pore diameter, such molecules can only interact directly with sites accessible from the external surface. [92, 93] It should be mentioned here, that depending on the sterical constraints and the basicity of the probe molecule, different site concentrations may be obtained, due to different degrees of accessibility and interaction distances.

### **2.4.2. Interaction with substrate molecules**

Measuring adsorption isotherms of substrate and product molecules is a powerful way of gaining insight into molecule – surface interactions. Spectroscopic measurements can be used to determine the heat of adsorption and entropic changes between gas phase and adsorbed state from adsorption isotherms measured at different temperatures using van't Hoff's equation. Besides this indirect approach, also directly measuring the adsorption heat is possible using thermogravimetric methods. [94, 95] While for the direct approach only one measurement is required for determining the heat of adsorption, thermogravimetric measurements only relate the heat flux to the total mass uptake on the sample. Therefore, adsorption processes on different sites cannot be differentiated, like with spectroscopic measurements.

## 3. Transport in Porous Materials

Diffusion is among the most fundamental and important phenomena in nature and of particular interest for nanoporous materials, utilized in membranes, adsorbents and catalysts for separation and chemical conversion. Diffusion describes the random motion of particles, driven by their thermal energy. The resulting flux of the diffusing particles is defined by Fick's first law as the product of the diffusivity  $D$  and a concentration gradient  $\delta c$  along the  $x$  coordinate.

$$j = -D(c) \cdot \frac{\delta c}{\delta x} \quad (3.1)$$

It is important to note that random molecular movement can occur under both equilibrium and non-equilibrium conditions, which both can be described by Equation 3.1. While applying Fick's first law comes natural for describing non-equilibrium conditions (Figure 3.1 a), the application under equilibrium is less intuitive. [96, 97] Under equilibrium conditions, two differently labelled, but otherwise completely identical groups of molecules on opposite sides of a container can be imagined (Figure 3.1 b). The flux of both groups is then opposite to each other and of identical magnitude, so that the total concentration of particles stays constant along the  $x$  axis of the tank. The diffusion coefficient measured under such equilibrium conditions is referred to as self-diffusivity. In contrast to diffusivity along an overall concentration gradient (transport diffusivity), self-diffusivity strongly depends on the overall concentration of molecules rather than only the concentration of the labelled molecules.

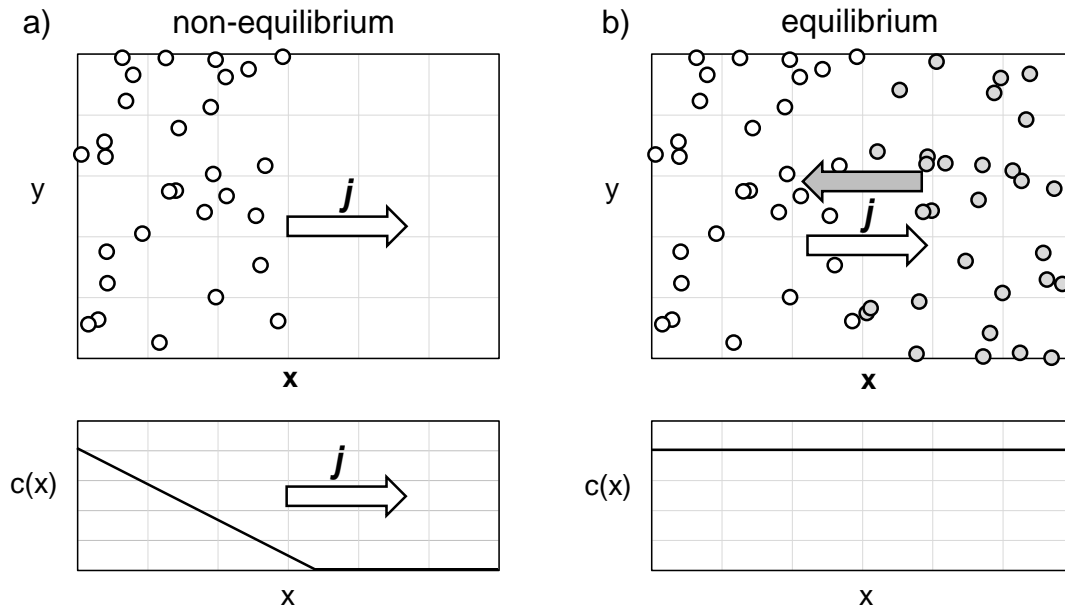


Figure 3.1: a) Concentration gradient induces flux of molecules along the x-axis (non-equilibrium situation). b) Equal distributed of identical molecules (constant concentration along x-axis) with right half molecules labeled (grey). Equal fluxes of labeled and unlabeled molecules in opposite directions canceling out.

Besides Equation 3.1, self-diffusivity can also be described by Einstein's equation (Equation 3.2), which correlates the squared displacement of a molecule from its origin ( $x_{t=0}$ ) with the diffusion time  $t$ .

$$\langle x^2(t) \rangle = 2Dt \quad (3.2)$$

It should be mentioned that transport and self-diffusion coefficients do not correlate with each other and are, except for very small concentrations, where molecule – molecule interactions can be neglected, not identical. Industrial applications for zeolites operate in general under non-equilibrium conditions, where a gradient in concentration or chemical potential is present. [96-98]

In this thesis, we will focus primarily on transport diffusion along a concentration gradient. The following section provides an overview on non-activated diffusion in relatively large macro- and mesopores as well as activated diffusion in the nanopores of zeolites.

### 3.1. Molecular diffusion

For large mesopores and macropores, the mean free pathway  $\lambda$  of a molecule is sufficiently smaller than the pore diameter  $d_p$ . Thus, the diffusion is dominated by molecule – molecule interactions and the molecule's movement can be described by a three-dimensional random walk, as expressed by Brownian molecular movement. The prevailing diffusion mechanism is referred as molecular diffusion. For zeolites, this mechanism is particularly important due to the incorporation of mesopores into the framework to increase mass transfer. Depending on the mean free path of a molecule, the diffusion coefficient can be calculated according to:

$$\lambda = \frac{1}{\sqrt{2}\pi\sigma^2} \cdot \frac{V}{N_A} \quad (3.1)$$

Here, the diffusivity  $D$  is only defined by the collision between gas molecules, and can be expressed as: [78]

$$D = \frac{\lambda \cdot \langle u \rangle}{3} = \frac{\lambda}{3} \cdot \sqrt{\frac{8RT}{\pi M}} \quad (3.2)$$

where  $\langle u \rangle$  is the mean gas velocity,  $R$  is the ideal gas constant and  $M$  the molecular weight of the diffusion molecule. [78] Considering a concentration gradient, the net flux is given by Fick's first law (Equation 3.1).

### 3.2. Knudsen diffusion

For small pores or at low pressures, the mean free pathway of a molecule is comparable to the pore diameter, and the number of collisions between molecules and pore wall exceeds the molecule – molecule collisions. In this case, energy is mainly exchanged between molecules and pore walls in consequence of a collision. Such a collision results in a diffusive reflection of the colliding molecule, whereby the velocity and direction of the leaving molecules are purely random and not related to the inciting molecules. As only molecule – wall interactions are considered, Knudsen diffusivity  $D_{Kn}$  is independent of pressure and only weakly varies with temperature and pore diameter.

$$D_{Kn} = \frac{d_p}{3} \cdot \sqrt{\frac{8RT}{\pi M}} \quad (3.3)$$

Knudsen diffusion can be expressed as Fickian flux  $j$  in a cylindrical pore, where the diffusivity only depends on the mean velocity of a molecule and the pore diameter. [99, 100]

$$j = -D_{Kn} \cdot \frac{\delta c}{\delta x} \quad (3.4)$$

### 3.3. Viscous flow

A mesopore can in first approximation be considered as a cylindrical capillary. If a pressure gradient is applied between the ends of this capillary of radius  $r$ , a laminar flow is induced, and the resulting diffusivity is given by the Fickian expression:

$$D_{vis} = \frac{p \cdot r^2}{8\eta} \quad (3.5)$$

with  $\eta$  being the viscosity of the diffusing component. [85]

In parallel to this laminar flow, a diffusive flux in the form of Knudsen diffusion can occur. As both processes occur in parallel, both contributions can, in first approximation, assumed to be additive. The total diffusivity is given by:

$$D = D_{vis} + D_{Kn} \quad (3.6)$$

In general, the viscosity can be approximated to be pressure independent over a large pressure range. Therefore, according to Equation 3.5, the diffusivity should linearly correlate with the pressure. While this approximation does hold true for a large pressure range, it is not valid for very low pressures, where the viscosity becomes pressure dependent. [85]

### 3.4. Surface and pore diffusion

For micropores with pore diameters in the range of the kinetic diameter of the diffusing molecule, the molecule never escapes the forced field of the pore wall. Here, diffusion occurs via a hopping mechanism, where molecules weakly adsorb at the pore wall and hop between the energy minima along the transport path (Figure 3.2). [85, 101] This diffusion mechanism is referred to as surface, pore, configurational or zeolitic diffusion. As molecules and pore diameter are in the same range, sterical hindrance becomes dominant and diffusivity strongly decreases with molecule diameter. Also, the geometry and arrangement of pore channels co-determines the diffusivity for surface diffusion, which makes this mechanism highly complexity and less well understood. Therefore, diffusion coefficient must be determined experimentally [102] or by molecular dynamic simulations. [103]

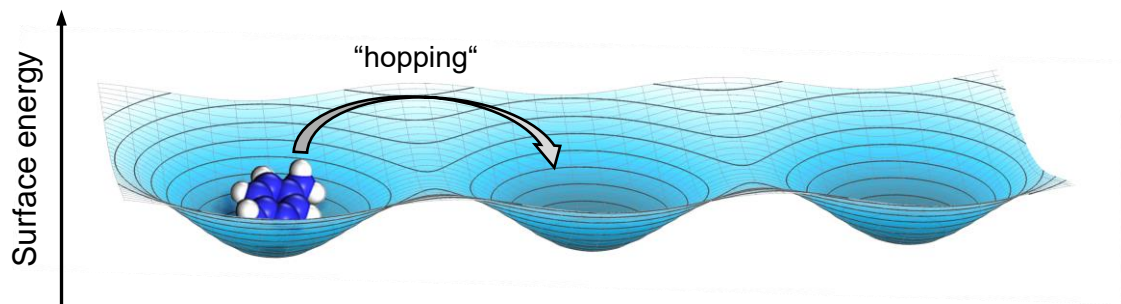


Figure 3.2: Schematic representation of *p*-xylene hopping between local energy minima on a surface.

### 3.5. Single file diffusion

For one dimensional pore system, or in unidirectional pore systems without intersection between channels, propagation of a molecule is limited to its current channel. Here, for pore diameters very similar to the kinetic diameter of the diffusing molecules, molecules are not able to pass each other and progression along the pore depends on free sorption sites in direct vicinity to the diffusing molecule. In this case, the diffusion of one molecule is co-determined by the movement of other molecules. As the movement of a molecule frees up a vacancy in backwards direction, subsequent movement is more likely to occur backwards, due to the higher probability of a free sorption site. [85, 104] As the past motion influences the next one, randomness of motion is no longer valid for single file diffusion, violating the requirement of ordinary diffusion. A mobility factor for single file diffusion can be calculated according to:

$$F_{SF} = l^2 \frac{1 - \theta}{\theta} \cdot \frac{1}{\sqrt{2\pi\tau_j}} \quad (3.8)$$

with  $l$  being the distance between two sorption sites and  $\tau_j$  the mean time between two succeeding jumps. As shown in Formula 3.8, the single file mobility strongly depends on the surface coverage  $\theta$ . [105]

For single file diffusion, transport resistances and crystalline irregularities, either on the surface or within the pores, may dramatically influence the mass transport. This mechanism is of particular interest when dealing with mixtures of molecules with very different diffusion coefficients, like mixtures of xylene molecules in MFI zeolites.

### 3.6. Surface barriers

Transport resistances may generally appear at boundaries between different phases and are denoted as surface barriers at the boundary of nanoporous particles. Such surface barriers are considered as a thin layer of significantly reduced diffusivity ( $D_{barr}$ ; Figure 3.3). Whether or not this leads on to a reduced overall transport rate depends on the ratio of surface permeation and internal diffusion. The appearance of surface barriers in zeolites has been noticed from significantly reduced uptake/release rates of diffusing molecules compared to their intracrystalline diffusion rates. The origin of these surface barriers may be explained by the preferential formation of defects on the external surface or adhesion of non-crystalline particles. [97, 106]

The magnitude of the barrier is defined by the surface permeability  $\varepsilon$  and the concentration difference between both sides of the barrier:

$$j_{surf} = \varepsilon \cdot (c_{eq} - c_{surf}) \quad (3.9)$$

As the flux is the product of diffusivity and concentration gradient (Fick's First law) along the thickness of the surface barrier  $l$ :

$$j_{surf} = D_{barr} \frac{c_{eq} - c_{surf}}{l}; \quad \varepsilon = \frac{D_{barr}}{l} \quad (3.10)$$

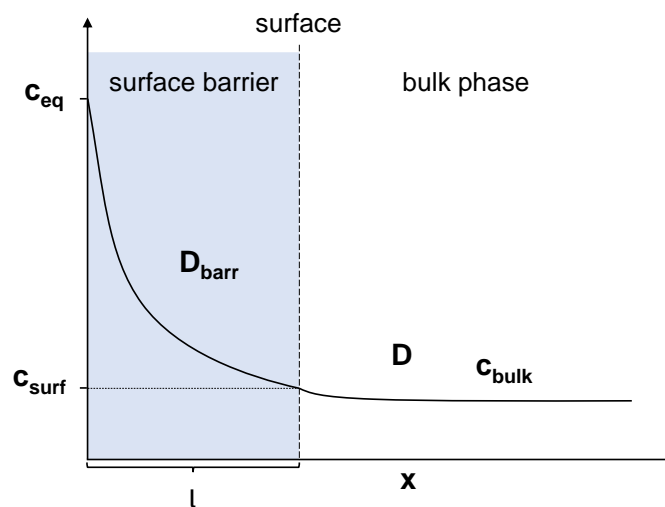


Figure 3.3: Schematic representation of a surface barrier. Note that the surface barrier thickness  $l$  is enlarged for better illustration.

An alternative model describing transport inhibition by surface barriers equally well suggests the reduction of guest solubility on the zeolite surface. In this model, surface permeation and internal diffusion are controlled by different, independent mechanisms. Crystalline materials, such as zeolites, are per definition highly ordered. Therefore, intracrystalline diffusivity does in general not depend on crystal size or crystallization procedure. The external surface of these crystals and thus their surface resistance, may however differ substantially from crystal to crystal. This can be rationalized by differences in surface defects or deposits of amorphous material on the external surface, arising from differences in their surrounding during crystallization and crystal storage. Therefore, a careful characterization of the external surface zeolites is inevitable for meaningful transport studies. [97, 106]

## **4. Applied Methods for Transport Measurements**

Several techniques were used in this work to determine transport properties on the external surface and inside the zeolite pores. In this chapter, the basic concepts and measuring principles of the most important methods used are presented.

### **4.1. Fast time-resolved infrared spectroscopy**

The rate of mass transport of hydrocarbons from the external surface of a zeolites to the catalytically active sites inside the pore network can vary greatly depending on various parameters like pore size, crystalline dimensions and the steric constrain of the diffusing molecules. Especially for small crystallites (< 100 nm), where the distance between active sites and pore openings are short, time scales of several seconds and below are common. Investigating transport at such time scales via infrared spectroscopy cannot be achieved at a satisfying signal-to-noise ratio by conventionally measuring interferograms in one single step. Fast time-resolved infrared spectroscopy can overcome this disadvantage by co-adding interferograms of different measuring cycles. More precisely, an adsorption – desorption cycle is divided in defined time slots of same length, in which, due to the shortness of the whole cycle, only few interferograms can be measured per time slot. The exact same experiment is then repeated and the new interferograms are co-added to the same defined time slots. Depending on the time scale of the cycle and the number of interferograms needed to achieve an adequate signal-to-noise ratio, the experiment is repeated several hundred times. Practically, this is done by periodically modulating the volume of a pre-equilibrated system, consisting of the gas phase of the diffusing molecule and a zeolite sample in the form of a wafer, positioned in the beamline of the spectrometer. Starting in the equilibrated state, periodically contracting, and

expanding the gas phase volume induces adsorption and desorption processes, where one cycle contains an ad- and desorption step (Figure 4.1). Therefore, this method requires perfectly reversible and reproducible measuring cycles. The induced ad- and desorption process is shown by the increase of the characteristic vibrational bands in the collected, time resolved infrared spectra.

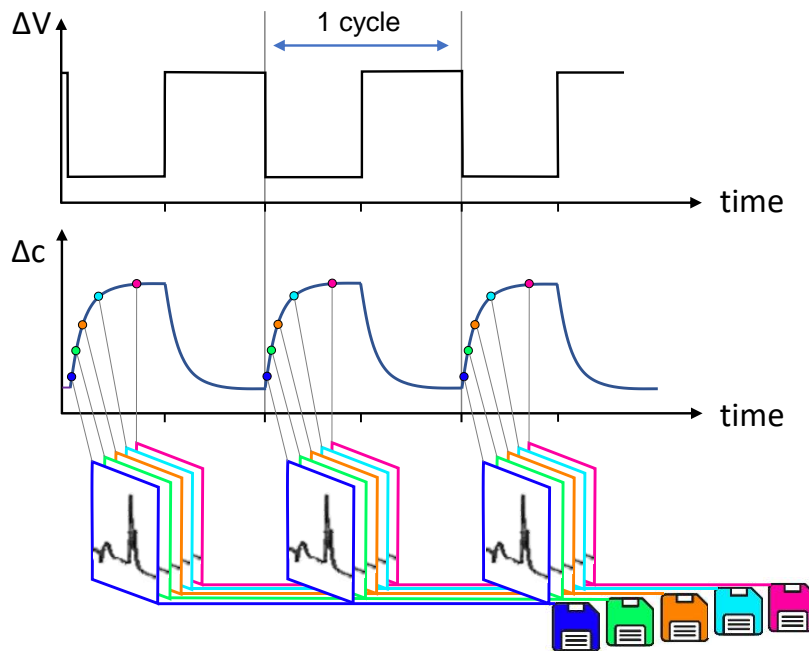


Figure 4.1: Schematic representation of the data acquisition of infrared spectra in rapid scan mode during transport measurements. [107]

To emphasize the changes in surface coverage induced by volume modulation, the last spectrum (equilibrated state) is subtracted from each spectrum of the series, resulting in a series of difference infrared spectra (Figure 4.2). The bands can then be converted in time resolved concentration profiles, using respective extinction coefficients and the time signature of the respective time slots. To extract sorption rates from concentration profiles, a first order kinetic model is applied to describe the adsorption and desorption behavior. [107-109]

Adsorption:

$$\Delta c(t) = \Delta c_{eq}(1 - e^{-t \cdot k_x}) \quad \forall \quad 0 < t \leq \frac{t_p}{2} \quad (4.1)$$

Desorption:

$$\Delta c(t) = \Delta c_{eq} \cdot e^{-\left(\frac{t-t_p}{2}\right) \cdot k_x} \quad \forall \quad \frac{t_p}{2} < t \leq t_p \quad (4.2)$$

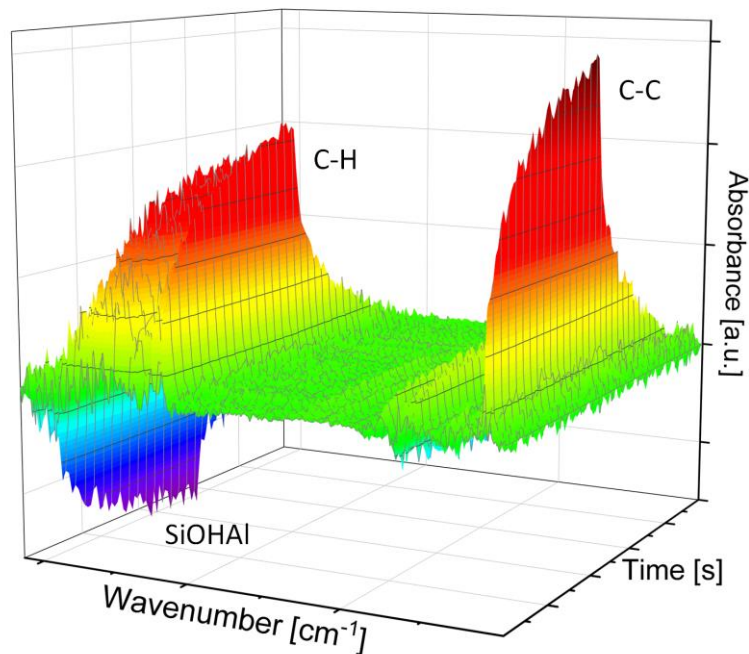


Figure 4.2: Example of time resolved infrared spectra of *p*-xylene adsorbed on HZSM-5 acquired by time resolved infrared spectroscopy described in Figure 4.1.

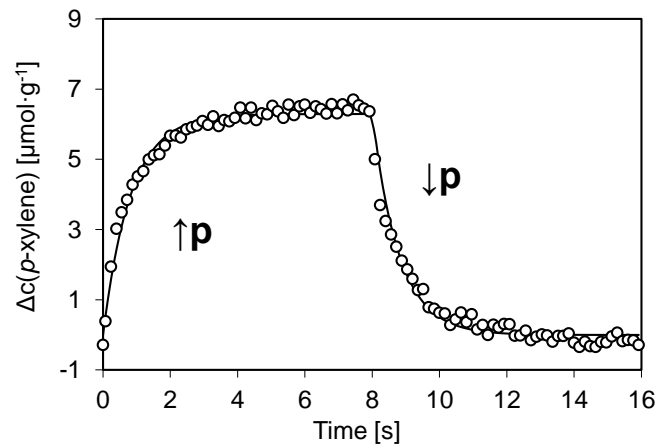


Figure 4.3: Exemplary time resolved concentration profile for *p*-xylene adsorption on HZSM-5 derived by integration of C-C stretching vibrations of time resolved infrared spectra (Figure 4.2).

Assuming an equilibrium between A (adsorbed component) and B (component in gas phase) at  $t=0$ ,

#### 4. Applied Methods for Transport Measurements

$$\frac{dc_A}{dt} = -k_{+1}c_{A(eq)} + k_{-1}c_{B(eq)} = 0 \quad (4.3)$$

with

$$k_{+1}c_{A(eq)} = k_{-1}c_{B(eq)} \quad (4.4)$$

During the volume modulation, the concentration of adsorbed species on the surface changes by  $x$ .

$$\begin{aligned} \frac{dc_A}{dt} &= -k_{+1}(c_{A(eq)} + x) + k_{-1}(c_{B(eq)} - x) \\ &= -k_{+1}c_{A(eq)} - k_{+1}x + k_{-1}c_{B(eq)} - k_{-1}x \end{aligned} \quad (4.5)$$

including Equation 4.4 results in

$$\frac{dc_A}{dt} = -(k_{+1} + k_{-1})x \quad (4.6)$$

$$k_x = k_{+1} + k_{-1} \quad (4.7)$$

As the equilibrium constant  $K$  between A and B is defined by

$$K = \frac{k_{+1}}{k_{-1}} \quad (4.8)$$

Combining 4.7 and 4.8 results in

$$k_1 = \frac{Kk_x}{1 + K} \quad (4.9)$$

For  $K \gg 1$  the fitted rate constant  $k_x$  is the rate constant for the adsorption process and, therefore the uptake profiles for ad- and desorption are equal

$$k_1 \approx k_x \quad (4.10)$$

The concentration time profiles can be described by Equations 3.9 and 3.10 and the transport rate is calculated according to Equation 4.11.

#### 4. Applied Methods for Transport Measurements

$$r_{ads} = \Delta c_{eq} k_{+1} = \Delta c_{eq} k_x \quad (4.11)$$

Due to the spectroscopic nature of this method, a differentiation between different adsorption sites and different molecules adsorbed is attainable. Therefore, this method is used in the following chapters for investigating transport processes for xylene mixtures.

## 4.2. Frequency response

The frequency response technique is a macroscopic relaxation method developed by Yasuda in the 1970s to study diffusion processes. The pressure response of an adsorption system to a periodic perturbation of varying frequency and constant amplitude is measured and the amplitude and phase lag between excitation and pressure response, different independent and thus additive transport processes can be identified (Figure 4.4). Nevertheless, only transport processes that differ in diffusivity by at least one order of magnitude can be distinctively separated. [110, 111]

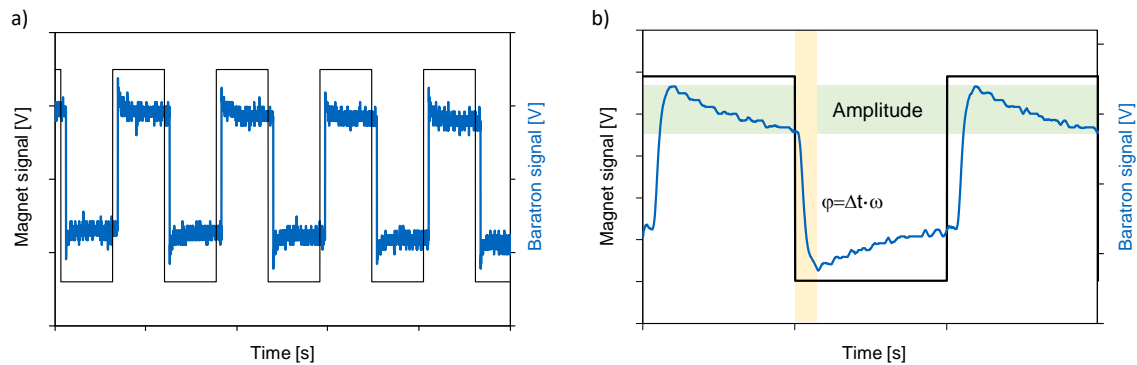


Figure 4.4: Modulation (Magnet signal) and pressure response (Baratron signal) for a frequency response experiment with *p*-xylene sorption on HZSM-5. a) Series of multiple modulations and b) magnification for closer look at the phase lag and amplitude.

Starting from an adsorption in the equilibrated state, the volume of the system is modulated periodically, either by a sinusoidal wave or as rectangular excitation (Figure 4.4). The corresponding pressure of the system  $p$  will respond with an oscillation of amplitude  $A_{FR}$ , and a phase lag to the volume modulation of  $\varphi$ , which can be directly derived (sinusoidal case), or extracted by Fourier transformation (rectangular case).

$$p = p_{eq} \cdot (1 + A_{FR} \cdot \cos(\omega t + \varphi)) \quad (4.12)$$

While the amplitude is determined by the magnitude of the volume modulation and the sorption capacity of the adsorber, the phase lag is a measure for the

sorption rate. The kinetic parameters can be derived from the solution of the mass balance of the system and are expressed as in-phase and out-phase response functions ( $\delta^{in}$  and  $\delta^{out}$ ). For a planar sheet with thickness  $2L$  these can be expressed as:

$$\frac{A_{FR,B}}{AA_{FR}} \cdot \cos(\varphi - \varphi_B) - 1 = \sum_{i=1}^n K_i \delta_i^{in} \quad (4.13)$$

$$\frac{A_{FR,B}}{A_{FR}} \cdot \sin(\varphi - \varphi_B) - 1 = \sum_{i=1}^n K_i \delta_i^{out} \quad (4.14)$$

To address the non-ideality of the system itself, blank experiments (without adsorber) under identical conditions (pressure, temperature, modulation frequency) must be included and result in a corrected phase lag  $\varphi - \varphi_B$  and an amplitude ratio between experiment with ( $A_{FR}$ ) and without ( $A_{FR,B}$ ) adsorber. The factor  $K$  account for the local slope  $\frac{dB}{dP}$  of the respective sorption isotherm and the total volume of the system  $V$ . [85, 112, 113]

$$K = \frac{RT}{V} \left( \frac{dB}{dP} \right) \quad (4.15)$$

Since simultaneously occurring, independent transport processes are additive, a simple summation of  $n$  transport processes is sufficient for Equations 4.13 and 4.14. The characteristic in-phase and out-phase functions are thereby defined by: [85, 112, 113]

$$\delta_{in} = \frac{1}{\eta_{FR}} \cdot \left( \frac{\sinh(\eta_{FR}) + \sin(\eta_{FR})}{\cosh(\eta_{FR}) + \cos(\eta_{FR})} \right) \quad (4.16)$$

$$\delta_{out} = \frac{1}{\eta_{FR}} \cdot \left( \frac{\sinh(\eta_{FR}) - \sin(\eta_{FR})}{\cosh(\eta_{FR}) + \cos(\eta_{FR})} \right) \quad (4.17)$$

with

$$\eta_{FR} = \sqrt{\frac{\omega \cdot L^2}{D}}; \omega = 2\pi f \quad (4.18)$$

The characteristic in- and out-phase functions for a single slap with thickness 250 nm are shown in Figure 4.5. Thereby, Figure 4.5 a) shows a single transport process while for b) two independent transport processes can be identified.

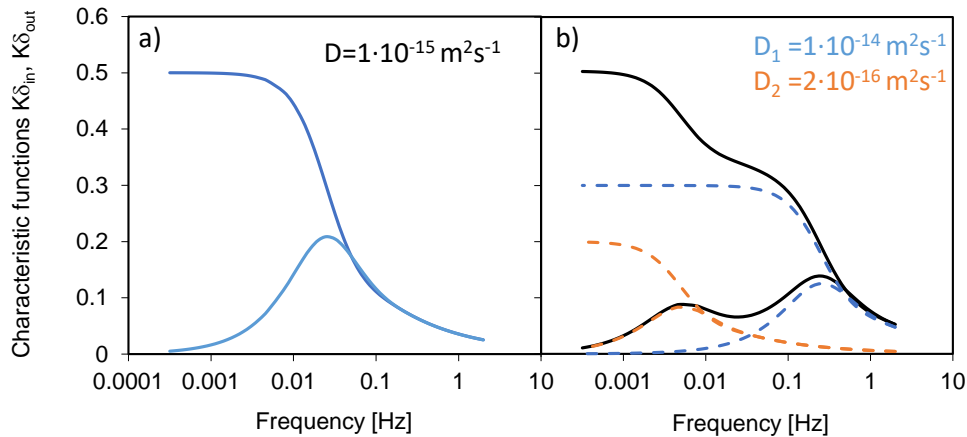


Figure 4.5: Frequency response spectra for crystallites with a half thickness of 250 nm for a) a single transport process with a diffusion coefficient of  $1 \cdot 10^{-15} \text{ m}^2\text{s}^{-1}$  and b) two independent transport processes with diffusion coefficients of  $D_1 = 1 \cdot 10^{-14} \text{ m}^2\text{s}^{-1}$  (blue) and  $D_2 = 2 \cdot 10^{-16} \text{ m}^2\text{s}^{-1}$  (orange). The spectra were calculated according to a planar sheet model.

It is worth mentioning, that different transport processes may appear at different loadings of the adsorber. A typical example is the diffusion of benzene in MFI. While for loadings below four molecules per unit cell only a single transport process appears in the frequency response spectra, for higher loadings two distinct processes are observed. Due to the two different channels of MFI, transport occurs in both – straight and sinusoidal channels – simultaneously. At low loadings, benzene can easily switch between channels, resulting in two dependent transport processes that appear as one averaged curve in the FR spectra. High loadings force the molecule to stay in its initial channel, as there is less space to reorientate in the occupied environment. This results in two independent transport processes, which show up as two distinct maxima in the frequency response spectra. [85]

### 4.3. Desorption curves

Imagining a surface with a distinct amount of sorption sites and a fraction of these sites being covered by adsorbed molecules. The coverage of this surface is then determined by the ratio of adsorption and desorption rate of the molecules at the respective pressure and temperature. Here, the mean residence time of a molecule  $\tau_{surf}$  is not affected by the partial pressure in the gas phase, nor by the coverage of the surface and solely is determined by the strength of interaction between molecule and surface adsorbed.

One way of measuring desorption kinetics is by preventing the adsorption process. This can be done by switching from the adsorbate to a pure carrier stream for flow operation (zero length column technique) or by evacuation of the adsorption cell (static approach). The desorption from the surface is followed (e.g., spectroscopically, or gravimetrically) and transferred in a concentration profile. The desorption rate constant  $k_{des}$  as well as the mean residence time on the surface are extracted from the desorption curve by fitting with a first order desorption model.

$$c(t) = c_0 \cdot \theta_{t=0} \cdot e^{-k_{des} \cdot t} \quad (4.19)$$

and

$$\tau_{surf} = \frac{1}{k_{des}} \quad (4.20)$$

For adsorption on zeolites, generally several adsorption sites with different sorption strength are available. Therefore, a differentiation between molecules desorbing from different sorption sites is required and knowledge about the coverage of these sites is essential. Due to different equilibrium constants, the specific sorption sites are occupied at different pressure regimes. For systems where the equilibrium constants for the distinct sorption sites differ by several orders of magnitude, a clear separation in the adsorption isotherm is visible (Figure 4.6 a). Here, predominantly one site is occupied in a certain pressure range and a reduction in pressure predominantly leads to a desorption from these

sites. Fitting this desorption process with equation 4.19 gives access to the desorption kinetics of the molecule on this specific site (Figure 4.6 b).

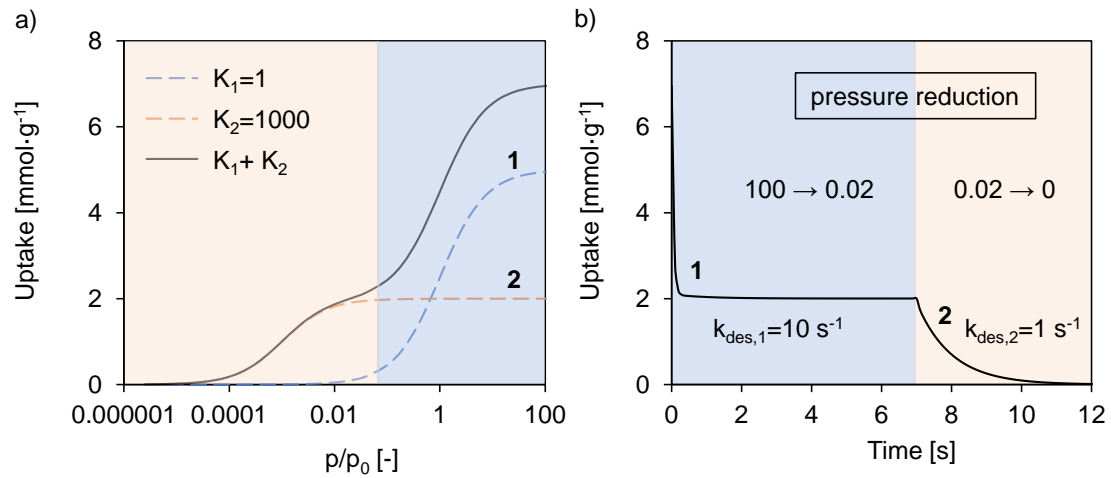
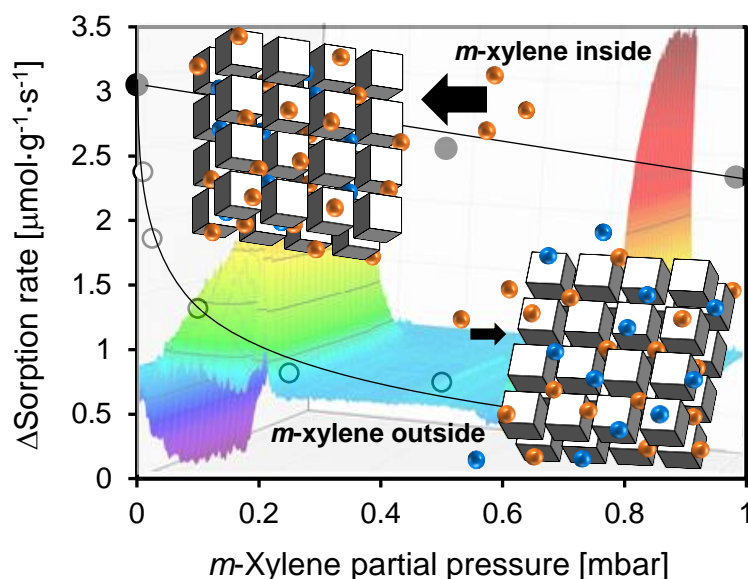


Figure 4.6: a) Langmuir adsorption isotherm on two distinct sorption sites and desorption curves for sudden pressure drops from  $p/p_0=100$  to 0.02 (desorption primarily from site 1) and from  $p/p_0=0.02$  to vacuum (desorption primarily from site 2).

## 5. Scope of the Thesis

This thesis describes the mass transport of aromatic hydrocarbons, in particular xylenes, in the microporous environment of zeolite pores. The focus is thereby set to transport in xylene mixtures and the interference of sterically hindered molecules on the transport properties of fast diffusing ones. In this context, also the role of acidic SiOHAl groups on the transport rate is to be examined. In chapter 1 – 4, general properties of zeolites, fundamental principles and characterization techniques are discussed. Chapter 6 focuses on the role of *m*-xylene during *p*-xylene transport in a purely silicious MFI zeolite and discusses the rate determining step for the *p*-xylene transport under these conditions. Chapter 7 addresses the influence of Brønsted acid sites on single *p*-xylene transport and determines energy barriers for the pore entrance with and without acid sites present. Chapter 8 combines the knowledge gained in the previous chapters and examines the transport properties of *p*-xylene in presence of *m*-xylene as well as Brønsted acid sites. To gain insight into transport under industrially relevant conditions, a *p*-xylene isomerization is followed in detail with concurrent transport measurements. The presented results contributed to a comprehensive understanding of transport in zeolites and nanoporous materials in general and will be conducive for improving industrially relevant processes like xylene isomerization and toluene methylation.

## 6. Understanding Transport Steps in Xylene Mixtures in ZSM-5 Zeolites



The transport of *p*-xylene in purely siliceous MFI was investigated in the presence of co-adsorbed *m*-xylene by combining fast time-resolved IR spectroscopy and frequency response methods. *p*-Xylene transport rates are dominated by diffusion in the straight channels of MFI, which is eight times faster than transport in the sinusoidal channels. *m*-Xylene adsorbed on the outer surface lowers the sorption rate of *p*-xylene significantly by blocking pore entrances, whereas *m*-xylene adsorbed in the MFI pores hardly influences the *p*-xylene transport rates. If the pore entrance is the rate determining step of the transport process, as for the MFI samples investigated, *m*-xylene sorption on the outer surface selectively impedes the faster transport through the straight pore openings.

## 6.1. Introduction

Medium pore size zeolites such as MFI enhance the para-selectivity in shape selective reactions of aromatic molecules including toluene alkylation and toluene disproportionation [47, 114-116] as well as xylene isomerization. [48, 117-120] In these reactions, the selective adsorption and transport of hydrocarbons in the zeolite pores is concluded to be the key factor in controlling the selectivities. [6, 85, 121-126] Three consecutive steps have been identified for the transport processes of molecules from the gas phase to the sorption/reaction sites of a zeolite inside the micropores: (i) adsorption from the gas phase on the external surface, (ii) reorientation on the surface and pore entering, and (iii) transport within the micropores to the catalytically active sites. [127] We have shown that the rate determining step for the transport of aromatic molecules on MFI zeolites depends on the crystallite size. [127] For large MFI crystallites (> 1000 nm), diffusion inside the pores determines the overall rate of the transport process, while for particles smaller than 500 nm (having significantly shorter internal diffusion paths) the pore entering step begins to dominate the overall transport kinetics.

The transport of the xylene isomers in the porous environment of MFI is crucial for the activity and selectivity in alkylation/isomerization reactions of aromatic molecules as it determines the effective residence time of the molecules in the pores and consequently the selectivity to the desired para products. [128] Diffusion coefficients for *p*-xylene in zeolites have been determined by several studies during the last decades for single component as well as in combination with other hydrocarbons. [109, 129-137] While these macroscopic processes are well-established, insight into the rate limiting steps of the transport is hardly available which is, however, required to mitigate negative effects of joint transport and to design better catalysts, e.g. for shape selective alkylation and isomerization reactions of alkyl substituted aromatic molecules. [6, 121]

In the present study, we describe and discuss the transport of *p*-xylene in a purely siliceous MFI in presence and absence of *m*-xylene. We use small MFI crystallites (with a size close to industrially used zeolites) and study the process of

## 6. Understanding Transport Steps in Xylene Mixtures in ZSM-5 Zeolites

equilibration by fast time-resolved infrared spectroscopy and the frequency response experiments. We will identify the rate determining step by investigating the influence of the location of adsorbed *m*-xylene on *p*-xylene transport, which determines the rates for the entrance of *p*-xylene into straight and sinusoidal pore openings.

## 6.2. Experimental section

### 6.2.1. Materials

Siliceous MFI was synthesized via a hydrothermal synthesis route in a stainless steel autoclave with a PTFE inlay. [138] Water, tetraethyl orthosilicate and tetra propylammonium hydroxide (40 % solution in water) were added at a (mass based) ratio of 9:5:1 and aged under stirring at room temperature overnight. Hydrothermal synthesis was carried out at 443 K for 72 h rotating the autoclaves at 30 rpm. The samples were washed with deionized water, dried and calcined under synthetic air ( $100 \text{ mL}\cdot\text{min}^{-1}$ ) at 823 K for 8 h to receive the template free siliceous MFI.

### 6.2.2. Physicochemical characterization

**Scanning electron microscopy:** Scanning electron microscopy (SEM) images were recorded on a JSM–7500 F microscope operating at 2 kV with a resolution of 1.4 nm and a nominal magnification of  $1.0 \cdot 10^5$ . For SEM, the powdered sample was suspended in isopropanol, ultra-sonicated and dropped on copper tape. The sample was probed after complete evaporation of isopropanol. Particle sizes and proportions were determined graphically via ImageJ. [139]

**N<sub>2</sub> Physisorption:** Nitrogen physisorption isotherms were measured at 77 K using a PMI automated sorptometer. The sample was activated in vacuum at 523 K for 2 h prior to the measurement and the BET surface area was calculated over a relative pressure range from 0.03 to 0.3  $p/p_0$ . The external surface areas was determined according to the benzene-filled pore method. [140] For these experiments, the sample was activated in vacuum at 523 K for 2 h and saturated with benzene at room temperature overnight. After cooling to 77 K and evacuating, N<sub>2</sub> physisorption isotherms were recorded assuming that the pores were filled with benzene and thus N<sub>2</sub> physisorption occurs only on the outer surface.

### 6.2.3. Concentration of pore openings

The concentration of pore openings on the outer surface of siliceous MFI was determined by combining electron microscopy and external surface area measurements. SEM images were used to determine the ratio between the length of the edges along the a, b and c direction of the particles (orientation defined in Figure 6.1). A 3D model of the crystallite based on the dimensions obtained by SEM and the external surface area, determined via N<sub>2</sub>-physisorption on benzene filled pores, was created. N<sub>2</sub>-physisorption isotherms measured starting from the empty and the benzene filled zeolite are shown in the supporting information (Figure S6.1).

For large MFI crystallites (in the  $\mu\text{m}$  range) it is widely accepted that they do not consist of single crystals but are rather composed of at least six pyramidal subunits. The crystal growth mechanism leads to a rotation of 90° between two (or more) of these subunits with respect to the channel orientation of the other subunits. [141-146] Depending on the number and orientation of the subunits located inside the crystal, 2-component as well as 3-component models have been proposed to describe the arrangement of subunits within one MFI crystal. [143, 147] For small MFI crystallites ( $< 1 \mu\text{m}$ ), however, like the ones investigated in this study as well as for grown MFI membranes, electron diffraction patterns indicate the presence of single crystals. [148-151]

The channel orientation of the MFI unit cell, shown in Figure 6.1, was assigned to the crystallite surface planes according to literature assuming the presence of single crystals. [147, 150] The straight channels are aligned parallel to the crystallographic b-vector, sinusoidal channels parallel to the a-vector. Sinusoidal

channel openings were also assumed to be present along the c-direction resulting from sinusoidal channel cut along the surface.

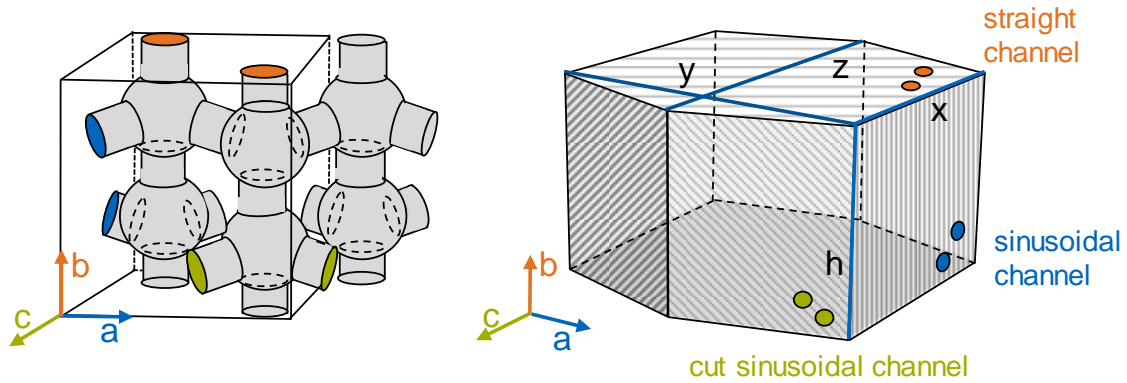


Figure 6.1: Schematic representation of the MFI unit cell (left) and the crystallite model representing the determined ratio of 1 : 1.4 : 1.5 : 1 between  $x : y : z : h$  axis and the location of straight and sinusoidal pore openings (right).

The number of pore openings for each type of channels was determined using the surface area of the unit cell site perpendicular to straight and sinusoidal channels and the corresponding area of the surface plane via:

$$c_{open.,i/g(zeolite)} = \frac{N_{open.,i/crystal}}{m_{crystal}} = \frac{2 \cdot A_{crystal,i}}{A_{unit\ cell,i}} \cdot \frac{1}{m_{crystal}} \quad (6.1)$$

with  $N_{open.,i/crystal}$  being the number of pore openings  $i$  per crystallite surface orientation,  $A_{crystal,i}$  the surface area perpendicular to channel  $i$  of the crystallite and  $A_{unit\ cell,i}$  the surface area of the unit cell site perpendicular to channel  $i$ .

#### 6.2.4. Selective deposition of *m*-xylene

The location of *m*-xylene was controlled by varying the time for equilibration and evacuation. For loading *m*-xylene into the pores, the sample was equilibrated with *m*-xylene at partial pressures between 0.010 and 0.500 mbar followed by evacuation at  $10^{-6}$  mbar for 20 minutes. For deposition of *m*-xylene on the outer surface, the sorption time was decreased to 10 minutes, which ensures that *m*-xylene does not diffuse into the pore system in significant amounts on the time

scale of the frequency response and IR experiments. After loading the samples with *m*-xylene, *p*-xylene was added and equilibrated at a partial pressure of 0.150 mbar.

### 6.2.5. Fast time-resolved IR spectroscopy

**Experimental setup and measuring principle:** The sorption kinetics of *p*-xylene in MFI zeolites was followed using fast time-resolved IR spectroscopy. A rectangular volume modulation with an amplitude of  $\pm 4\%$  and a modulation frequency of  $1/25\text{ s}^{-1}$  was applied to study the transport processes at conditions close to the equilibrium. A more detailed description of the method can be found in our previous work. [152] The concentration profiles of *p*-xylene and *m*-xylene were calculated from the intensity of the C–C stretching vibrations at  $1542\text{--}1475\text{ cm}^{-1}$  and  $1550\text{--}1422\text{ cm}^{-1}$ , respectively. Initial sorption rates were derived from the initial slopes of the concentration time profiles according to the following equations.

Adsorption:

$$\Delta c(t) = \Delta c_{eq} \left( 1 - e^{-\frac{t}{t_{ads}}} \right) \quad \forall \quad 0 < t \leq t_p/2 \quad (6.2)$$

Desorption:

$$\Delta c(t) = \Delta c_{eq} \cdot e^{-\frac{t-t_p/2}{t_{des}}} \quad \forall \quad t_p/2 < t \leq t_p \quad (6.3)$$

Herein,  $\Delta c_{eq}$  denotes the change of the sorbate concentration when reaching the equilibrium after the volume perturbation.  $t_{ads}$  and  $t_{des}$  represent the time constants of the adsorption and desorption process and  $t_p$  the time for one modulation period.

**Sample preparation and activation:** The powdered sample was carefully dispersed in isopropanol, dropped on a  $\text{CaF}_2$  infrared window and dried, which creates a thin uniform zeolite layer and insures measurements without diffusion limitations in inter-particle pores. The sample was activated at pressures below

$10^{-6}$  mbar at 673 K for 1 h prior to transport studies. All diffusion experiments were carried out at 373 K.

**Deconvolution procedure of IR spectra:** The time resolved series of infrared spectra from *p*-xylene/*m*-xylene mixtures were deconvoluted using contributions of spectra from the single substances adsorbed on the siliceous MFI sample. For deconvolution, the xylene C–C stretching vibrations located between 1550 and 1400  $\text{cm}^{-1}$  were used. Fitting was done using a least square method. For fast time-resolved IR measurements this procedure was applied for all spectra of the experiment series to obtain the individual sorption rates for *p*-xylene and *m*-xylene molecules. A graphical illustration of the deconvolution procedure can be found in the supporting information (Figure S7.2).

### 6.2.6. Frequency response measurements

**Experimental Setup:** The frequency response setup was already described in our previous work. [137] For calculating the in-phase and out-phase characteristic functions  $\delta_{in}$  and  $\delta_{out}$ , a planar sheet diffusion model with the thickness  $2L$  was applied.

$$\delta_{in} = \frac{1}{\eta_{FR}} \cdot \left( \frac{\sinh(\eta_{FR}) + \sin(\eta_{FR})}{\cosh(\eta_{FR}) + \cos(\eta_{FR})} \right) \quad (6.4)$$

$$\delta_{out} = \frac{1}{\eta_{FR}} \cdot \left( \frac{\sinh(\eta_{FR}) - \sin(\eta_{FR})}{\cosh(\eta_{FR}) + \cos(\eta_{FR})} \right) \quad (6.5)$$

with

$$\eta_{FR} = \sqrt{\frac{\omega \cdot L^2}{D}}; \quad \omega = 2\pi f \quad (6.6)$$

where  $\omega$  is the angular frequency and  $D$  the transport diffusion coefficient. For describing the pore entrance processes, a diffusion length  $L$  and diffusion coefficient  $D$  cannot be defined. Therefore,  $\frac{L^2}{D}$  is considered as the sorption time

## 6. Understanding Transport Steps in Xylene Mixtures in ZSM-5 Zeolites

constant, i.e., the time a molecule needs for the pore entering process after volume perturbation.

In the case of two independent transport processes occurring simultaneously (like for *p*-xylene in MFI), a dual planar sheet model with  $n=2$  was applied.

$$K\delta_{in} = \sum_{i=1}^n K_i\delta_{in,i} \quad (6.7)$$

$$K\delta_{out} = \sum_{i=1}^n K_i\delta_{out,i} \quad (6.8)$$

**Sample preparation and activation:** 15 mg of powdered sample was dispersed in a quartz sample holder on several layers of quartz wool to avoid bed effects. The glass-tube was connected to the vacuum setup, evacuated to  $10^{-6}$  mbar and activated at 673 K for 1 h. During the experiment, the volume of the setup was periodically modulated with a square wave volume perturbation function in a frequency range of  $10^{-4}$  Hz to 2 and an amplitude of  $\pm 4$  % of the total system volume.

**Data treatment:** The amplitude and the phase lag were obtained from a Fourier transformation of the pressure response. The parameters of the characteristic functions were obtained by least square nonlinear parameter fitting.

## 6.3. Results and discussion

### 6.3.1. Physicochemical characterization

Nitrogen physisorption led to an apparent BET surface area of  $384 \text{ m}^2\cdot\text{g}^{-1}$  and a micropore volume of  $0.17 \text{ cm}^3\cdot\text{g}^{-1}$  for the investigated siliceous MFI. The external surface area, determined via benzene pore filling method, [140] was  $39 \text{ m}^2\cdot\text{g}^{-1}$ . The average length of the crystals, determined from the analysis of the crystals by scanning electron microscopy (SEM, Figure 2), were  $120 \cdot 165 \cdot 185 \cdot 120 \text{ nm}$  (ratio  $1 : 1.4 : 1.5 : 1$ ) along the  $x \cdot y \cdot z \cdot h$  axis (as defined in Figure 7.1).

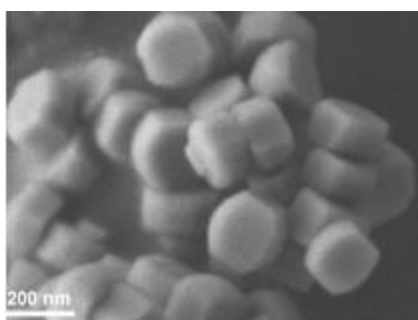


Figure 6.2: Scanning electron microscopy image of the siliceous MFI sample. The white scale bar represents 200 nm.

### 6.3.2. Concentration of pore openings

The concentration of pore openings on the outer surface was calculated combining crystal dimensions, obtained by SEM, with the external surface area, measured by  $\text{N}_2$  sorption after filling the pores with benzene. The overall concentration of pore openings was estimated to be  $45 \mu\text{mol}\cdot\text{g}^{-1}$  with  $19 \mu\text{mol}\cdot\text{g}^{-1}$  for the straight and  $26 \mu\text{mol}\cdot\text{g}^{-1}$  for the sinusoidal pore openings for siliceous MFI.

### 6.3.3. Fast time-resolved IR spectroscopy

**Single component diffusion (*p*-xylene in siliceous MFI):** A typical example of an intensity profile of the C-C stretching vibrations is presented in Figure 6.3. The functions described in Equations 2 and 3, assuming a first order sorption process, were used to fit the concentration profiles. The same rate was observed for the adsorption and desorption process, with an initial change in *p*-xylene transport rate of  $1.58 \mu\text{mol}\cdot\text{g}^{-1}$ , indicating complete reversibility of adsorption and desorption pathways. IR spectra of *p*-xylene adsorbed on siliceous MFI are shown in the supporting information (Figure S6.3).

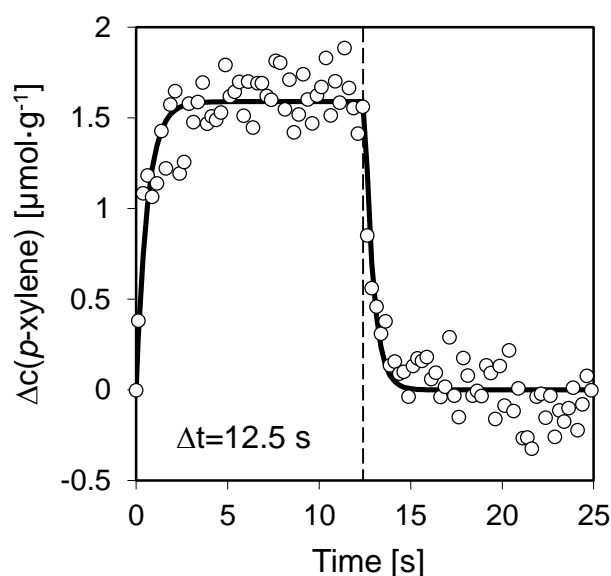


Figure 6.3: Concentration change profile for *p*-xylene (calculated from the C–C stretching vibrational bands) adsorbed on siliceous MFI induced by square wave pressure perturbations with a modulation frequency of  $1/25 \text{ s}^{-1}$ .

**Dual component mixtures: Transport of *p*-xylene in the presence of *m*-xylene:** To identify the rate determining step for the *p*-xylene transport for the investigated crystallite dimensions, slowly diffusing *m*-xylene was selectively adsorbed on the external surface or inside the micropores. As *m*-xylene diffuses about three orders of magnitude slower than *p*-xylene, [18] its presence should significantly retard the *p*-xylene transport if the transport processes compete at the surface or inside the pores in the rate determining step. The transport rates and the concentration changes of *p*-xylene in presence of *m*-xylene adsorbed on

the outer surface and inside the pores are shown in Figure 6.4. The *p*-xylene transport rates markedly decreased with increasing *m*-xylene coverage on the outer surface, while an increasing loading of *m*-xylene inside the pores showed only a minor influence on the *p*-xylene transport rates (Figure 6.4). In previous studies on the transport of single component aromatic molecules in zeolite crystals below 300 nm in diameter, we have identified the pore entrance step to be rate determining. [127] This is in perfect agreement with the present data, as *m*-xylene on the outer surface competes with *p*-xylene for the sites at the pore openings and, thus, reduces so the rate of uptake of the faster diffusing *p*-xylene molecules.

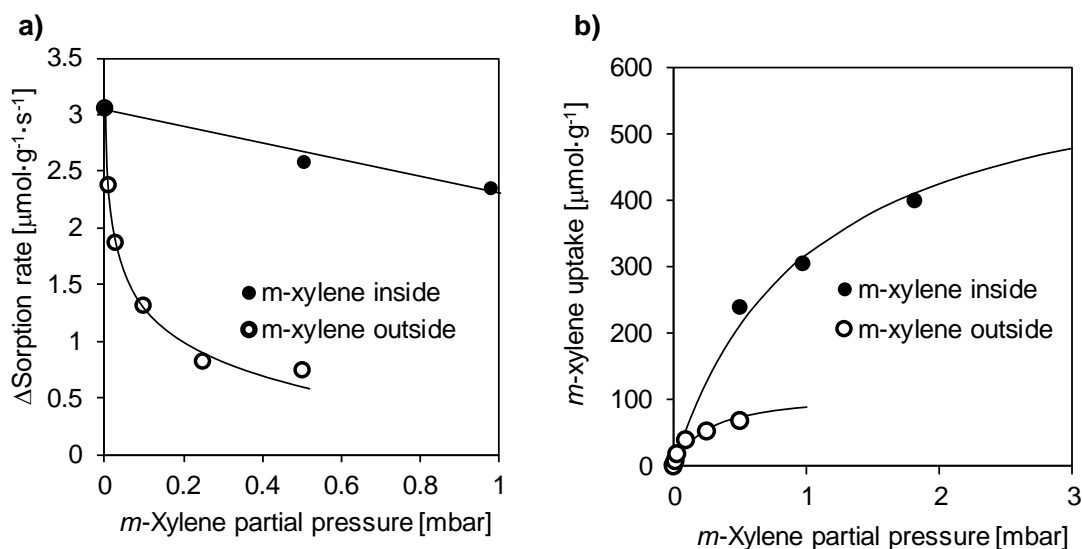


Figure 6.4: a) Change in *p*-xylene sorption rate during  $\pm 4\%$  volume modulation measured via fast time-resolved infrared spectroscopy as function of the *m*-xylene partial pressure at constant *p*-xylene partial pressure of 0.150 mbar. A sample concentration profile used for rate determination is shown in the supporting information (Figure S7.4). b) Adsorption isotherms of *m*-xylene on siliceous MFI at 373 K measured at constant *p*-xylene partial pressure of 0.150 mbar. For measuring the *m*-xylene uptake on the external surface (*m*-xylene outside) and inside the channels (*m*-xylene inside) separately, the deposition procedure described for diffusion experiments was applied.

### 6.3.4. Frequency response measurements

**Single component diffusion: *p*-Xylene transport:** The characteristic functions of the frequency response experiments for pure *p*-xylene transport with an equilibrium partial pressure of 0.150 mbar in siliceous MFI are shown in Figure 6.5.

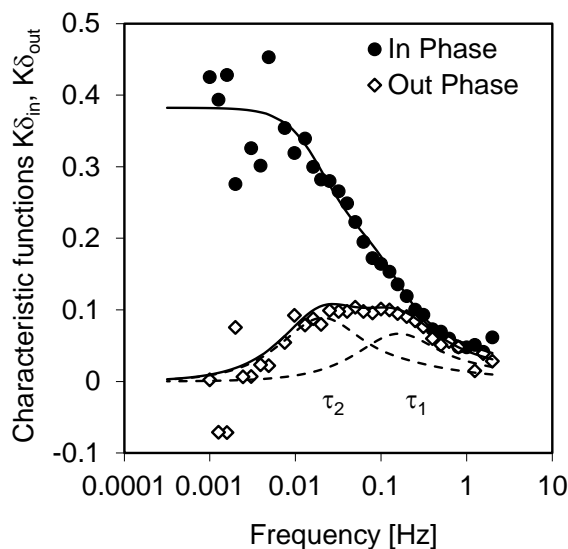


Figure 6.5: Frequency response curves for 0.150 mbar *p*-xylene adsorbed on siliceous MFI at 373 K and the fit with a dual planar sheet model including an additional surface adsorption contribution.

Two independent transport processes for *p*-xylene diffusion in siliceous MFI, characterized by two maxima in the out-of-phase characteristic function, were observed and assigned to transport processes in the straight and sinusoidal MFI channels. The slower transport process with the maximum occurring at lower frequencies ( $\tau_2$ ) is attributed to transport into the slightly smaller (0.55 · 0.51 nm) and more tortuous sinusoidal channels, while the faster transport ( $\tau_1$ ) is related to transport into the straight channels. The appearance of two independent transport processes is attributed to the inability of *p*-xylene to re-orientate at the intersections at low temperatures, which would be necessary to change between sinusoidal and straight channels. Note that for molecules like benzene, which can reorient in the intersection, only one maximum is typically observed. [85, 126]

## 6. Understanding Transport Steps in Xylene Mixtures in ZSM-5 Zeolites

Additionally, another small contribution to the overall *p*-xylene transport was observed, which is attributed to xylene adsorbing at the outer surface of the zeolite. As this process occurs much faster (at frequencies above 2 Hz) compared to the pore entrance, a distinct maximum in the out-phase function was not detected. Its existence was deduced from a slight shift in the in-phase function ( $K= 0.01$ ) to higher values throughout all frequencies measured. It must be noted that on (non-porous) silica this process was also observed (see Figure S6.6 in supplementary material).

The overall characteristic in and out phase functions (Figure 6.5) were well described by using a dual planar sheet model with an additional contribution due to surface adsorption. An additional surface resistance term was not included, as the chosen model was able to fit the characteristic functions. The sorption time constant  $\tau = \frac{L^2}{D}$ , determined from the position of the maximum in the out of phase function according to Equation 6.5, describes the time between the successful entering of two *p*-xylene molecule through the same pore opening during equilibration. For straight and sinusoidal channels, 10 and 83 s were determined as sorption time constants, which represents, in principle, the limit for the (macroscopic) transport rates in reactions and membrane permeation of *p*-xylene over MFI zeolites under the conditions (pressure, temperature) investigated. Membrane permeabilities calculated based on the assumption of a perfectly flat and oriented crystal surface using the determined sorption time constants (see Supporting Information for detailed calculation) lead to  $9.3 \cdot 10^{-8} \frac{\text{mol}}{\text{m}^2 \cdot \text{s} \cdot \text{Pa}}$  along the b-direction (straight channel pore entrance),  $1.2 \cdot 10^{-8} \frac{\text{mol}}{\text{m}^2 \cdot \text{s} \cdot \text{Pa}}$  along the a-direction (sinusoidal channel pore entrance) and  $7.6 \cdot 10^{-9} \frac{\text{mol}}{\text{m}^2 \cdot \text{s} \cdot \text{Pa}}$  along the c-direction, which is in excellent agreement to literature values reported for MFI membranes which is in the order of  $\sim 3 \cdot 10^{-8} \frac{\text{mol}}{\text{m}^2 \cdot \text{s} \cdot \text{Pa}}$ . [153-155] The number of molecules diffusing through the pores of the sample during the pressure modulation in the frequency response experiments is proportional to the uptake constant  $K$  obtained by fitting the characteristic functions. As the *p*-xylene molecules cannot change between channels and are equally distributed throughout the crystallite, the ratio between the number of accessible straight and sinusoidal channels and,

## 6. Understanding Transport Steps in Xylene Mixtures in ZSM-5 Zeolites

therefore, also of the corresponding pore openings, can be calculated from the ratio between the  $K$  values for the two transport processes. For the frequency response experiment with  $p$ -xylene only (i. e., all pores available), the ratio between the  $K$  values for straight and sinusoidal channels is in accordance to the ratio between straight and sinusoidal channels calculated from the crystallite model (Figure 6.1).

**$m$ -Xylene sorption on the outer surface:** To gain further insight into the kinetics of the  $p$ -xylene transport process, frequency response experiments were conducted with  $m$ -xylene partially blocking the pore openings (using increasing  $m$ -xylene partial pressures to change the coverage).

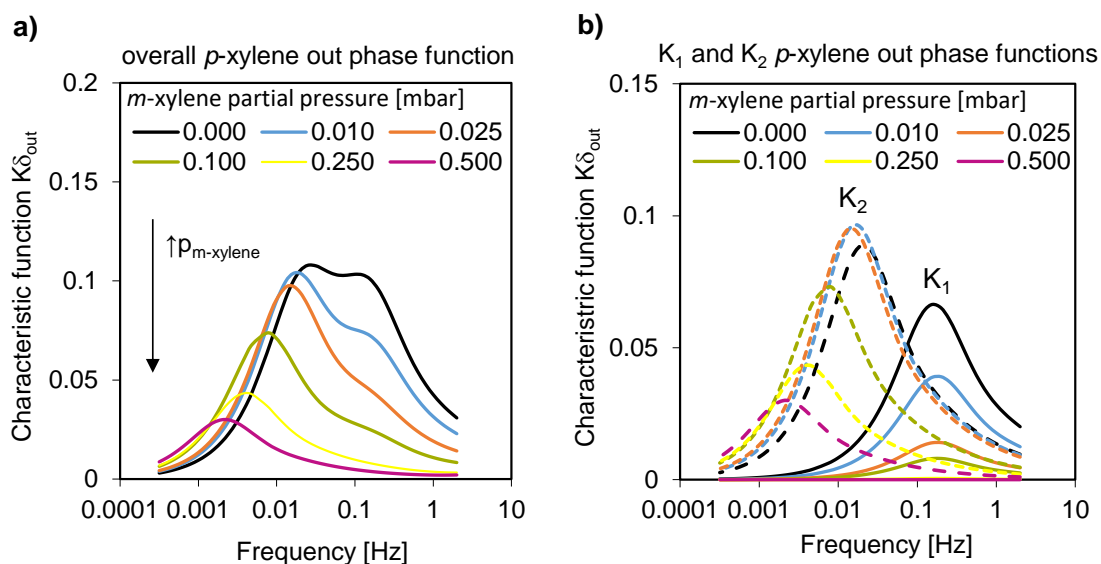


Figure 6.6: a) Out phase functions for siliceous MFI equilibrated with 0.150 mbar  $p$ -xylene at  $m$ -xylene partial pressures indicated b) Characteristic out phase functions for straight (straight line:  $K_1$ ) and sinusoidal channel (dashed line:  $K_2$ ) channel pore entrance at  $m$ -xylene partial pressures indicated using a dual planar sheet approach. The individual frequency response curves are shown in the supporting information (Figure S7.5).

With increasing  $m$ -xylene surface concentration the faster transport process through the straight channels described by  $K_1$  (0.56·0.53 nm compared to 0.55·0.51 nm for sinusoidal channel) was impeded first, whereas transport

## 6. Understanding Transport Steps in Xylene Mixtures in ZSM-5 Zeolites

through the smaller sinusoidal channels ( $K_2$ ) remained unaffected (Figure 6.6). The selectively reduced uptake through the straight channels with increasing surface coverage of *m*-xylene indicates that *m*-xylene adsorbed on the outer surface of the zeolite preferably blocks the pore openings to the straight channels. The sorption time constant  $\tau_1$  for the straight channels, however, is not affected by the presence of *m*-xylene. The slower transport process in the sinusoidal channels (represented by  $K_2$ ) is suppressed only after the diffusion through the straight channels is almost completely hindered. This decrease in  $K_2$  after most of the straight channels were blocked by *m*-xylene is manifested by an increasing time constant  $\tau_2$  for the pore entrance of *p*-xylene into the sinusoidal pore openings (Table 6.1).

With increasing coverage of *m*-xylene on the external surface, the mobility of *p*-xylene weakly bound to the surface decreases thus lowering the probability for *p*-xylene to achieve the appropriate orientation to enter the pores, thus increasing the time constant  $\tau_2$  for the pore entrance.

Having determined the total pore concentration, the ratio between  $K_1$  and  $K_2$  can be used to estimate the fraction of straight and sinusoidal channels available for *p*-xylene for each measured *m*-xylene surface coverage according to Equation 6.9.

$$c(\text{free pore openings})_i = \frac{K_i}{K_{0, \text{overall}}} \cdot c_o = \frac{K_i}{K_{0, \text{str.}} + K_{0, \text{sinus.}}} \cdot c_o \quad (6.9)$$

With  $K_i$  denoting the uptake constant for the straight and sinusoidal channel,  $K_{0, \text{str.}}$  and  $K_{0, \text{sinus.}}$  the contributions of straight and sinusoidal channel for pure *p*-xylene (all channels available) and  $c_o$  the pore opening concentration without pore blocking. The pore concentrations as well as the sorption time constants at varying *m*-xylene partial pressure are presented in Table 6.1.

## 6. Understanding Transport Steps in Xylene Mixtures in ZSM-5 Zeolites

Table 6.1: Sorption time constants and available pore openings for *p*-xylene transport into straight and sinusoidal pore openings at varying *m*-xylene and constant *p*-xylene (0.150 mbar) partial pressure.

<i>m</i> -Xylene pressure [mbar]	Straight pore openings		Sinusoidal pore openings	
	Available pore openings [ $\mu\text{mol}\cdot\text{g}^{-1}$ ]	Sorption time constant $\tau_1$ [s]	Available pore openings [ $\mu\text{mol}\cdot\text{g}^{-1}$ ]	Sorption time constant $\tau_2$ [s]
0.000	19	10	26	82
0.010	11	9	26	101
0.025	4.1	9	26	107
0.100	2.3	9	21	220
0.250	0.1	9	13	374
0.500	0.0	-	9	741

Having derived the concentration of available pore openings for the straight and sinusoidal channels as well as the specific sorption time constants, the transport rates of *p*-xylene can be calculated according to Equation 6.10, which is based on the assumption that only one *p*-xylene molecule can enter one pore opening at the same time. As *p*-xylene and the channels of MFI have similar kinetic diameter (0.59 and 0.56 · 0.53 nm, respectively), [7, 156] it seems rather unlikely that two *p*-xylene molecules could fit through one pore at the same time.

$$\Delta r_i = \frac{c(\text{pore openings})_i}{\tau_i} \quad (6.10)$$

The indices *i* denotes the channel type (straight or sinusoidal) utilized by *p*-xylene for pore entering. The calculated and measured sorption rates are presented in Table 6.2 as well as in Figure 6.7.

## 6. Understanding Transport Steps in Xylene Mixtures in ZSM-5 Zeolites

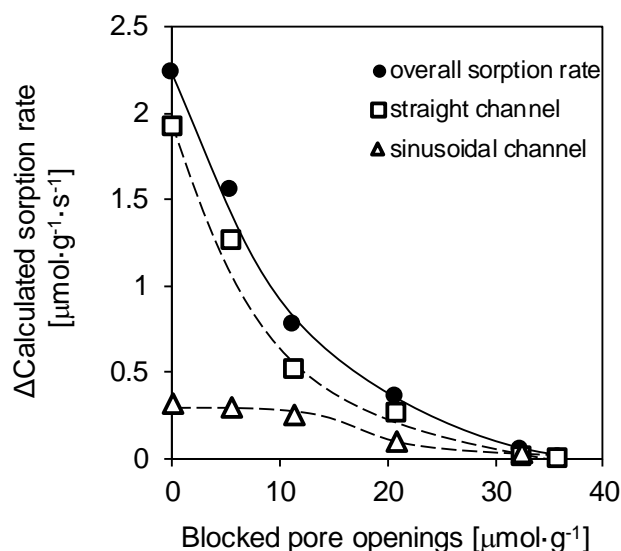


Figure 6.7: Overall (filled symbol) as well as channel specific (open symbols) *p*-xylene sorption rates on Siliceous MFI as function of the number of available pore openings.

Table 6.2: Calculated (frequency response) and measured (fast time-resolved IR) *p*-xylene sorption rates at varying *m*-xylene and constant *p*-xylene (0.150 mbar) partial pressure.

<i>p</i> ( <i>m</i> -Xylene) [mbar]	r(straight) [ $\mu\text{mol}\cdot\text{g}^{-1}\cdot\text{s}^{-1}$ ]	r(sinusoidal) [ $\mu\text{mol}\cdot\text{g}^{-1}\cdot\text{s}^{-1}$ ]	r(overall) [ $\mu\text{mol}\cdot\text{g}^{-1}\cdot\text{s}^{-1}$ ]	r(IR) [ $\mu\text{mol}\cdot\text{g}^{-1}\cdot\text{s}^{-1}$ ]
0.000	1.9	0.32	2.2	3.1
0.010	1.3	0.29	1.6	2.5
0.025	0.5	0.26	0.8	1.9
0.100	0.3	0.10	0.4	1.3
0.250	0.02	0.03	0.05	0.82
0.500	0.00	0.01	0.01	0.69

Note that the rates derived from the frequency response experiments are lower compared to the rates obtained via fast time-resolved infrared measurements. To understand this difference, we must identify which transport processes are included in the rates determined. For the rates obtained via the frequency response method it can be seen from the two out phase maxima as well as the rate calculations (Equation 6.10), that the rate describes the pore entering

## 6. Understanding Transport Steps in Xylene Mixtures in ZSM-5 Zeolites

kinetics into straight and sinusoidal pore openings. On the other hand, IR spectroscopy measures adsorption-desorption processes in a time interval of 12.5 seconds, which is too short to observe the eight times slower pore entering process of *p*-xylene through the sinusoidal pore openings. Therefore, primarily the fast transport process of *p*-xylene through the straight pore openings can be observed on the time scale of the fast time resolved infrared experiment (which contributes 86 % to the overall pore entering rate).

Thus, in the rapid scan experiments only half the *p*-xylene uptake, expected from the (equilibrium) sorption isotherm, i.e.,  $1.6 \mu\text{mol}\cdot\text{g}^{-1}$  with the respect to the uptake from the *p*-xylene adsorption isotherm of  $3.1 \mu\text{mol}\cdot\text{g}^{-1}$ , was observed (Figure 6.8). This confirms that primarily the faster *p*-xylene transport through the straight pore openings occurs on the time scale of the fast time-resolved IR.

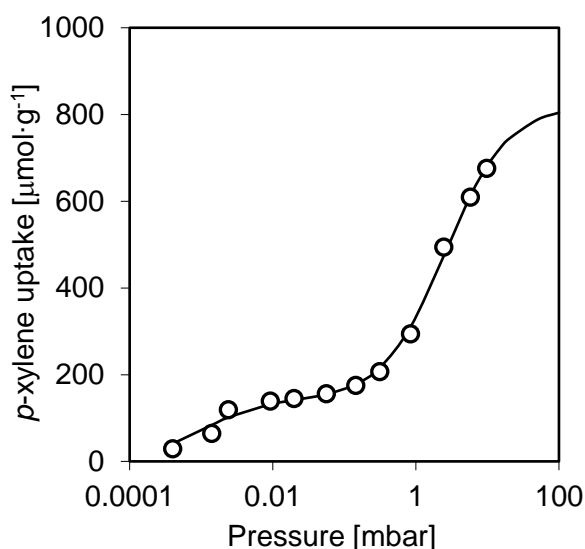


Figure 6.8: *p*-Xylene isotherm on siliceous MFI measured (open symbols) at 373 K and fit using a Langmuir type isotherm (full line). A pressure change from 0.144 to 0.156 mbar resulted in concentration change of adsorbed *p*-xylene on siliceous MFI of  $3.1 \mu\text{mol}\cdot\text{g}^{-1}$ .

The fast contribution of the *p*-xylene sorption on the external surface is included in the transport rate measured via fast time-resolved IR. As already described, this process contributes with a shoulder at high frequencies in the frequency response experiments (see Figure 6.5) but is not included into the rate calculation

## 6. Understanding Transport Steps in Xylene Mixtures in ZSM-5 Zeolites

based on frequency response. As the coverage with *p*-xylene was quantified by integration of the C–C stretching vibrations (1542 to 1475 cm<sup>-1</sup>) *p*-xylene molecules inside the micropores and molecules physisorbed on the outer surface were included into the sorption rates determined via IR. Therefore, the measured initial *p*-xylene adsorption rate is a combination of the adsorption rates from the gas phase to the external surface and the straight channel pore entrance.

The adsorption rate on the external surface due to volume modulation can be estimated using the *p*-xylene collision frequency and sticking probability based on the Hertz-Knudsen equation.

$$\Delta r_{ads,surf.} = \alpha \cdot \left( \frac{p_2(1 - \theta_2) - p_1(1 - \theta_1)}{\sqrt{2\pi \cdot m \cdot k_B \cdot T}} \right) \quad (6.11)$$

where  $\alpha$  denotes the sticking coefficient for *p*-xylene on ZSM-5,  $p$  the *p*-xylene partial pressure [Pa],  $\theta$  the overall surface coverage,  $m$  the mass of one molecule [kg],  $k_B$  the Boltzmann constant [J/K] and  $T$  the temperature [K]. The sticking probability was derived applying statistical thermodynamics, describing the loss of molecular degrees of freedom according to Equation 6.12. A detailed explanation on the sticking probability calculation can be found in our previous work. [152]

$$\alpha = \frac{q_{rot} \cdot q_{vib}}{q_{rot}^{gas} \cdot q_{vib}^{gas}} \quad (6.12)$$

With  $q_{rot}^{gas}$ ,  $q_{vib}^{gas}$ ,  $q_{rot}$  and  $q_{vib}$  describing the rotational and vibrational partition functions of the sorbate molecule in the gas phase and in the physisorbed state, respectively. According to this equation, the sticking coefficient for *p*-xylene adsorbing on the external surface of siliceous MFI was determined to be  $1 \cdot 10^{-5}$ .

The overall surface coverage was derived using an *m*-xylene adsorption isotherm, where *m*-xylene, due to short equilibration times, was only located at the outer surface (Figure 6.4b). Note that the same equilibrium constant for meta- and para-xylene was assumed based on the identical heats of adsorption for both molecules. [157] The derived surface coverages as well as the calculated adsorption rates on the surface are presented in Table 6.3.

## 6. Understanding Transport Steps in Xylene Mixtures in ZSM-5 Zeolites

Table 6.3: Changes in the surface adsorption rate derived via statistical thermodynamics, as well as total surface coverages  $\theta$  for low (1) and high (2) pressure state during volume modulation.

$p(m\text{-xylene})$ [mbar]	$p(\text{total})$ [mbar]	$\theta_1(\text{total})$ [%]	$\theta_2(\text{total})$ [%]	$\Delta r_{ads,surf.}$ [ $\mu\text{mol}\cdot\text{g}^{-1}\cdot\text{s}^{-1}$ ]
0.000	0.150	60.0	61.4	1.34
0.010	0.160	61.6	62.8	1.25
0.025	0.175	63.8	65.0	1.17
0.100	0.250	71.6	72.4	1.08
0.250	0.400	80.1	80.7	0.77
0.500	0.650	86.8	87.0	0.70

After subtracting the surface adsorption rates from the rates measured via fast time-resolved infrared spectroscopy, the rates are almost identical to the *p*-xylene pore entrance rates determined via frequency response (Figure 6.9).

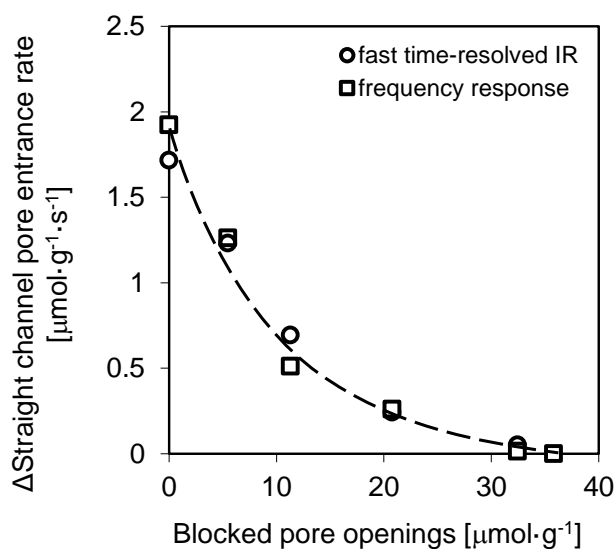


Figure 6.9: Comparison of straight channel pore entrance rates derived via fast time resolved IR and frequency response method.

## 6. Understanding Transport Steps in Xylene Mixtures in ZSM-5 Zeolites

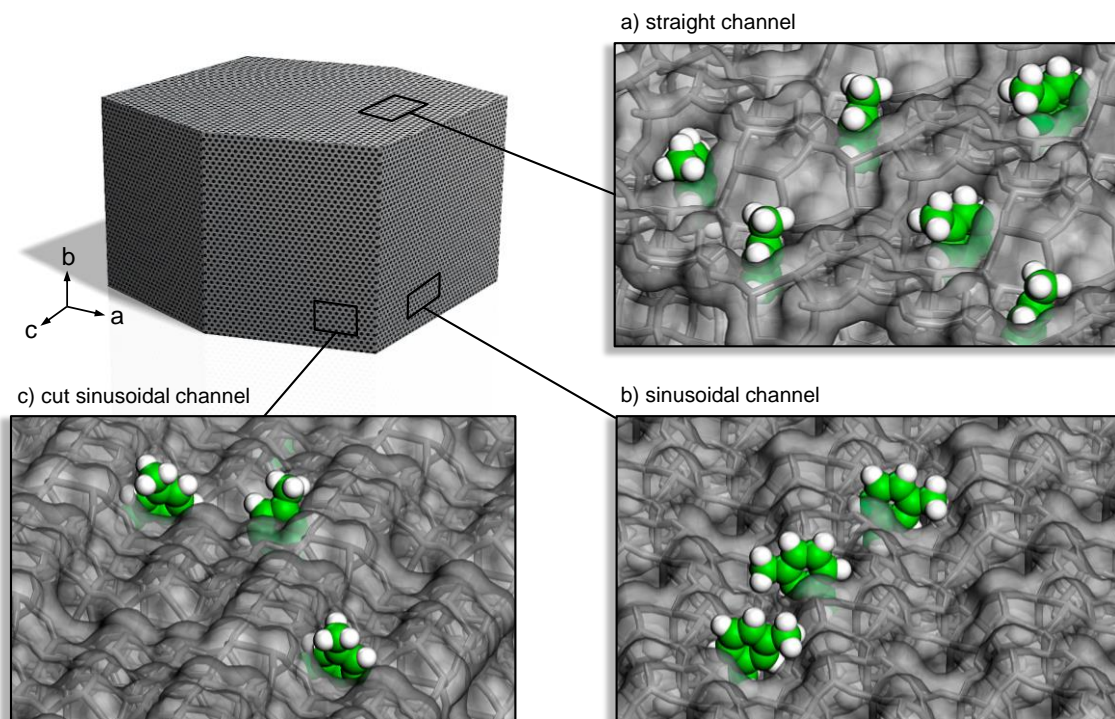


Figure 6.10: Siliceous MFI zeolite model with surface adsorbed *m*-xylene; a) adsorption in straight pore openings, b) sinusoidal pore openings, c) cut sinusoidal pore openings.

For better understanding of the preferential sorption of *m*-xylene at the pore openings of the straight channels, a closer look at the zeolite surface is required. The location of *m*-xylene at the pore openings of the straight and sinusoidal channels, based on the crystal geometry of the MFI structure, is depicted in Figure 6.10. Using the size of the (unrelaxed) xylene molecules and the pores, a much tighter fit for *m*-xylene in the openings to the straight channels compared to sinusoidal and cut sinusoidal pore openings was observed. Thus, a higher heat of adsorption is expected, which can explain the preferential sorption of *m*-xylene into the straight pore openings. Note that we have observed that for the adsorption benzene in MFI zeolites the difference in the heat of adsorption of 3 - 4  $\text{kJ}\cdot\text{mol}^{-1}$  leads to a preferential adsorption of the molecules at intersection containing Brønsted acid sites. [158, 159]

## 6.4. Conclusion

The macroscopic transport rates of binary mixtures of xylenes strongly depend on the presence of slow diffusing molecules. We have shown that the overall *p*-xylene transport rate is directly proportional to the available fraction of straight channel pore openings. *p*-Xylene is transported through the straight channel pore openings about eight times faster than through sinusoidal channel openings. Due to preferentially impeding the *p*-xylene transport through the straight channel openings, even small surface concentrations of *m*-xylene have a significant impact on *p*-xylene transport rates for small zeolite crystals. As the pore entrance step is rate limiting for aromatic molecules with small crystallite medium pore zeolites, sorption of *m*-xylene inside the pores (up to 2.2 molecules *m*-xylene per unit cell) has only a minor effect on the (macroscopic) overall *p*-xylene transport rate. Therefore, the entrance rate into the pores defines the maximum rates for reactions and permeation of *p*-xylene. The sorption of molecules with slow diffusivity will decrease the number of available sites and thus presents an additional contribution decreasing the reaction rate. As, for *p*-xylene, the pore entrance into the straight channels is about one order of magnitude faster than into the sinusoidal channels, this further indicates that transport of substrate and products will predominantly occur through the straight channels and that blocking the openings of these channels e.g. by re-adsorption of bulky products on the external surface of the zeolite – even in small quantities – can lead to severe transport limitations for molecules unable to re-orientate between channels.

## 6.5. Supporting information

### Determination of surface area

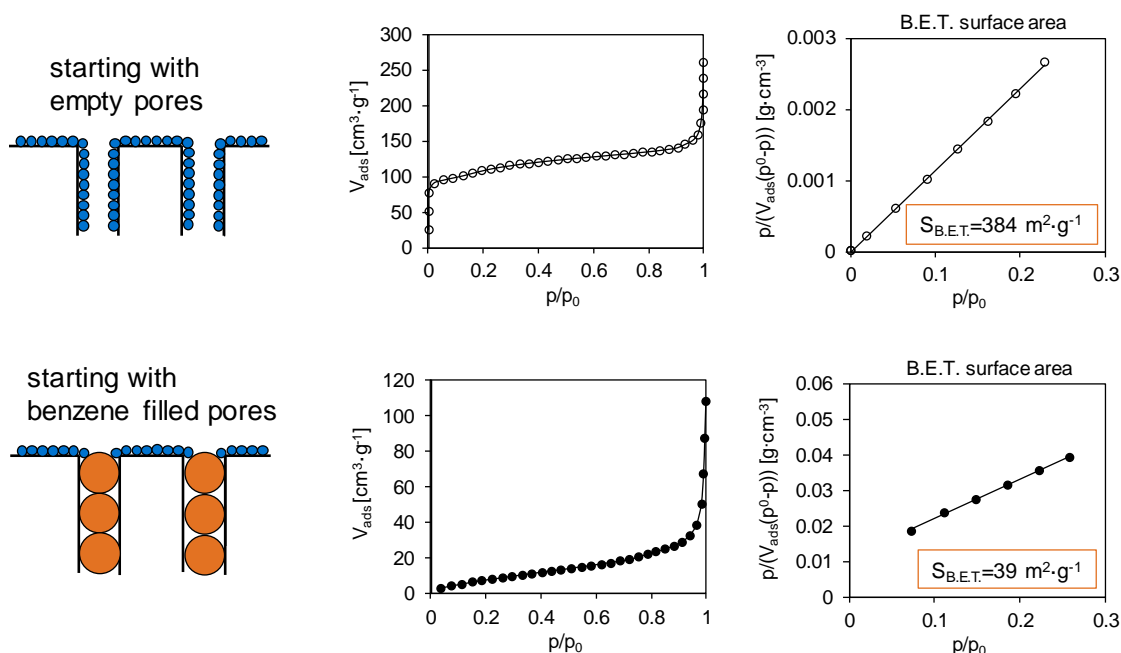


Figure S6.1: Determination of overall and external surface area from  $N_2$  Physisorption measurements starting from empty and benzene-filled zeolite.

### IR spectra

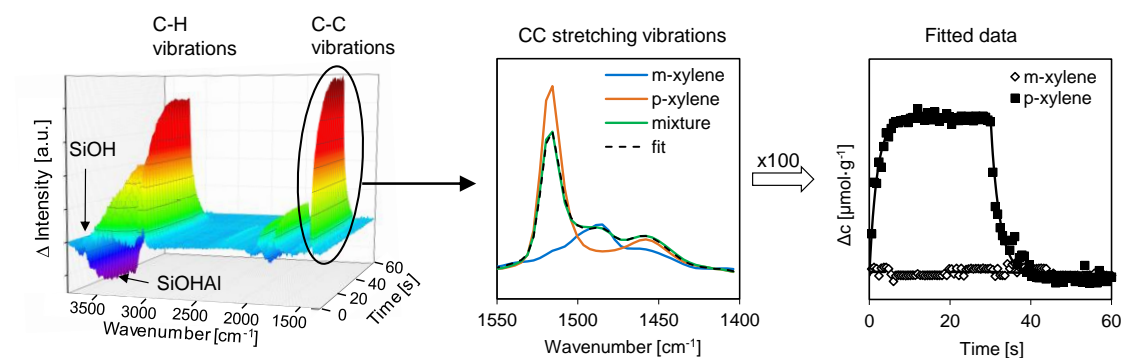


Figure S6.2: Deconvolution procedure used for separating *m*-xylene/*p*-xylene mixtures measured via fast time-resolved IR spectroscopy.

## 6. Understanding Transport Steps in Xylene Mixtures in ZSM-5 Zeolites

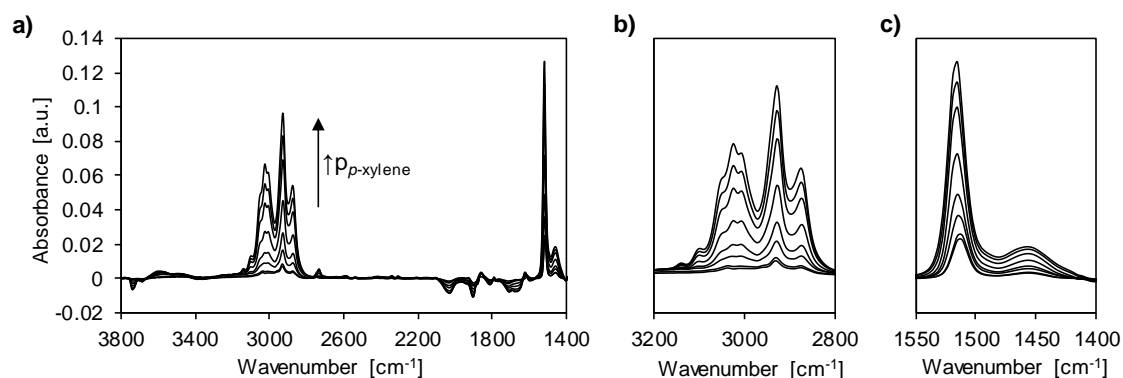


Figure S6.3: IR spectra for *p*-xylene adsorption on Siliceous MFI at 373 K. a) Difference IR spectra for *p*-xylene adsorption on Siliceous MFI b) Magnified section showing *p*-xylene C–H stretching vibrations c) Magnified section showing *p*-xylene C–C stretching vibrations.

### Fast time-resolved IR measurements

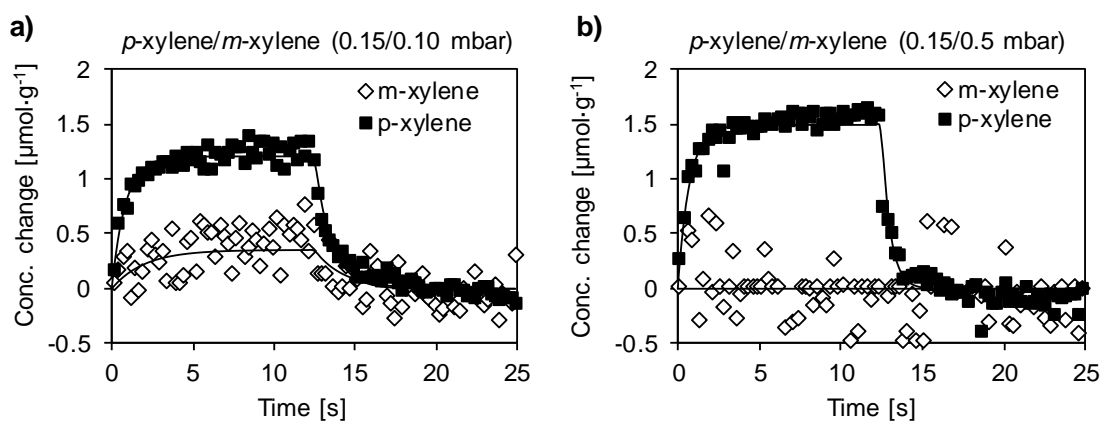


Figure S6.4: Concentration profiles measured via fast time resolved IR for *m*-xylene/*p*-xylene mixtures on Siliceous MFI at 373 K. a) 0.100 mbar *m*-xylene followed by 0.150 mbar *p*-xylene (*m*-xylene adsorbed on the outer surface) and b) 0.500 mbar *m*-xylene followed by evacuation and equilibrated with 0.150 mbar *p*-xylene (*m*-xylene located inside the pores).

## Frequency response measurements

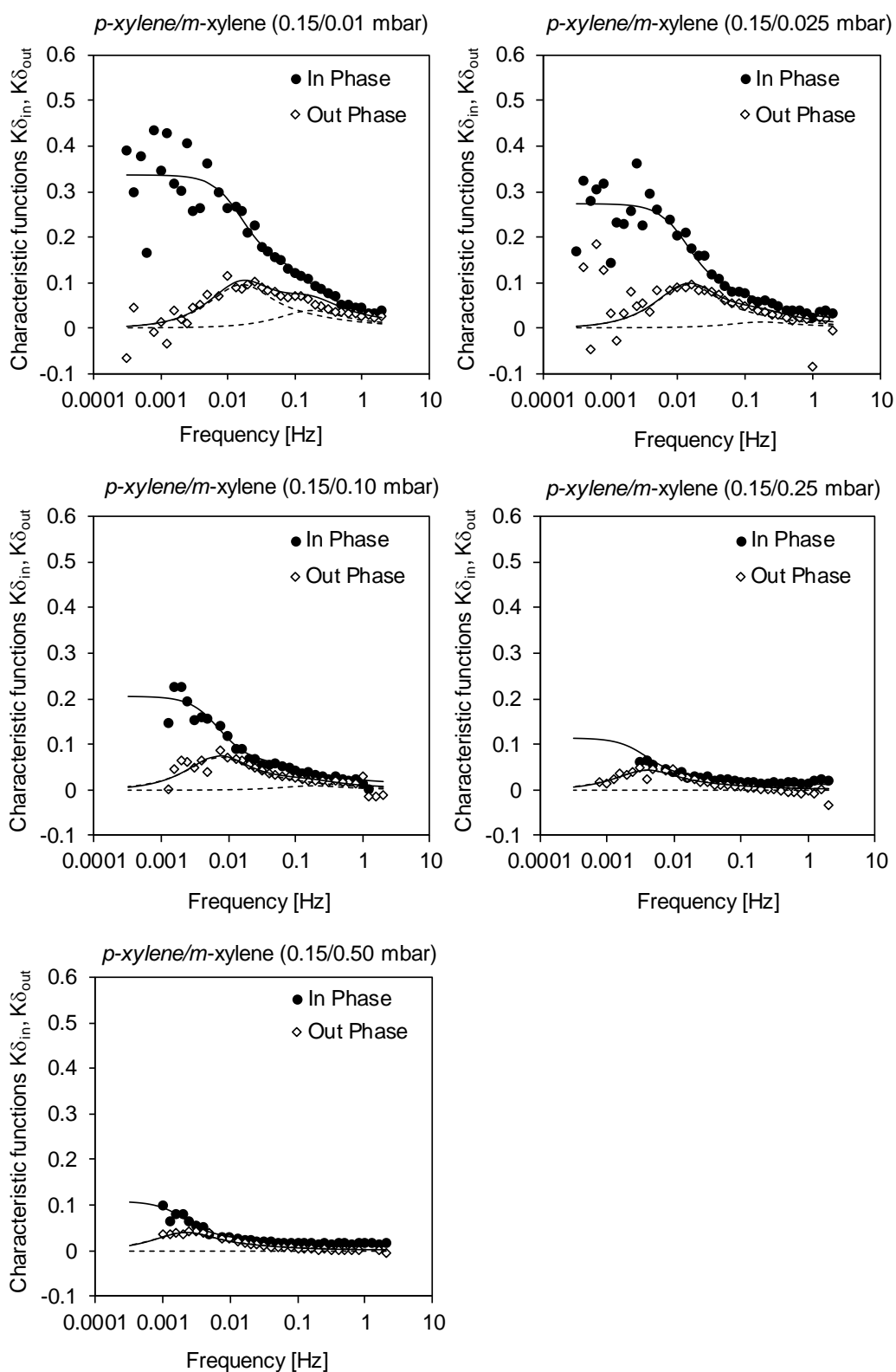


Figure S6.5: Frequency response curves measured for  $m$ -xylene/ $p$ -xylene mixtures at different  $m$ -xylene partial pressures on Siliceous MFI at 373 K. The

## 6. Understanding Transport Steps in Xylene Mixtures in ZSM-5 Zeolites

curves show the situation for *m*-xylene adsorbed primarily on the outer surface of the zeolite.

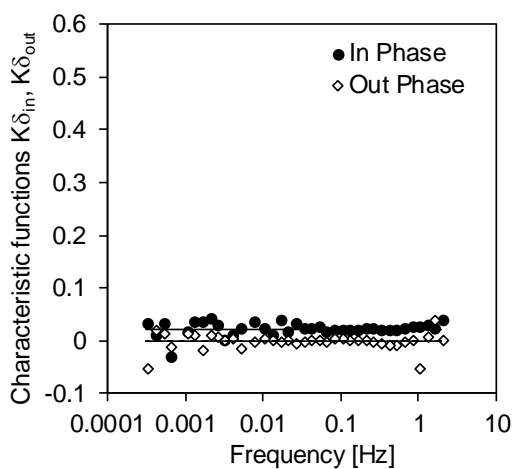


Figure S6.6: Frequency response curve measured for 0.150 mbar *p*-xylene adsorbed on nonporous Silica at 373 K.

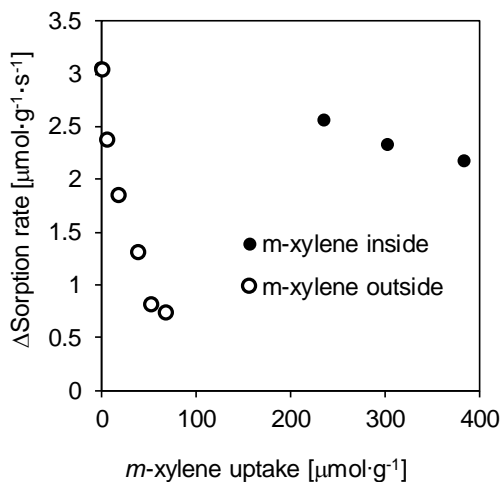


Figure S6.7: Change in *p*-xylene sorption rate during  $\pm 4\%$  volume modulation measured via fast time-resolved infrared spectroscopy as function of the *m*-xylene uptake at constant *p*-xylene partial pressure of 0.150 mbar at 373 K.

### Calculating permeabilities for *p*-xylene at 373 K

The number of pore openings per m<sup>2</sup> for a-, b- and c- oriented MFI crystals are calculated from the unit cell dimensions.

Table S6.1: MFI unit cell parameters

MFI unit cell parameter	Length [nm]
a	2.009
b	1.974
c	1.314

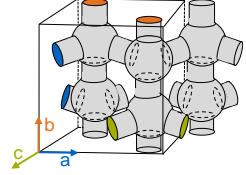


Table S6.2: Calculated surface areas for each unit cell plane.

Channel Orientation	Unit Cell Plane	Surface Area [nm <sup>2</sup> ]
a-orientation	b · c	2.594
b-orientation	a · c	2.640
c-orientation	a · b	3.966

As every unit cell plane contains two pore openings, the number of pore openings per surface area is calculated according to:

$$N_{open/surf,i} = \frac{2}{A_{u.c.plain i}} \quad (S6.1)$$

with *i* denoting one channel orientation.

The flux *j* of *p*-xylene molecules under the applied conditions is calculated by:

$$j_i = \frac{N_{open/surf,i}}{\tau_i \cdot N_A} \quad (S6.2)$$

with  $\tau_i$  being the sorption time constant for channel orientation *i* and  $N_A$  the Avogadro constant.

The permeability *P* is then calculated by:

$$P_i = J_i / \Delta p \quad (S6.3)$$

with  $\Delta p = 1.35$  Pa being the pressure change in the system due to volume modulation.

Table S6.3: Calculated *p*-xylene flux and permeability for each channel

Channel Orientation	$N_{open/surf,i} \cdot 10^{-17}$ [m <sup>2</sup> ]	$j \cdot 10^8$ [mol·m <sup>-2</sup> ·s <sup>-1</sup> ]	$P \cdot 10^8$ [mol·m <sup>-2</sup> ·s <sup>-1</sup> ·Pa <sup>-1</sup> ]
a-orientation	7.71	1.56	1.16
b-orientation	7.58	12.6	9.32
c-orientation	5.04	1.02	0.76

### Calculating the concentration of pore openings for individual MFI channel

The total surface area given by the B.E.T. measurement (39 m<sup>2</sup>·g<sup>-1</sup>) is the sum of the areas corresponding to straight, sinusoidal, and cut sinusoidal channel.

$$A_{B.E.T.} = \frac{A_{crystal}}{m_{crystal}} = \frac{A_{crystal, str.} + A_{crystal, sin.} + A_{crystal, cut}}{m_{crystal}} \quad (S6.4)$$

The ratio between the channel specific areas is determined by the side ratio of the crystallite obtained via SEM. For the geometry and side ratio described here (1 : 1.4 : 1.5 : 1 = *x* · *y* · *z* · *h* axis), the areas are given by:

$$A_{str.} = 2 \cdot x \cdot y + y \cdot (z - x) = 3.5x^2 \quad (S6.5)$$

$$A_{sin.} = 2 \cdot z \cdot h = 3.0x^2 \quad (S6.6)$$

$$A_{cut.} = 2 \cdot y \cdot h = 2.8x^2 \quad (S6.7)$$

From the side ratio of 3.5 : 3.0 : 2.8 ( $A_{str.} : A_{sin.} : A_{cut.}$ ) the absolute values for  $A_{str.}$ ,  $A_{sin.}$  and  $A_{cut.}$  can be calculated based on Equation S6.4. The concentration of pore openings for each channel is derived based on Equation 6.1.

## 6.6. Associated content

This chapter is based on a peer reviewed article.

Reprinted (minor changes) with permission from (M. Baumgärtl, A. Jentys, and J. A. Lercher. "Understanding Elementary Steps of Transport of Xylene Mixtures in ZSM-5 Zeolites." *The Journal of Physical Chemistry C* 123.13 (2018): 8092-8100) Copyright (2018) American Chemical Society.

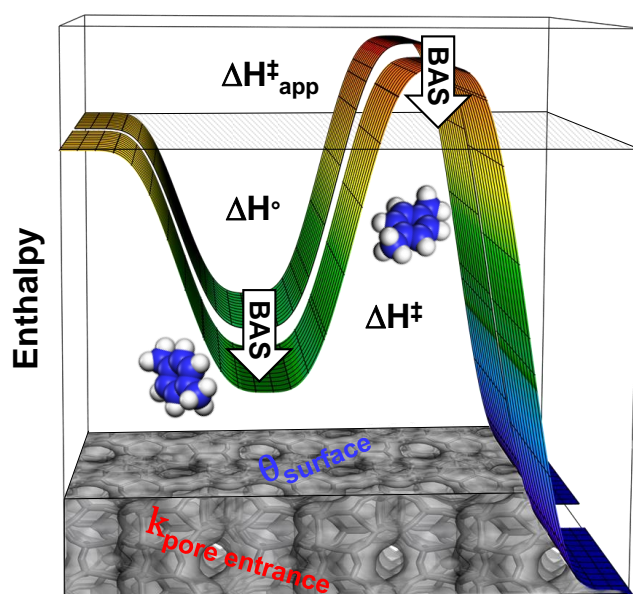
### Contributions

M. Baumgärtl did the zeolite synthesis, the transport experiments, adsorption isotherms, quantification, and calculations presented. T. Ikuno contributed the SEM images. M. Baumgärtl, A. Jentys and J.A. Lercher conceived the research. The manuscript was written through contributions of all authors.

### Acknowledgements

The financial support from the Deutsche Forschungsgemeinschaft DFG Project JE 260/12 is highly acknowledged. The authors are also grateful to Takaaki Ikuno for conducting the SEM measurements.

## 7. Influence of Acid Sites on Xylene Transport in MFI Type Zeolites



The influence of Brønsted acidic sites at the pore entrance of MFI type zeolites on the transport of *p*-xylene was investigated by comparing the diffusion rates on samples with and without Al. The pore entrance rate is directly proportional to the concentration of molecules on the external surface. Brønsted acid sites lead to a higher sorption equilibrium constant of xylene because of stronger binding by about  $3 \text{ kJ}\cdot\text{mol}^{-1}$ , compared to a neutral surface. The stronger binding energy reduces the apparent but not the true energy of activation for the pore entrance step of *p*-xylene, leading to an enhanced pore entrance rate. Brønsted acid sites in the pores do not markedly influence the transport.

### 7.1. Introduction

Catalysis in nanoporous materials depends on the reaction rate at the active site but may be limited by mass transport of reactants and products. Both processes are interconnected, as active sites along diffusion pathways are involved in sorption and desorption of reactive substrates while converting these. [160-162] Understanding the relations between reaction and mass transport, therefore, is essential for developing catalytic processes and has stimulated significant fundamental research. [18, 163-165] In this context, several studies on the role of Brønsted acid sites on the intra-crystalline transport properties of aromatic molecules in ZSM-5 (MFI) [166, 167] reported that diffusivity in the channels decreases with increasing acid site concentration. This behavior have been attributed to stronger interactions between diffusing molecules and acid sites, leading to a prolonged residence time on these sites and, therefore, to lower transport rates. [167, 168] The MFI samples investigated in these studies consisted of crystallites in the micrometer range, for which intra-crystalline diffusion controls transport, [127, 169] while reactions at the surface and at the pore entrance hardly influence the overall transport process.

Despite the large pore volume of zeolites, transport processes involve the external surface, as sorption at the outer surface is a critical step in the transport from the gas phase to the sites in the micropores, especially for molecules whose critical diameter approaches the diameter of the pore. We have previously shown that the pore entrance step is rate determining for the transport of aromatics in crystallites of siliceous MFI below 300 nm diameter. [169] Because Brønsted acidic SiOHAl groups are the active sites for catalytic reactions such as xylene isomerization, [47, 117, 118] insight into the impact of these sites on the kinetics of the transport process is crucial for further catalyst design. Thus, we decided to investigate the role of Brønsted acid sites on the transport of molecules through the pores of MFI crystals. To address this experimentally, diffusion through MFI in presence and absence of SiOHAl sites was followed by fast time-resolved infrared spectroscopy. We determine transition state enthalpies and entropies for the *p*-xylene pore entrance in MFI with and without the presence of SiOHAl sites.

## 7.2. Experimental section

### 7.2.1. Materials

Small crystallite MFI type zeolites were synthesized via a hydrothermal synthesis as described previously. [169] Water, tetraethyl orthosilicate, and tetra propyl ammonium hydroxide (40% solution in water) were added together with the appropriate amount of sodium aluminate (for the Al containing sample; 3.1 mmol and 6.2 mmol for MFI-45 and MFI-27, respectively) at a mass-based ratio of 9:5:1 into a stainless-steel autoclave with PTFE inlay and aged under stirring at room temperature overnight. Hydrothermal synthesis was carried out at 443 K for 72 h at 30 rpm. After washing with deionized water, the samples were dried and calcined under synthetic air ( $100 \text{ mL}\cdot\text{min}^{-1}$ ) at 823 K for 8 h. [170] All samples were ion-exchanged three times with a 1 M ammonium nitrate solution for 5 h at 343 K under stirring, separated by centrifugation and dried at 343 K overnight. [138] Ammonium hexafluorosilicate solution was used to remove extra-framework aluminium from the pores of the zeolite according to reference [171]. To obtain the proton form of the zeolite, the materials were calcined at 823 K for 5 h under synthetic air ( $100 \text{ ml}\cdot\text{min}^{-1}$ ). The aluminium containing zeolites are denoted MFI-X, with X representing the Si/Al ratio obtained after AHFS treatment, determined by elemental analysis. The purely siliceous sample is denoted Si-MFI. IR spectra of the activated samples are given in the Supporting Information (Figure S7.1).

### 7.2.2. Physicochemical characterization

**Scanning electron microscopy:** Scanning electron microscopy (SEM) images were obtained with a JSM-7500 F microscope at a resolution of 1.4 nm and a magnification of  $1.0 \cdot 10^5$  at 2kV. The powdered samples were prepared by dropping an ultra-sonicated isopropanol suspension on copper tape.

**Concentration of pore openings:** The concentration of pore openings on the outer surface was determined analogous to the description in our previous study

by combining electron microscopy (Figure 7.2) and external BET surface area measurements. [169]

**Determination of Brønsted acid site concentration:** Concentration of Brønsted acidic SiOHAl sites (BAS) was determined by adsorption of pyridine followed by IR spectroscopy. Self-supporting wafers of the samples were evacuated for one hour at pressures below  $10^{-6}$  mbar at 723 K. Pyridine was adsorbed on the samples at an equilibrium pressure of  $10^{-1}$  mbar at 423 K. The concentration of BAS was determined from the integration of the band at  $1545\text{ cm}^{-1}$  of protonated pyridine using a molar extinction coefficient of  $0.73\text{ cm}^2\cdot\mu\text{mol}^{-1}$ . [172]

Mesitylene was chosen to quantify the concentration of externally accessible BAS, as this molecule is structurally similar to xylenes, but – due to a kinetic diameter of 0.86 nm – cannot enter the 10 membered-ring pore openings of MFI. [173] Therefore, it interacts only with the Brønsted acid sites accessible from the pore mouth region or within the mesopores. The concentration of these externally accessible BAS was determined from the decrease of the band at  $3608\text{ cm}^{-1}$ , assigned to the OH stretching vibration of the SiOHAl groups.

**Uptake on external surface area:** *m*-Xylene was chosen to estimate the *p*-xylene uptake on the external surface of the zeolite samples. The difference in heat of adsorption between *p*- and *m*-xylene for the adsorption on the external surface of MFI, estimated by calorimetric adsorption experiments on amorphous  $\text{SiO}_2$ , resulted in heats of adsorption of  $-45$  and  $-49\text{ kJ}\cdot\text{mol}^{-1}$  for *p*- and *m*-xylene, respectively. Based on these numbers and the measured equilibrium constants for *m*-xylene, the equilibrium constants and surface coverage of *p*-xylene for the zeolite samples were calculated.

## 7. Influence of Acid Sites on Xylene Transport in MFI Type Zeolites

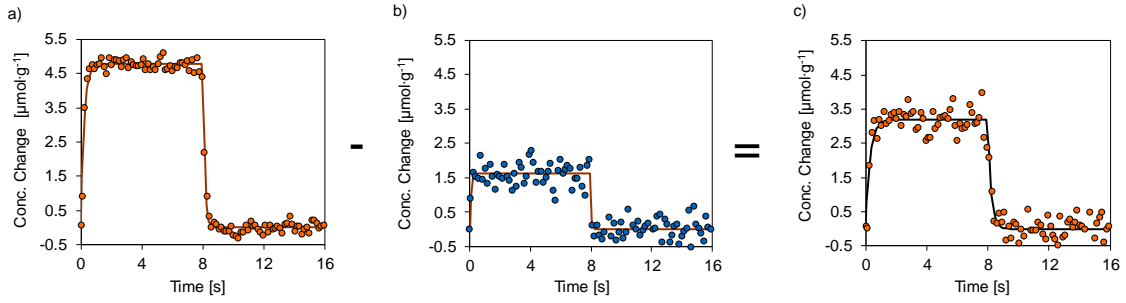


Figure 7.1: Xylene concentration profiles measured by infrared spectroscopy for a) *p*-xylene transport, b) *m*-xylene transport and c) *p*-xylene subtracted by *m*-xylene transport (pore entrance contribution).

### 7.2.3. Fast time-resolved IR spectroscopy

**Experimental setup and measuring principle:** Fast time-resolved IR spectroscopy was used to follow the sorption kinetics of *p*-xylene in MFI zeolites. For a detailed description of this method we refer to reference [169]. To obtain the concentration profiles of *p*-xylene and *m*-xylene the C–C stretching vibrations were integrated in the range of 1542-1475 cm<sup>-1</sup> and 1550-1422 cm<sup>-1</sup>, respectively. *p*-Xylene transport rates were derived from the initial slopes of the concentration time profiles according to the following equations.

Fit of adsorption:

$$\Delta c(t) = \Delta c_{eq} \left( 1 - e^{-\frac{t}{\tau_{ads}}} \right) \quad \forall \quad 0 < t \leq t_p/2 \quad (7.1)$$

Fit of desorption:

$$\Delta c(t) = \Delta c_{eq} \cdot e^{-\frac{t-t/2}{\tau_{des}}} \quad \forall \quad t_p/2 < t \leq t_p \quad (7.2)$$

With  $\Delta c(t)$  being the concentration difference between  $t=0$  and  $t$  and  $\Delta c_{eq}$  between the equilibrated states.  $\tau$  is the time constant for the sorption process. The measured concentration time profiles were fitted with Equation 7.1 and 7.2 using a least-square method. The derived parameters  $\Delta c_{eq}$  and  $\tau$  are used to calculate the transport rates. In this study only the adsorption process was investigated.

## 7. Influence of Acid Sites on Xylene Transport in MFI Type Zeolites

$$r_{ads} = \frac{d(\Delta c(t))}{dt} = \frac{\Delta c_{eq} \left(1 - e^{-\frac{t}{\tau_{ads}}}\right)}{\tau_{ads}} = \frac{\Delta c_{eq}}{\tau_{ads}} \quad (7.3)$$

The samples for IR spectroscopy were prepared by dispersing a zeolite sample in isopropanol and coating a CaF<sub>2</sub> infrared window with this suspension to prevent diffusion limitations in inter-particle pores. [169] Samples were activated at pressures below 10<sup>-6</sup> mbar at 673 K for 1 h prior to transport studies. Transport experiments with *p*-xylene were performed with pre-equilibrated samples in the pressure range on 0 to 4 mbar for temperatures of 323, 343 and 373 K applying a rectangular volume modulation with an amplitude of ± 4% and a modulation frequency of 1/16 s<sup>-1</sup>.

### 7.2.4. Determination of pore entrance rates

Volume modulation experiments followed by IR spectroscopy were used to monitor the dynamic changes in *p*-xylene uptake. The time-dependent concentration change is shown in Figure 7.1. The uptake rate observed in these experiments is a combination of adsorption on the external surface and in the pores. Spectroscopically, a differentiation between both processes is not possible, therefore, the contribution of the surface adsorption of *p*-xylene was estimated by using *m*-xylene, for which pore entrance can be excluded on the time scale of the transport experiment (periodicity of the volume perturbation 16 s) and subtracted from the *p*-xylene rate (containing both contributions) to obtain transport rates into the pores. To account for the differences in adsorption strength and surface coverage between *p*- and *m*-xylene, the measured *m*-xylene concentration profiles were corrected with the ratio of the equilibrium constants derived from the differences in heat of adsorption measured on SiO<sub>2</sub>. The rates derived from the total *p*-xylene uptake is referred to as *p*-xylene transport rate, the rate corrected by the surface adsorption term (*m*-xylene measurement) is referred to as pore entrance rate.

## 7.3. Results and discussion

### 7.3.1. Physicochemical characterization

Nominal specific surface areas of  $384 \text{ m}^2\cdot\text{g}^{-1}$ ,  $369 \text{ m}^2\cdot\text{g}^{-1}$ , and  $380 \text{ m}^2\cdot\text{g}^{-1}$  for the siliceous MFI (Si-MFI), MFI-45 and MFI-27 were determined by  $\text{N}_2$  physisorption. The external surface areas, determined by the benzene filling pore method, were  $39 \text{ m}^2\cdot\text{g}^{-1}$ ,  $63 \text{ m}^2\cdot\text{g}^{-1}$  and  $37 \text{ m}^2\cdot\text{g}^{-1}$  for Si-MFI, MFI-45 and MFI-27, respectively. The concentration of bridging hydroxyl groups (SiOHAl), determined by IR spectroscopy of adsorbed pyridine, were  $491 \text{ }\mu\text{mol}\cdot\text{g}^{-1}$  and  $369 \text{ }\mu\text{mol}\cdot\text{g}^{-1}$  for MFI-27 and MFI-45, with 6.3 % (MFI-27) and 4.1 % (MFI-45) of these sites being accessible from the external surface, as determined by IR spectroscopy of adsorbed mesitylene (Figure S7.2). The concentration of extra framework aluminum was determined by  $\text{Al}^{27}$ -NMR to 7.7% for both MFI-45 and MFI-27 (Figure S7.3). The larger external surface area for the MFI-45 sample reflects its rougher external surface (shown in SEM, Figure 7.2) compared to the Si-MFI and MFI-27 sample.

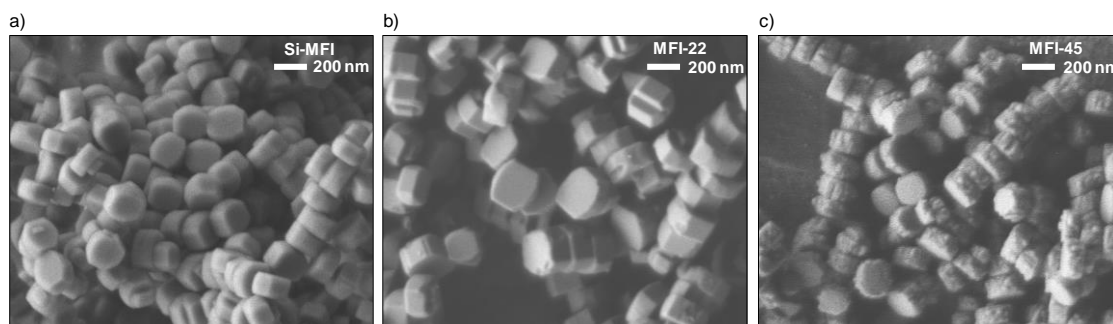


Figure 7.2: Scanning electron microscopy images of a) Si-MFI b) MFI-27 and c) MFI-45.

### 7.3.2. Concentration of pore openings

The overall concentration of pore openings (PO) was estimated to be  $45 \text{ }\mu\text{mol}\cdot\text{g}^{-1}$  consisting of  $19 \text{ }\mu\text{mol}\cdot\text{g}^{-1}$  straight and  $26 \text{ }\mu\text{mol}\cdot\text{g}^{-1}$  sinusoidal pore openings for Si-MFI,  $43 \text{ }\mu\text{mol}\cdot\text{g}^{-1}$  ( $19 \text{ }\mu\text{mol}\cdot\text{g}^{-1}$  straight and  $24 \text{ }\mu\text{mol}\cdot\text{g}^{-1}$  sinusoidal) pore openings for MFI-27 and  $71 \text{ }\mu\text{mol}\cdot\text{g}^{-1}$  ( $32 \text{ }\mu\text{mol}\cdot\text{g}^{-1}$  straight and  $39 \text{ }\mu\text{mol}\cdot\text{g}^{-1}$  sinusoidal) pore openings for the MFI-45 sample (details given in reference [169]).

To obtain the fraction of pore openings containing externally accessible Brønsted acid sites, the concentration of externally accessible BAS (determined by mesitylene adsorption) is divided by the concentration of pore openings. This results in a ratio of externally accessible Brønsted acid sites to pore openings of 74% for MFI-27 and 21% for MFI-45 (i.e., 3/4 and 1/5 of the pores openings contained an externally accessible SiOHAl group, respectively). While this indicates evenly distributed aluminium throughout the MFI-27 sample (inside and outside), the MFI-45 sample is slightly aluminium deficient on the external surface.

### 7.3.3. *p*-Xylene sorption

*p*-Xylene adsorption on the three materials (Figure 7.3 a) at low pressure ( $p < 1$  mbar) showed a larger sorption equilibrium constant in presence of Brønsted acid sites, leading to a higher *p*-xylene uptake on the acidic materials at same partial pressure. After complete saturation of Brønsted acid sites with *p*-xylene at higher pressure ( $p > 1$  mbar) the isotherms proceed parallel, indicating the same equilibrium constant for sorption on intersection without BAS.

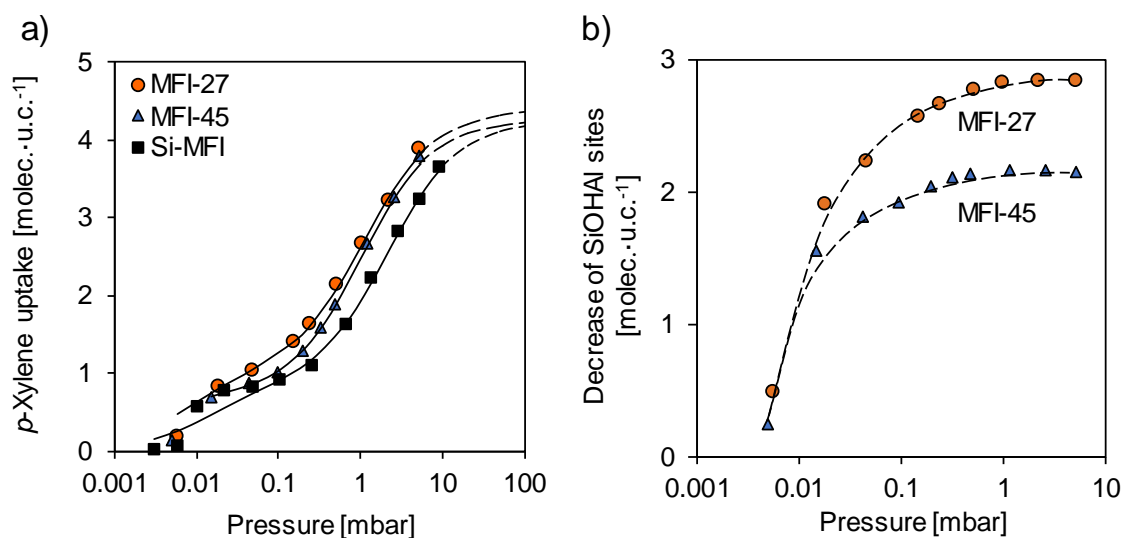


Figure 7.3: a) *p*-Xylene sorption isotherms for adsorption on Si-MFI (black) and MFI-45 (blue) and MFI-27 (orange) b) Decrease of SiOHAl sites (vibration at  $3610\text{ cm}^{-1}$ ) on MFI-45 and MFI-27 with *p*-xylene adsorption.

The preferential adsorption on SiOHAl sites is due to a higher heat of adsorption (3-5 kJ·mol<sup>-1</sup>), which is manifested in the saturation of SiOHAl sites already at 0.5 mbar (Figure 7.3 b). [158, 159]

#### 7.3.4. *m*-Xylene isotherms for sorption on external surface

To estimate the *p*-xylene coverage on the external surface, *m*-xylene was adsorbed, which rapidly equilibrated on the external surface, but did not enter the micropores on the time scale of the experiments. [18] This allows to spectroscopically differentiate the uptake rates on the surface and into the pores. Two components, i.e., the adsorption on non-porous sections and the adsorption at the pore mouth were differentiated from the isotherms for *m*-xylene adsorption on the external surface of MFI (Figure 7.4 and 7.5). Fitting the isotherm with a dual Langmuir model allows to separate the preferential adsorption of *m*-xylene on the pore mouth sites (i.e., a higher equilibrium constant), which is attributed to a higher enthalpic stabilization for the adsorbed molecules in the more confined environment. Unlike Si-MFI, on non-porous SiO<sub>2</sub> this contribution is missing and only surface adsorption was observed (described with a single Langmuir isotherm, Figure S7.4).

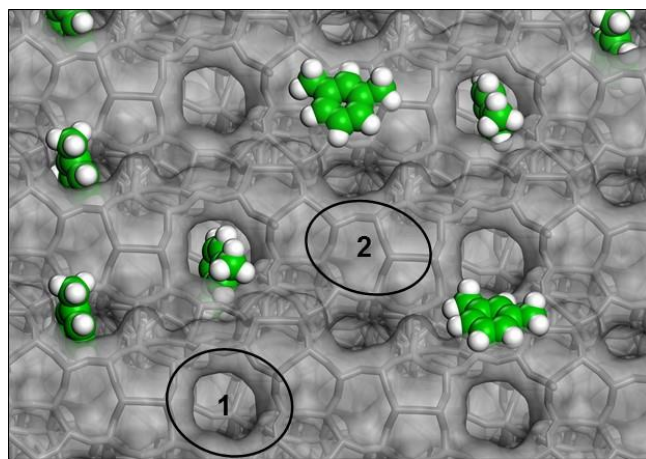


Figure 7.4: Illustration of the external surface of an MFI zeolite, indicating the location of the two different sorption sites at 1) the pore opening (PO) and 2) the non-porous section of the external surface.

## 7. Influence of Acid Sites on Xylene Transport in MFI Type Zeolites

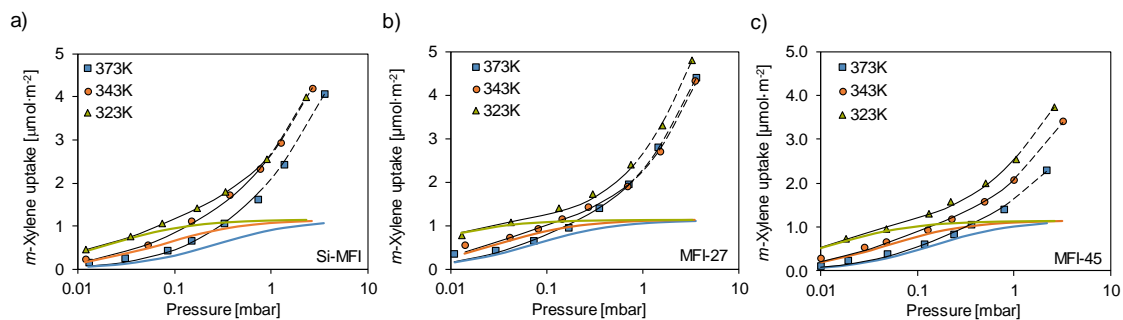


Figure 7.5: *m*-Xylene adsorption isotherms at 323, 343 and 373 K fitted by a dual Langmuir model (contributions for external surface without and with pore openings) for adsorption on a) Si-MFI and b) MFI-27 and c) MFI-45. The colored curves correspond to the *m*-xylene contribution adsorbed at the pore openings, the black line to the total uptake on the external surface. A direct comparison between MFI-27 and Si-MFI isotherms is included in the supporting information (Figure S5). As higher pressures and temperatures favor *m*-xylene pore entrances, the range above 1 mbar was not included in the calculations. This is indicated by the dashed line above 1 mbar.

The enthalpy and entropy ( $\Delta H^\circ$  and  $\Delta S^\circ$ ) of *m*-xylene adsorption at pore openings (PO) with and without Brønsted acid sites were derived from the temperature dependence of equilibrium constant obtained from fitting the adsorption isotherms (Table 7.1, Equation 7.4). Si-MFI was selected as the acid site free sample. The  $K$  values for a (hypothetical) sample with  $[\text{BAS}]_{\text{external}}/[\text{PO}]=1$  were extrapolated from equilibrium constants measured for Si-MFI, MFI-45 and MFI-27 (Figure 7.6 a, b).

## 7. Influence of Acid Sites on Xylene Transport in MFI Type Zeolites

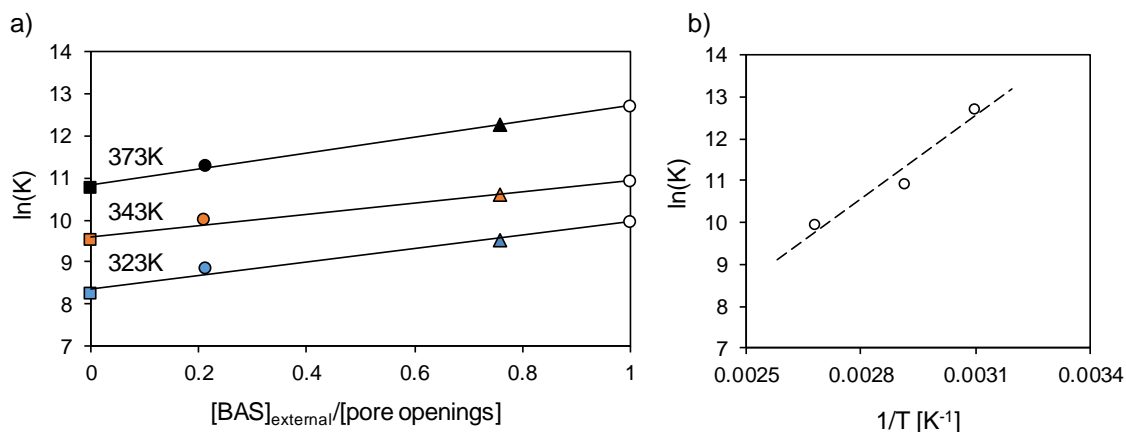


Figure 7.6: a) Dependency of equilibrium constants on acid site concentration per pore opening and temperature on Si-MFI (square), MFI-45 (circle) and MFI-27 (triangle). Extrapolated values to  $[BAS]_{\text{external}}/[PO]=1$  are given as open circles. b) van't Hoff plot for equilibrium constants extrapolated to  $[BAS]_{\text{external}}/[PO]=1$ .

Table 7.1: Equilibrium constants for *m*-xylene adsorption at MFI pore openings for Si-MFI, MFI-45, and MFI-27 as well as a hypothetical sample with  $[BAS]_{\text{external}}/[PO]=1$ .

	$K_{\text{pore entrance}} [10^3]$			$[BAS]_{\text{external}}/[PO] [\%]$
	323 K	343 K	373 K	
Si-MFI	47	14	3.7	0
MFI-45	82	22	7	21
MFI-27	210	40	14	74
extrapolated	340	57	21	100

$$K = e^{-\frac{\Delta H^0}{RT}} \cdot e^{\frac{\Delta S^0}{R}} \quad 7.4$$

The heats of adsorption for *m*-xylene at the pore opening with and without acid sites were  $-55 \text{ kJ}\cdot\text{mol}^{-1}$  and  $-51 \text{ kJ}\cdot\text{mol}^{-1}$ , respectively, indicating an additional contribution of  $4 \text{ kJ}\cdot\text{mol}^{-1}$  for the localized interaction with Brønsted acid sites. (Table 7.1). This difference leads to a substantial increase of surface coverage on MFI-27 for pressures below 0.3 mbar (Figure 7.5; Table 7.1). Heats of adsorption for *p*-xylene at pore openings with and without acid sites were calculated based on the respective values derived for *m*-xylene and the difference

in heat of adsorption between *p*- and *m*-xylene for amorphous silica (-45 and -49 kJ·mol<sup>-1</sup>; 8 %) (Table 7.2).

Table 7.2: Adsorption enthalpies and entropies for *p*-xylene adsorption at MFI pore openings (PO) with and without acid sites present.

[BAS] <sub>external</sub> /[PO] [%]	$\Delta H^\circ$ [kJ·mol <sup>-1</sup> ]	$\Delta S^\circ$ [J·mol <sup>-1</sup> ·K <sup>-1</sup> ]
0	-47	-68
100	-50	-66

### 7.3.5. *p*-Xylene transport

The concentration profiles for *p*-xylene during a pressure modulation over MFI-27 and Si-MFI are compared in Figure 7.7 and show a faster transport rate – indicated by a steeper initial slope – for the MFI sample containing acidic SiOHAl sites. These samples also show a higher uptake, related to the higher coverage under all pressures in this range (see *p*-xylene isotherm Figure 7.3).

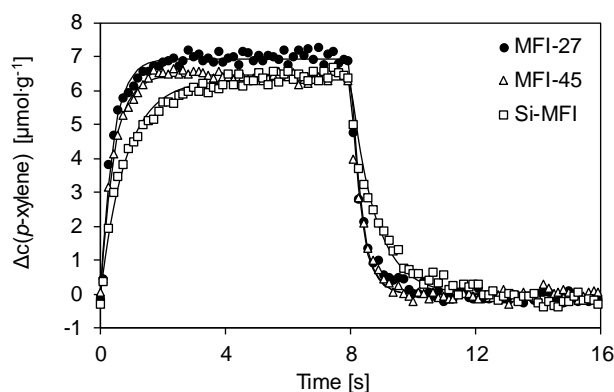


Figure 7.7: Concentration profile for *p*-xylene adsorbed on Si-MFI (open squares), MFI-45 (open triangles) and MFI-27 (filled circles). Adsorption process induced by square wave pressure perturbations with a modulation frequency of 1/16 s<sup>-1</sup> at a starting pressure of *p*-xylene of 0.3 mbar and 373 K.

## 7. Influence of Acid Sites on Xylene Transport in MFI Type Zeolites

The *p*-Xylene pore entrance rates were determined from the volume modulation experiments at different *p*-xylene partial pressures according to Equations 7.1-3 and the entropic and enthalpic barriers for the pore entrance were determined from the temperature dependence of these rate constants. The pore entrance rate linearly correlates with the surface concentration and can be described by a first order rate law (Figure 7.8, Equation 7.5).

$$\frac{r_{pore\ entr.}}{c_{0,PO}} = k_{pore\ entr.} \cdot c(p\text{-xylene})_{ext.\ surface} \quad 7.5$$

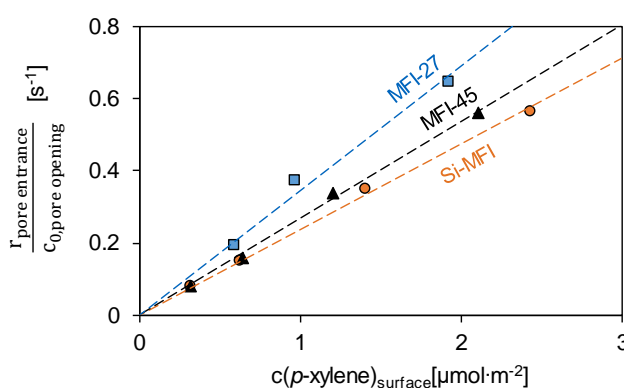


Figure 7.8: Normalized *p*-xylene pore entrance rates as a function of *p*-xylene surface concentration for Si-MFI (orange circles,  $k = 0.24 \frac{m^2}{\mu\text{mol}\cdot s}$ ), MFI-45 (black triangles,  $k = 0.29 \frac{m^2}{\mu\text{mol}\cdot s}$ ) and MFI-27 (blue squares,  $k = 0.35 \frac{m^2}{\mu\text{mol}\cdot s}$ ) at 373 K.

The apparent transition state barriers for *p*-xylene transport into pore openings with and without Brønsted acid sites were derived from the temperature dependence of the rate constants measured for Si-MFI, MFI-45 and MFI-27 (Table 7.3-4, Figure 7.9).

## 7. Influence of Acid Sites on Xylene Transport in MFI Type Zeolites

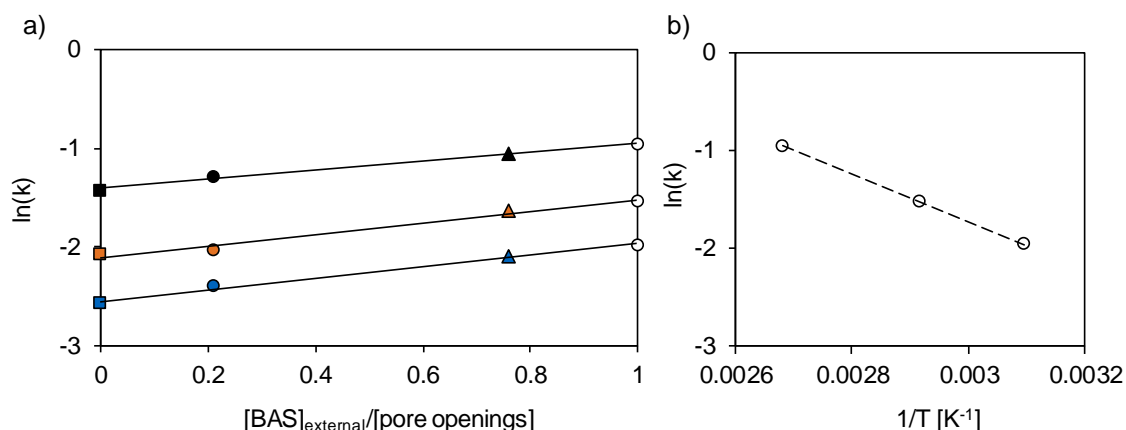


Figure 7.9: a) Dependence of rate constants on acid site concentration per pore opening and temperature determined from Si-MFI (square), MFI-45 (full circle) and MFI-27 (triangle). Extrapolated values to  $[BAS]_{\text{external}}/[PO]=1$  are given as open circles. b) Eyring plot for rate constants extrapolated to  $[BAS]_{\text{external}}/[PO]=1$ .

Table 7.3: Rate constants for *p*-xylene pore entrance for Si-MFI, MFI-45 and MFI-27 as well as a hypothetical sample with  $[BAS]/[PO]=1$ .

	$k_{\text{pore entr.}} \left[ \frac{\text{m}^2}{\mu\text{mol}\cdot\text{s}} \right]$			$[BAS]_{\text{external}}/[PO]$
	323 K	343 K	373 K	
Si-MFI	0.08	0.13	0.24	0
MFI-45	0.09	0.13	0.29	0.21
MFI-27	0.12	0.20	0.35	0.74
extrapolated	0.14	0.22	0.38	1.00

Table 7.4: Apparent and true transition state entropies, enthalpies, and free energies for the *p*-xylene pore entrance with and without a SiOHAl sites present at the pore opening.

$[BAS]_{\text{external}}/[PO]$	$\Delta H^{\ddagger}_{\text{app}} [\text{kJ}\cdot\text{mol}^{-1}]$	$\Delta S^{\ddagger}_{\text{app}} [\text{J}\cdot\text{mol}^{-1}\cdot\text{K}^{-1}]$	$\Delta H^{\ddagger} [\text{kJ}\cdot\text{mol}^{-1}]$
0	20	-205	67
1	17	-208	67

## 7. Influence of Acid Sites on Xylene Transport in MFI Type Zeolites

For a first order reaction the apparent reaction barrier is determined by the difference between the true barrier (for the elemental step) and the heat of adsorption (Equation 7.6). [76]

$$\Delta H_{true}^{\ddagger} = \Delta H_{app}^{\ddagger} - \Delta H_{ads}^0 \quad 7.6$$

The apparent enthalpic barrier for *p*-Xylene pore entrance into the Si-MFI sample is 3 kJ·mol<sup>-1</sup> higher compared to transport through pores with SiOHAl sites. The energy diagrams for the transport of *p*-xylene into Si-MFI and MFI samples are compared in Figure 7.9.

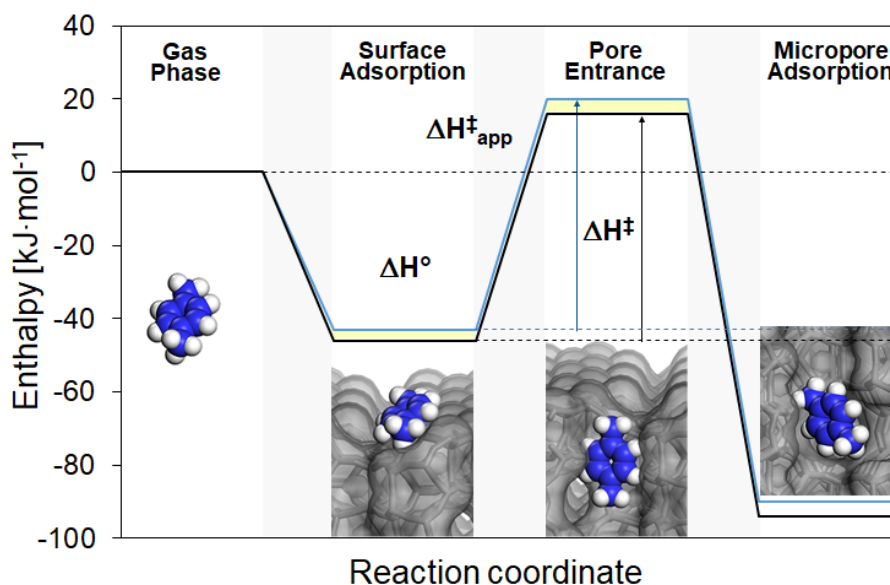


Figure 7.10: Energy profiles for the *p*-xylene transport into the micropores of MFI zeolites. *p*-Xylene transport involving a SiOHAl site on the surface (black) and on the purely siliceous material (blue) are included.

While the apparent barrier for the transport of *p*-xylene into Si-MFI is larger, the true barriers are identical for the transport of *p*-xylene in pores with and without SiOHAl sites, indicating that the SiOHAl sites stabilize ground and transition state in an identical way (Figure 7.10).

## 7. Influence of Acid Sites on Xylene Transport in MFI Type Zeolites

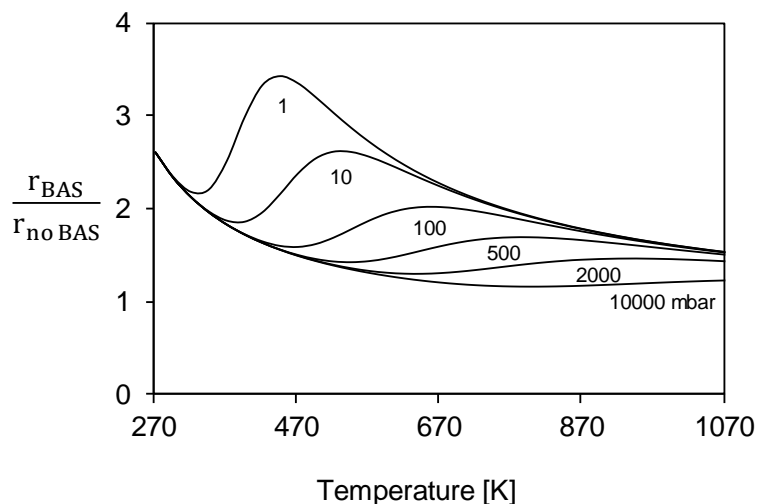


Figure 7.11: Relative increase in pore entrance rate in presence of externally accessible acid sites as function of temperature and pressure.  $r_{BAS}$  is the pore entrance rate for  $[BAS]_{\text{external}}/[PO]=1$ . A detailed description of the rate calculation is shown in the supporting information.

Based on the energy profile, pore entrance rates for a pure *p*-xylene/MFI system were extrapolated in a broad range of (catalytically relevant) temperatures and pressures (Figure 7.11). As shown in Equation 7.5, the pore entrance rate is defined by the product of rate constant and surface coverage. When starting from low temperatures, the pore entrance rate in presence of acid sites initially decreases because of a decrease in the ratio between  $\frac{k_{BAS}}{k_{no\ BAS}}$  with increasing temperature (Figure S7.6), as higher temperatures generally favor the rate of the reaction with the higher apparent energy barrier (in this case the non-acidic material over the acidic one). With increasing temperature, the ratio between the rates ( $\frac{\Gamma_{BAS}}{\Gamma_{no\ BAS}}$ ) reached a maximum (i.e., at 500 K for 1 mbar), which is the result of the higher surface coverage for adsorption on acidic compared to non-acidic materials (Figure S7.6). Note that for low temperatures, both acidic and non-acidic surface sites are fully covered, leading to  $\frac{\theta_{BAS}}{\theta_{no\ BAS}} = 1$ . With increasing temperature, the coverage of the non-acidic surface will decrease stronger compared with the acidic surface due the weaker interaction (increase in  $\frac{\theta_{BAS}}{\theta_{no\ BAS}}$ ), while at higher temperatures the isobars get less steep and the differences

## 7. Influence of Acid Sites on Xylene Transport in MFI Type Zeolites

between them gets smaller (decrease in  $\frac{\theta_{BAS}}{\theta_{no\ BAS}}$ ). For higher pressures, this maximum becomes less pronounced, as higher temperatures are required to reach the steep part of the isobar, resulting in a lower ratio between  $\frac{K_{BAS}}{K_{no\ BAS}}$  (see isobars Figure S7.7). This estimation indicates that for low partial pressures of *p*-xylene (1-10 mbar) and typical xylene isomerization temperatures (500-700 K), [133] the pore entrance rate can be increased by externally accessible Brønsted acid sites by a factor of 3-4 (Figure 7.11).

## 7.4. Conclusion

The presence of externally accessible SiOHAl sites increases the pore entrance rate by increasing the sorption strength on the external surface. The stronger interaction of *p*-xylene with acidic SiOHAl surface sites results in an energetically preferred sorption state ( $3 \text{ kJ}\cdot\text{mol}^{-1}$ ), leading to a higher surface coverage and a lower apparent transition state barrier ( $-3 \text{ kJ}\cdot\text{mol}^{-1}$ ) compared to the purely siliceous sample. A higher first order rate constant for the pores entrance rate with SiOHAl sites and, therefore, a faster mass transport into the micropores of the zeolite was observed. Although the apparent energy barrier for the pore entrance step of *p*-xylene was reduced by externally accessible SiOHAl sites, the true energy of activation was identical for acidic and on non-acidic materials, pointing towards the same pore entrance mechanism for pores with and without acidic sites present. Extrapolation to catalytically relevant temperatures and pressures showed that the presence of SiOHAl sites at the pore entrances can increase the transport rate of *p*-xylene by a factor of four.

## 7.5. Supporting information

### IR spectra

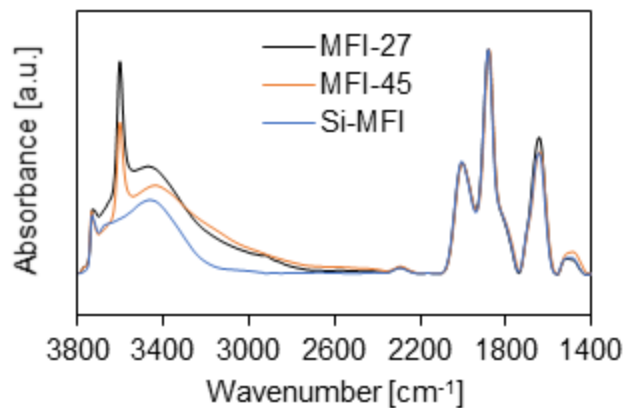


Figure S7.1: IR spectra of zeolite samples at 373K and pressures below 10<sup>-6</sup> mbar after activation at pressures below 10<sup>-6</sup> mbar at 673 K for 1 h.

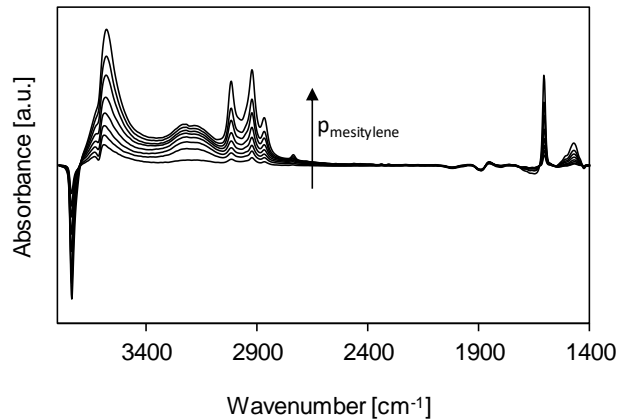


Figure S7.2: Series of differential infrared spectra of mesitylene adsorbed on MFI-27 at 323K.

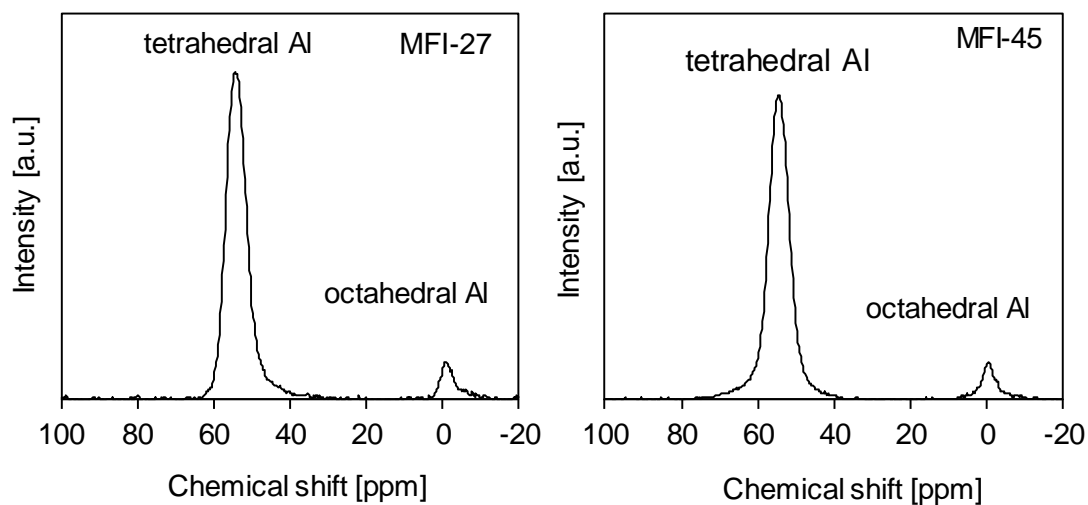
**Al<sup>27</sup>-NMR**

Figure S7.3:  $^{27}\text{Al}$ -NMR of MFI-27 (left) and MFI-45 (right). The octahedrally coordinated portion of aluminum was determined to 7.7% of the overall Al content for both samples.

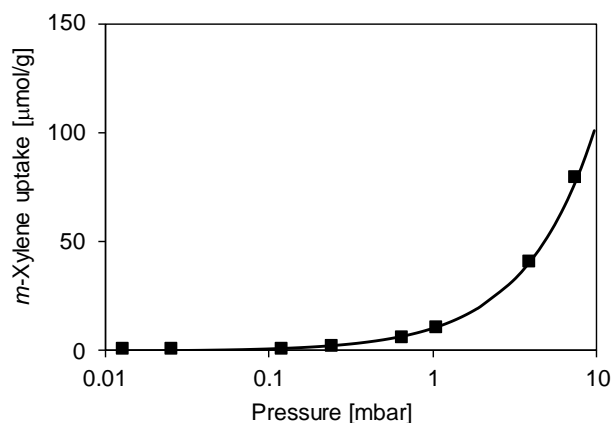


Figure S7.4: Isotherm for *p*-Xylene adsorption on amorphous  $\text{SiO}_2$  at 373 K. Note that the isotherm can be described perfectly by a single site adsorption Langmuir model.

## 7. Influence of Acid Sites on Xylene Transport in MFI Type Zeolites

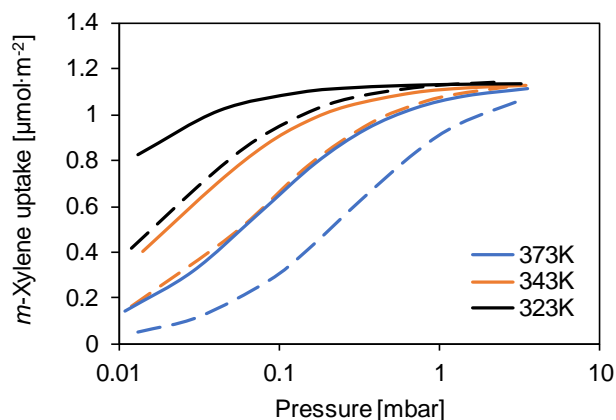


Figure S7.5: Comparison of *m*-xylene adsorption on pore openings for MFI-27 (straight) and Si-MFI (dashed) at different temperatures.

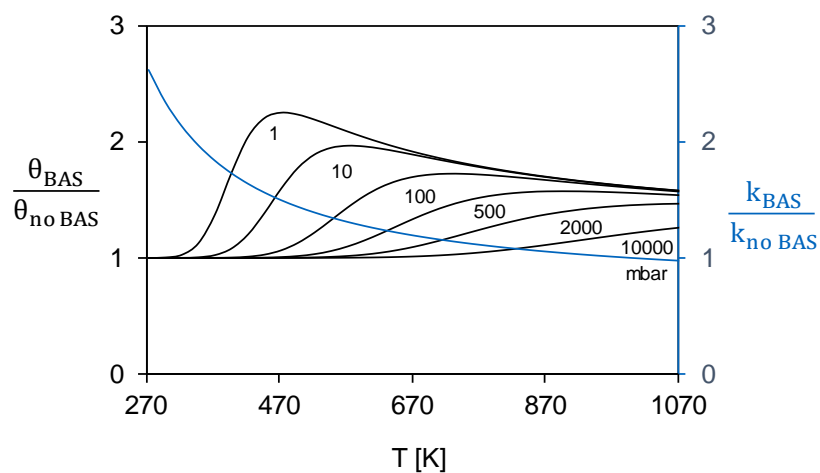


Figure S7.6: Relative increase in surface coverage (black) and rate constant (blue) in presence of externally accessible acid sites as function of temperature and pressure.

## 7. Influence of Acid Sites on Xylene Transport in MFI Type Zeolites

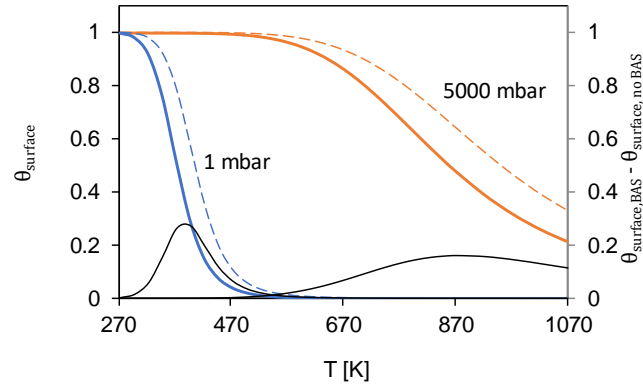


Figure S7.7: Isobars for *p*-xylene adsorption on acidic (dashed) and non-acidic (solid) external surface as well as differences in coverage between both materials (black line) for 1 and 5000 mbar.

### Extrapolation of transport rates

The used thermodynamic values ( $\Delta H^\ddagger$ ,  $\Delta S^\ddagger$ ,  $\Delta H^0$ ,  $\Delta S^0$ ) are listed in Table 7.2 and Table 7.4.

$$\frac{r_{pore\ entr.}}{c_{0,PO}} = k_{pore\ entr.} \cdot c(p\text{-xylene})_{ext.\ surf.} \quad 7.5$$

$$c(p\text{-xylene})_{ext.\ surf.} = c_0 \cdot \frac{Kp}{1 + Kp} \quad 7.7$$

with Equation 7.4 in 7.2

$$r_{pore\ entr.} = c_{0,PO} \cdot k_{pore\ entr.} \cdot c_0 \cdot \frac{Kp}{1 + Kp} \quad 7.8$$

$$\frac{r_1}{r_2} = \frac{k_{1,pore\ entr.} \cdot \frac{K_1p}{1 + K_1p}}{k_{2,pore\ entr.} \cdot \frac{K_2p}{1 + K_2p}} \quad 7.9$$

$$k = \frac{k_B T}{h} \cdot e^{-\frac{\Delta H^\ddagger}{RT}} \cdot e^{\frac{\Delta S^\ddagger}{R}} \quad 7.7$$

$$K = e^{-\frac{\Delta H^0}{RT}} \cdot e^{\frac{\Delta S^0}{R}} \quad 7.4$$

## 7.6. Associated content

This chapter is based on a peer reviewed article.

Reprinted (minor changes) with permission from (M. Baumgärtl, A. Jentys, and J. A. Lercher. "Influence of Acid Sites on Xylene Transport in MFI Type Zeolites." *The Journal of Physical Chemistry C* 124.7 (2020): 4134-4140.) Copyright (2020) American Chemical Society.

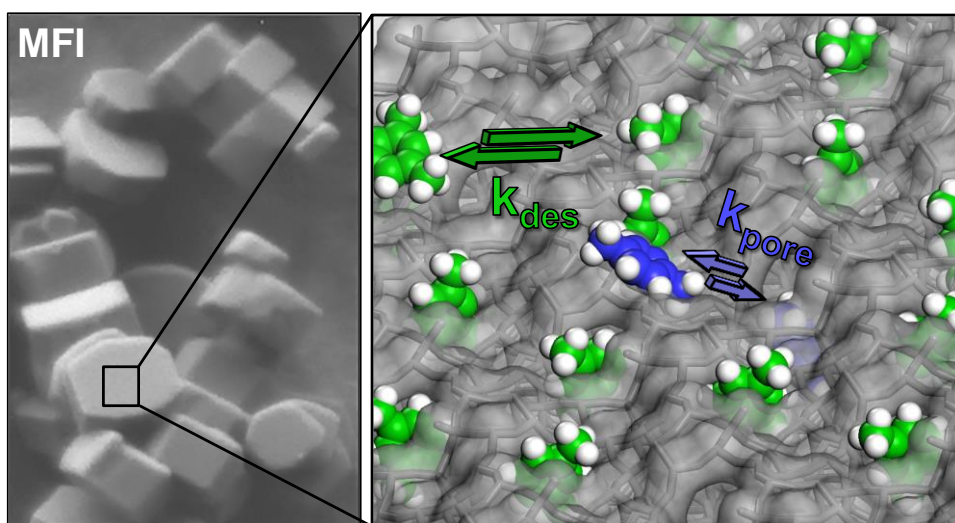
### Contributions

M. Baumgärtl did the zeolite synthesis, the transport experiments, adsorption isotherms, quantification, and calculations presented. T. Ikuno contributed the SEM images. T. Schachtl measured N<sub>2</sub>-Physisorption isotherms used for the calculation of BET. surface areas. M. Aigner measured the NMR spectra shown in Figure S7.3. M. Baumgärtl, A. Jentys and J.A. Lercher conceived the research. The manuscript was written through contributions of all authors.

### Acknowledgements

The financial support from the Deutsche Forschungsgemeinschaft DFG Project JE 260/12 is highly acknowledged. The authors are also grateful to Takaaki Ikuno for conducting SEM measurements, Teresa Schachtl for B.E.T. measurements and Martina Aigner for NMR measurements.

## 8. Surface Effects determining Transport in Binary Xylene Mixtures



The effect of adsorbed *m*-xylene on the *p*-xylene transport rate in MFI type zeolites with and without Brønsted acidic SiOHAl groups was investigated with and without isomerization occurring. At 373 K, *p*-xylene is hindered entering the pores by competitive adsorption of *m*-xylene, causing a low *p*-xylene surface coverage. The long residence time of *m*-xylene at pore openings compared to *p*-xylene statistically blocks the entrance for *p*-xylene under these conditions. The higher heat of *m*-xylene adsorption ( $58 \text{ kJ}\cdot\text{mol}^{-1}$ ) compared to the activation energy of the *p*-xylene pore entrance ( $18 \text{ kJ}\cdot\text{mol}^{-1}$  on MFI-27), strongly depletes the *m*-xylene coverage with increasing temperatures. At 453 K, the desorption rate constant of *m*-xylene and of the pore entrance of *p*-xylene are comparable and the *p*-xylene transport is not inhibited by *m*-xylene.

## 8.1. Introduction

Zeolites are an important group of catalysts, with active sites located in the micropores. [59, 174] During the reaction, molecules are transported from the gas phase to active sites in the pores. To avoid transport limitations, the transport rates of the substrate and product molecules must be equal or faster than the intrinsic reaction rate. The similarity of the zeolite pore diameters and the size of reacting molecules allow to realize shape selective reactions, utilizing subtle differences in diffusion coefficients between reactant and product molecules as well as limitations to the possible transition states of catalyzed conversions. Under those conditions reaction rates frequently approach and exceed transport rates in the micropores. [175]

For shape selective xylene isomerization or disproportionation, controlling the mass transport of xylene mixtures in medium pore zeolites like MFI is essential for ensuring high para selectivities. [48, 117-120] Xylene transport of single components in MFI has been investigated, [102, 127, 129, 132, 134, 137, 166, 176, 177] while multicomponent diffusion is far more challenging and less well understood. It is, for example, unclear, how the adsorption strength, molecule diameter, diffusivity, and framework type influence multicomponent diffusion. The *p*-xylene pore entrance rate shows a first order dependence on the concentration of externally adsorbed *p*-xylene for small crystallites where the rate determining step is the pore entrance. [178] Under these conditions, diffusion is directly proportional to the concentration of pore openings at the external surface and the *p*-xylene surface concentration. We have shown that the co-adsorption of *m*-xylene on the external surface reduces the overall *p*-xylene transport rate on MFI at 373 K by reducing the concentration of pore openings available for the *p*-xylene transport. [169] However, it remains unclear, by what mechanism *m*-xylene blocks sorption sites as adsorption of *m*- and *p*-xylene is equilibrated.

To understand the transport of xylenes during shape selective isomerization, *p*-xylene transport in binary mixtures with *m*-xylene was followed by fast time-resolved infrared spectroscopy for MFI in the presence and absence of SiOHAl sites under reactive (453 K) and non-reactive conditions (373 K). Thus, it is aimed

## 8. Surface Effects determining Transport in Binary Xylene Mixtures

not only to provide an in-depth understanding of the inhibition of *p*-xylene transport by *m*-xylene at 373 K, but also to better understand the impact of *m*-xylene present during isomerization at 453 K.

## 8.2. Experimental section

### 8.2.1. Materials

Small crystallite MFI type zeolites with a particle size of 150-200 nm and Si/Al ratios of 27 (MFI-27) and 34000 (Si-MFI) were synthesized as described previously. [169, 178]

A larger purely siliceous MFI zeolite with an average crystal size of 700 nm (Si-MFI/LC) was synthesized by adding 6.4 g of tetraethyl orthosilicate to a solution of 4.0g of tetra propyl ammonium hydroxide (40% solution in water) at room temperature. The dense gel was added to a solution of 1.0 g of tetra propyl ammonium bromide and 50 mL of deionized water. This mixture was aged at room temperature for 20 h under stirring. Hydrothermal synthesis was carried out at 453 K for 48 h at 30 rpm. After washing the samples with deionized water, they were dried and calcined under synthetic air ( $100 \text{ mL}\cdot\text{min}^{-1}$ ) at 823 K for 8 h.

A 1 M ammonium nitrate solution was used to ion-exchange all samples for 5 h at 343 K under stirring. After centrifugation, the samples were dried at 343 K overnight. [138] Extra-framework aluminium was removed from the pores of the zeolite with an Ammonium hexafluorosilicate solution according to ref. [171] The proton form of the zeolite was obtained by calcination at 823 K for 5 h under synthetic air ( $100 \text{ ml}\cdot\text{min}^{-1}$ ). The study the influence of externally accessible Brønsted acid sites tri-tert-butylphosphine was anchored on the SiOHAl groups via reaction from the gas phase. In this reaction the sample was activated at 673 K below  $10^{-7}$  mbar and exposed to tri-tert-butylphosphine for 1 h at 323 K. Subsequently the sample was evacuated for 1h at 673 K below  $10^{-7}$  mbar to remove physisorbed tri-tert-butylphosphine.

### 8.2.2. Physicochemical characterization

**Scanning electron microscopy:** Scanning electron microscopy (SEM) images were obtained with a JSM-7500 F microscope at a resolution of 1.4 nm and a

magnification of  $1.0 \cdot 10^5$  at 2kV. The powdered samples were prepared by dropping an ultra-sonicated isopropanol suspension on copper tape.

**Concentration of Brønsted acid sites (BAS):** The concentration of BAS was determined by pyridine adsorption followed by infrared spectroscopy. Samples were prepared as self-supporting wafers and activated at 723 K and pressures below  $10^{-6}$  mbar for one hour. Pyridine was adsorbed at 423 K and physisorbed pyridine was removed by subsequent evacuation. The band at  $1545 \text{ cm}^{-1}$  (protonated pyridine) was integrated to determine the BAS concentration using a molar extinction coefficient of  $0.73 \text{ cm}^2 \cdot \mu\text{mol}^{-1}$ . [172] The concentration of externally accessible BAS was quantified by mesitylene adsorption. [173, 178] monitoring the decrease of the OH stretching vibration of SiOHAl groups ( $3608 \text{ cm}^{-1}$ ).

### 8.2.3. Fast time-resolved IR spectroscopy

**Experimental setup and measuring principle:** The sorption kinetics of *p*-xylene in MFI zeolites were followed by fast time-resolved IR spectroscopy. The C–C stretching vibrations of *p*-xylene and *m*-xylene ( $1542\text{-}1475 \text{ cm}^{-1}$  and  $1550\text{-}1422 \text{ cm}^{-1}$ , respectively) were integrated for time resolved concentration profiles. From the initial slope of these concentration profiles *p*-Xylene transport rates were derived according to:

Adsorption:

$$\Delta c(t) = \Delta c_{eq}(1 - e^{-t \cdot k_x}) \quad \forall \quad 0 < t \leq \frac{t_p}{2} \quad (8.1)$$

Desorption:

$$\Delta c(t) = \Delta c_{eq} \cdot e^{-\left(\frac{t-t_p}{2}\right) \cdot k_x} \quad \forall \quad \frac{t_p}{2} < t \leq t_p \quad (8.2)$$

with  $\Delta c(t)$  being the concentration difference between  $t=0$  and  $t$  and  $\Delta c_{eq}$  between the equilibrated states A and A'. Assuming an equilibrium between A and B at  $t=0$ ,

## 8. Surface Effects determining Transport in Binary Xylene Mixtures

$$\frac{dc_A}{dt} = -k_{+1}c_{A(eq)} + k_{-1}c_{B(eq)} = 0 \quad (8.3)$$

with

$$k_{+1}c_{A(eq)} = k_{-1}c_{B(eq)} \quad (8.4)$$

During the volume modulation, a concentration change  $x$  is induced:

$$\begin{aligned} \frac{dc_A}{dt} &= -k_{+1}(c_{A(eq)} + x) + k_{-1}(c_{B(eq)} - x) \\ &= -k_{+1}c_{A(eq)} - k_{+1}x + k_{-1}c_{B(eq)} - k_{-1}x \end{aligned} \quad (8.5)$$

With Equation 8.4

$$\frac{dc_A}{dt} = -(k_{+1} + k_{-1})x \quad (8.6)$$

$$k_x = k_{+1} + k_{-1} \quad (8.7)$$

As

$$K = \frac{k_{+1}}{k_{-1}} \quad (8.8)$$

$$k_1 = \frac{Kk_x}{1 + K} \quad (8.9)$$

For  $K \gg 1$

$$k_1 \approx k_x \quad (8.10)$$

Equation 8.1 and 8.2 were used to fit the measured concentration time profiles.

The transport rate was calculated according to Equation 8.11.

$$r_{ads} = \Delta c_{eq}k_{+1} = \Delta c_{eq}k_x \quad (8.11)$$

Zeolite samples used for fast time-resolved IR spectroscopy studies were prepared by coating a CaF<sub>2</sub> infrared window with a suspension of the respective zeolite in isopropanol. Activation was done at pressures below 10<sup>-6</sup> mbar at 673 K for 1 h. [169, 178]

### 8.3. Results and discussion

#### 8.3.1. Physicochemical characterization

The surface areas and acid site concentrations for the investigated samples are summarized in Table 8.1:

Table 8.1: Physicochemical properties of investigated samples.

	$A_{\text{surface}}$ [ $\text{m}^2 \cdot \text{g}^{-1}$ ]	$A_{\text{external surface}}$ [ $\text{m}^2 \cdot \text{g}^{-1}$ ]	$c(\text{SiOHAl})$ [ $\mu\text{mol} \cdot \text{g}^{-1}$ ]	$c(\text{ext. SiOHAl})$ [ $\mu\text{mol} \cdot \text{g}^{-1}$ ]
Si-MFI	384	39	-	-
Si-MFI/LC	349	28	-	-
MFI-27	380	37	491	31

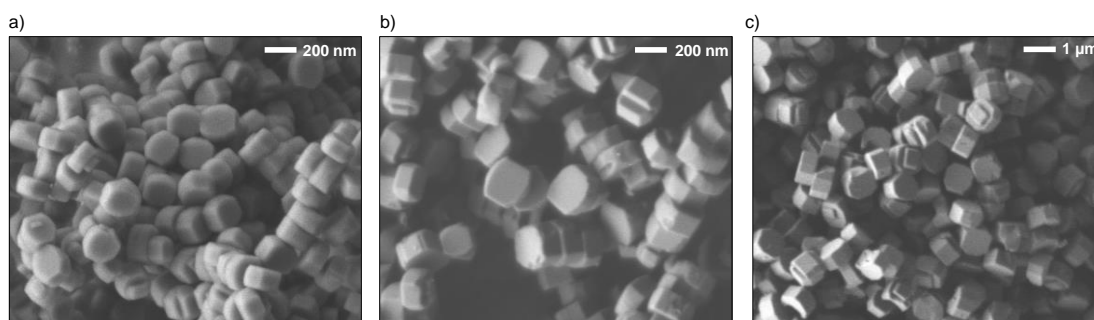


Figure 8.1: Scanning electron microscopy images of a) Si-MFI b) MFI-27 and c) Si-MFI/LC (larger crystallite).

### 8.3.2. Concentration of pore openings

The concentration of pore openings, determined from the external surface area and the crystallite geometry, is given in Table 8.2. [169, 178]

Table 8.2: Concentration of pore openings for investigated samples.

	c(pore openings) [ $\mu\text{mol}\cdot\text{g}^{-1}$ ]	c(straight openings) [ $\mu\text{mol}\cdot\text{g}^{-1}$ ]	c(sinusoidal openings) [ $\mu\text{mol}\cdot\text{g}^{-1}$ ]
Si-MFI	45	19	26
Si-MFI/LC	31	14	18
MFI-27	43	19	24

### 8.3.3. Binary sorption of xylenes

The transport of *p*-xylene in the presence of *m*-xylene in Si-MFI and MFI-27 was investigated by fast time-resolved infrared spectroscopy at 373 K and 453 K. Under these conditions the sorption of *m*- and *p*-xylene is equilibrated and both molecules are highly mobile on the surface, while only *p*-xylene can enter the pores on the time scale of the pressure modulation experiment.

As reported previously, [169] *p*-xylene transport is severely impeded by *m*-xylene adsorbed on the external surface of Si-MFI at 373 K (Figure 8.2a). This behavior holds also true in presence of BAS on MFI-27, where a higher transport rate for *p*-xylene was observed compared to Si-MFI at same *p*-xylene partial pressure. The preferential adsorption of *p*-xylene on SiOHAl sites leads to a higher surface coverage and following the first order rate process already reported to a higher sorption rate. [178]

## 8. Surface Effects determining Transport in Binary Xylene Mixtures

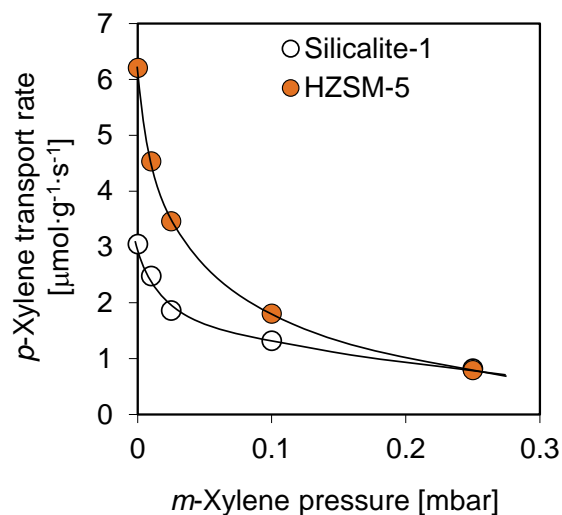


Figure 8.2: Influence of *m*-xylene partial pressure on *p*-xylene transport rate for Si-MFI (open symbols) and MFI-27 (orange symbols) at constant *p*-xylene partial pressure of 0.150 mbar. *m*-Xylene is located at the external surface due to short exposure time.

Due to the stronger interaction of hydrocarbons with acidic sites at the pore openings, the equilibrium constant for adsorption on the external surface for MFI-27 is higher than that of the siliceous MFI ( $K_{\text{Si-MFI}} = 3700$ ,  $K_{\text{MFI-27}} = 13600$  for *m*-xylene at 373 K). [158, 159] As *m*-xylene is slightly more basic than *p*-xylene (due to the higher electron density in the ring, resulting from the stronger inductive effect of the CH<sub>3</sub>-group in meta position), the surface concentration of *m*-xylene is higher than that of *p*-xylene at same partial pressure (Figure 8.3a).

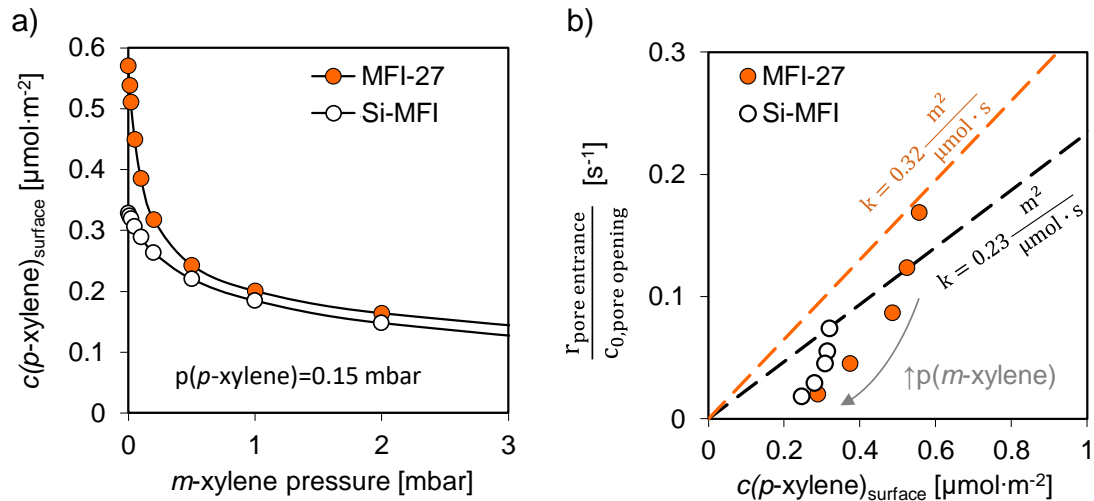


Figure 8.3: a) Competitive adsorption isotherm for *p*-xylene adsorption at the external surface for a constant *p*-xylene partial pressure of 0.15 mbar at 373 K. The isotherm was calculated with a Langmuir model based on the equilibrium constants derived in section 3.4. b) *p*-xylene transport rate for constant *p*-xylene pressure (0.15 mbar) as function of the *p*-Xylene external surface concentration at 373 K (combination of Figure 2 and 3a). Dashed lines represent the rate dependence found for the pure *p*-xylene situation for MFI-27 (orange) and Si-MFI (white). Note that the two points showing the estimated rate dependence on *p*-xylene for MFI-27 and Si-MFI (dashed lines) are measured without *m*-xylene.

A lower *p*-xylene surface concentration will lead in consequence to a lower transport rate into the pores. [178] In presence of *m*-xylene, the transport rate of *p*-xylene decreased stronger as predicted from the first order rate dependency and the *p*-xylene surface concentration (Figure 8.3b).

We have reported previously that *m*-xylene blocks pores for the *p*-xylene transport. [169] In order to effectively impede *p*-xylene transport by reducing the concentration of available pore openings, the average residence time of *m*-xylene at the pore openings must be significantly higher than the average time required for the pore entrance of *p*-xylene. If this boundary condition is not met, a rapid exchange between xylene isomers on the surface would eliminate the transport resistance induced by pore blocking.

The residence time of *m*-xylene at the external surface and at the pore openings was determined by desorption experiments in different pressure regimes for

## 8. Surface Effects determining Transport in Binary Xylene Mixtures

Si-MFI at 373 K. Evacuation from 0.1 to  $10^{-7}$  mbar primarily results in desorption from *m*-xylene adsorbed at the pore openings, whereas during a pressure reduction from 5.8 to 1.6 mbar *m*-xylene desorbs from sites at the external surface (Figure 8.4a). The desorption rate constants were calculated from the measured desorption rates according to Equation 8.12.

$$r_{des} = k_{des} \cdot c_{0,sites} \cdot \theta \quad 8.12$$

with  $c_{0,sites}$  being the concentration of surface sites and  $\theta$  the coverage of these sites by *m*-xylene molecules at respective partial pressure. The mean residence time of a molecule on the surface  $\tau_{surf}$  is defined by the rate of desorption and the concentration of molecules on the surface (Equation 8.13).

$$\tau_{surf} = \frac{c_{0,sites} \cdot \theta}{r_{des}} = \frac{1}{k_{des}} \quad 8.13$$

Table 8.3: Rate constants and average residence times for *m*-xylene on the outer surface of Si-MFI. Adsorption rate constants were derived from equilibrium constants according to  $K = \frac{k_{ads}}{k_{des}}$ .

adsorption at	$k_{ads}$ [ $s^{-1}$ ]	$k_{des}$ [ $s^{-1}$ ]	$\tau_{surf}$ [s]
external surface	993	5.7	0.2
pore opening	59	0.01	80

## 8. Surface Effects determining Transport in Binary Xylene Mixtures

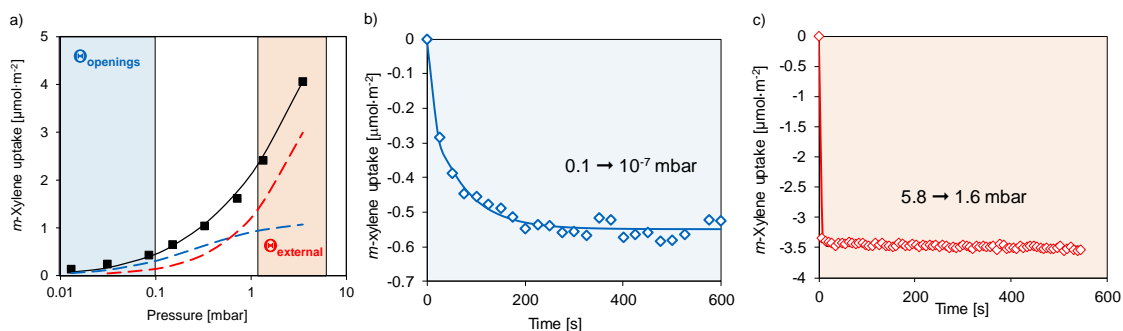


Figure 8.4: a) *m*-Xylene surface adsorption isotherm on Si-MFI (black) fitted with a dual site Langmuir adsorption model including a site at the pore opening (blue) and at the external surface (red) at 373 K. Blue and orange marked areas indicate the pressure range for the two desorption experiments. Concentration profiles for the *m*-xylene desorption induced by a pressure decrease b) from 0.1 to  $10^{-7}$  mbar and c) 5.8 to 1.6 mbar for Si-MFI.

A substantially slower desorption rate for molecules leaving the pore mouth sites compared to the molecules desorbing from the external surface was observed (Figure 4b and c) at 373 K. The stronger binding of xylenes adsorbed at the pore openings compared to the sorption on the external surface (indicated by a larger equilibrium constant and a preferential sorption) resulted in a longer residence time of *m*-xylene on the surface sites (Table 8.3). [178] Note that the average residence time of *m*-xylene at the pore opening was found to be 80 s at 0.15 mbar, which is 8 times larger compared to the average time for the pore entrance of *p*-xylene under the same conditions for Si-MFI and is sufficiently large to effectively impede the *p*-xylene transport by pore blocking. [169]

To compare the blocking of the pore entrance for a dynamic and an irreversible process, tri-tert-butyl phosphine (T<sup>t</sup>BP) was used to permanently block SiOHAl sites at pore openings. T<sup>t</sup>BP cannot enter the micropore channels of MFI because of the molecule dimensions and therefore, only binds (irreversibly) to SiOHAl sites at the pore opening positions accessible from the external surface. Infrared spectra of parent and T<sup>t</sup>BP modified sample are compared in Figure 8.5 a. The concentration of SiOHAl sites decreased by 7.2 % after T<sup>t</sup>BP modification (note that mesitylene adsorption indicated a fraction of 6.3 % for the externally accessible SiOHAl sites), while SiOH groups remained unaffected. With the phosphine modification, *p*-xylene transport rate decreased from  $6.8 \mu\text{mol}\cdot\text{g}^{-1}\cdot\text{s}^{-1}$

## 8. Surface Effects determining Transport in Binary Xylene Mixtures

to  $1.6 \mu\text{mol}\cdot\text{g}^{-1}\cdot\text{s}^{-1}$  for 0.15 mbar *p*-xylene at 373 K (Figure 8.5b). This decrease is in good agreement with the decrease observed when all external SiOHAl sites were covered by *m*-xylene (0.15 mbar). It allows us to conclude that *m*-xylene, although reversibly bound to the SiOHAl sites and equilibrated with the gas phase, can effectively block pore openings for *p*-xylene transport by competitive adsorption on the surface.

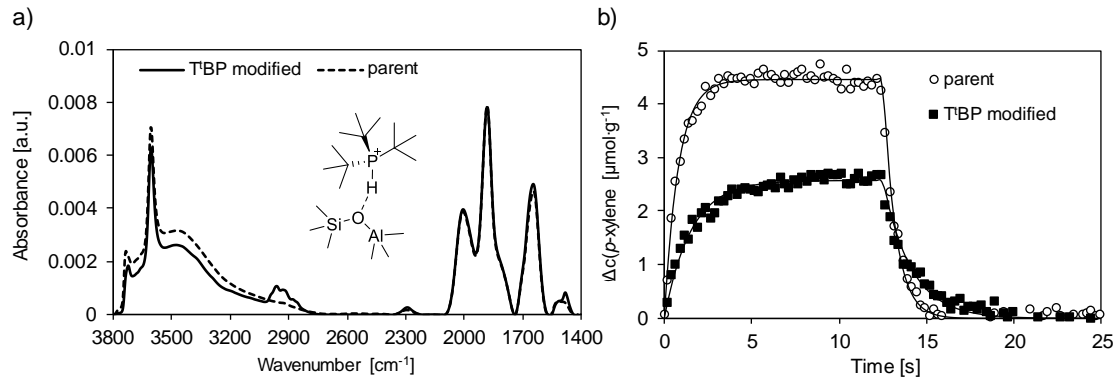


Figure 8.5: a) Infrared spectra of MFI-27 (parent material, dashed line) and TBP modified sample (solid line). A slight decrease of the SiOHAl vibration ( $3610 \text{ cm}^{-1}$ ) as well as the presence of the tert-butyl species, indicated by C–H and C–C stretching vibrations ( $2900\text{-}3030 \text{ cm}^{-1}$  and  $1450\text{-}1510 \text{ cm}^{-1}$ , respectively). b) Concentration profile for *p*-xylene adsorbed on the parent (open symbols) and TBP modified sample (filled symbols) from a starting pressure of *p*-xylene of 0.150 mbar.

Therefore, the concentration of pore openings available for the pore entrance is effectively reduced in presence of *m*-xylene. The fraction of pore openings (PO) available for the *p*-xylene transport  $\theta_{PO}^*$  (calculated using competitive Langmuir adsorption) was included in Equation 8.14. [178]

$$\frac{r_{pore\ entr.}}{c_{0, PO} \cdot \theta_{PO}^*} = k_{pore\ entr.} \cdot c(p\text{-xylene})_{ext.surf.} \quad 8.14$$

## 8. Surface Effects determining Transport in Binary Xylene Mixtures

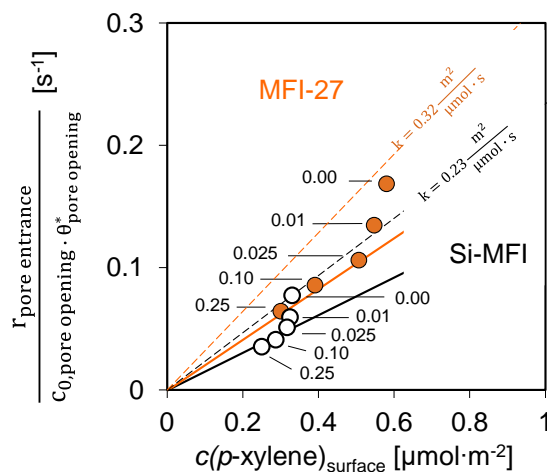


Figure 8.6: *p*-Xylene transport rate at 373 K and in presence of 0.15 mbar *p*-xylene and varying *m*-xylene partial pressures normalized to the concentration of available pore openings as function of the *p*-xylene surface concentration. Dashed lines represent the rate dependence found for the pure *p*-xylene system for MFI-27 (orange) and Si-MFI (black). [178] The corresponding *m*-xylene pressures in mbar are indicated.

Although the normalized pore entrance rates clearly show a better linear correlation to the *p*-xylene surface concentration (straight lines in Figure 8.6), for small *m*-xylene concentrations the results do not fit the proposed trend sufficiently. As previously shown by frequency response measurements, small amounts of *m*-xylene preferentially adsorb on straight channel pore openings. [169] As *p*-xylene transport in these channels is considerably faster compared to sinusoidal transport (8 times at 373 K and 0.15 mbar *p*-xylene partial pressure), blocking selectively straight channels reduces the overall transport rate stronger than predicted by rate constants and equilibrium constants averaged over all pore openings. It also shows that *p*-xylene uptake is controlled at the pore mouth and that a later change in direction (random transport at intersections) is inconsequential. The differentiation between straight and sinusoidal pore opening sites is spectroscopically not possible, and thus, rate constants could not be differentiated between channel types. Therefore, the dashed lines in Figure 8.6 represent the average rate constants with no pore blocking involved and blocking of the faster process in the straight channels in this case by adsorption of

## 8. Surface Effects determining Transport in Binary Xylene Mixtures

*m*-xylene will consequently lower the (average) rate constant (from dashed to straight lines in Figure 8.6) for the overall transport process.

To confirm the influence of a reduced concentration of pore openings on the *p*-xylene transport rate, we investigated a Si-MFI sample with larger crystallites (700 nm; Si-MFI/LC). As the ratio of volume to surface area increases with crystal size, the concentration of pore openings per mass is lower for larger crystallites. Note that after normalization of the pore entrance rate to the concentration of pore openings, the same rate constants for Si-MFI/LC and Si-MFI were found, confirming the observed first order rate dependence (Figure 8.7).

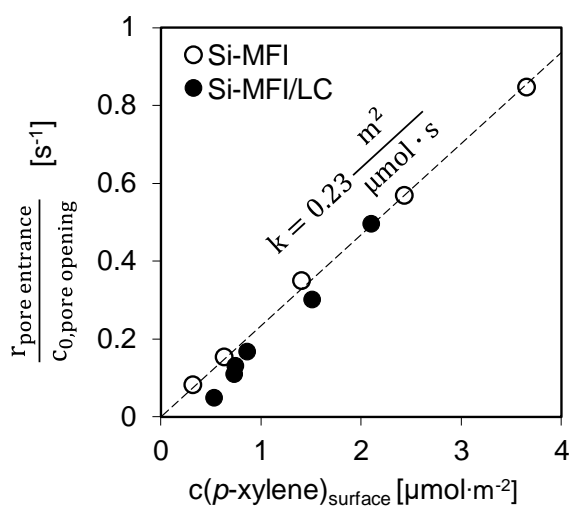


Figure 8.7: Normalized pore entrance rates vs. *p*-xylene surface concentration for two purely siliceous MFI samples with different concentration of pore openings due to different crystallite size.

We conclude, therefore, that the decrease of the transport rate in presence of *m*-xylene results from a competitive sorption at the pore openings. For benzene, which has the same kinetic diameter, but a considerably lower adsorption strength than *p*-xylene ( $-38 \text{ kJ}\cdot\text{mol}^{-1}$  vs.  $-45 \text{ kJ}\cdot\text{mol}^{-1}$  on amorphous  $\text{SiO}_2$ , determined by thermogravimetric measurements) a stronger inhibition of the transport rates at same *m*-xylene partial pressure was observed, (Figure S8.1).

After having studied the role of *m*-xylene on the transport we want to focus on the influence of competitively adsorbed *m*-xylene on the *p*-xylene transport under reactive conditions for the *p*-xylene isomerization at 453 K. In these experiments

## 8. Surface Effects determining Transport in Binary Xylene Mixtures

a wafer of MFI-27 was activated in vacuum below  $10^{-7}$  mbar at 673 K and 4 mbar of *p*-xylene were added at 453 K, mimicking a batch wise operation. The change in surface concentration for *p*- and *m*-xylene was monitored by IR spectroscopy as a function of time, while the gas phase composition was analyzed simultaneously by GC-FID. Over the course of the reaction, *p*-xylene transport rates were determined by short volume modulation experiments (7 min per experiment). The concentration of xylenes adsorbed on the zeolite (a) and in the gas phase (b) during *p*-xylene isomerization are shown in Figure 8.8. While *m*-xylene formed from isomerization of *p*-xylene can be initially detected on the zeolite surface by IR spectroscopy, the gas phase composition did not change during the first 200 minutes, which indicates that due to the low diffusivity, *m*-xylene formed inside the pores cannot leave the pores immediately and accumulates inside the zeolite. This effect leads to an increased coverage on acid sites during the first 200 min (Figure S8.2). For the *p*-xylene isomerization, a rate constant of  $0.15\text{ s}^{-1}$  was determined from the initial slope of the *p*-xylene concentration profile (Figure 8.8a).

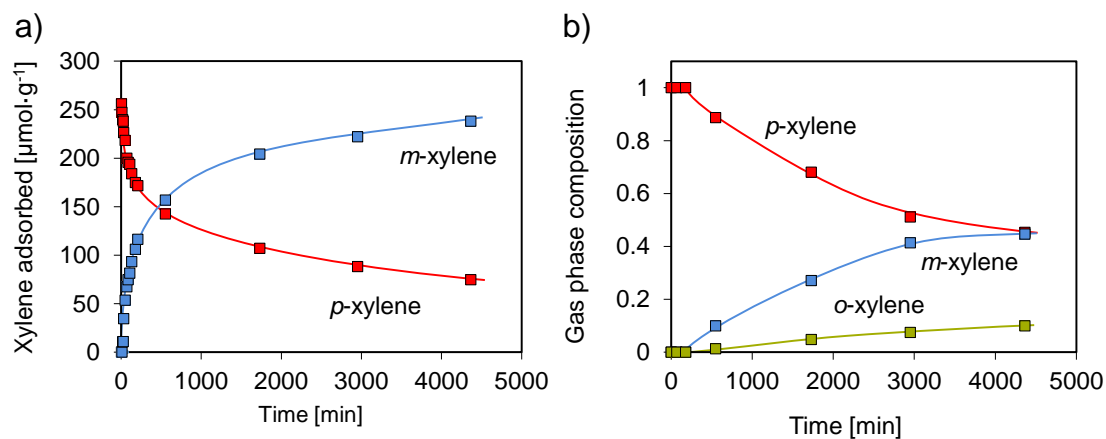


Figure 8.8: *p*-Xylene isomerization at 453 K and an initial *p*-xylene partial pressure of 4 mbar. a) Concentration profile for *p*-xylene (red), *m*-xylene (blue) and *o*-xylene (green) adsorbed on MFI-27 and b) in the gas phase during the reaction.

## 8. Surface Effects determining Transport in Binary Xylene Mixtures

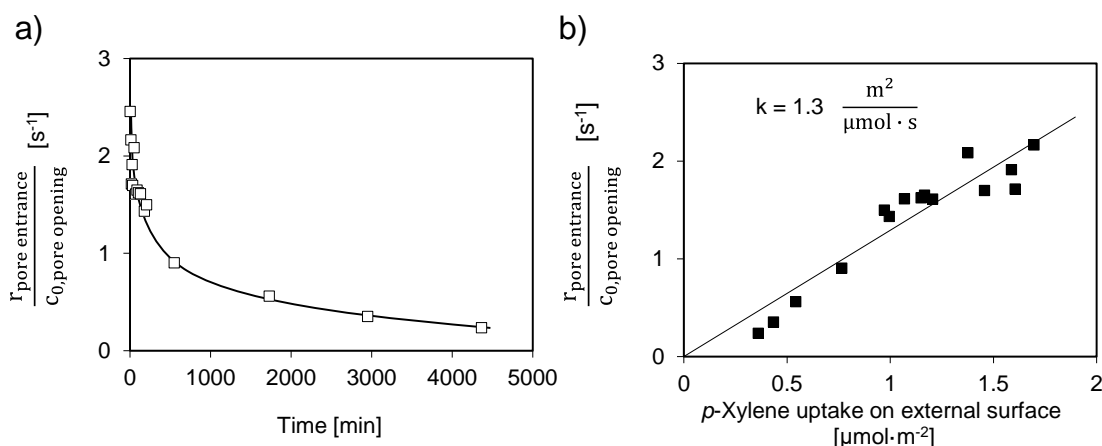


Figure 8.9: a) Evolution of  $p$ -xylene transport rate with reaction time. b)  $p$ -Xylene pore entrance rate normalized to the  $p$ -xylene concentration on the external surface.

Over the course of the reaction, the  $p$ -xylene transport rate decreased with increasing  $p$ -xylene conversion (Figure 8.9a). This was expected, since both an increasing  $m$ -xylene concentration as well as a decreasing  $p$ -xylene concentration should lower the  $p$ -xylene transport. To evaluate which effect is more pronounced under reaction conditions, the  $p$ -xylene transport rate was compared to the  $p$ -xylene surface concentration. A linear correlation between  $p$ -xylene transport rate and surface concentration was observed, typical for a first order reaction with no inhibition by  $m$ -xylene (Figure 8.9b).

Extrapolating recently published rate constants [178] for the  $p$ -xylene transport from 373 K to 453 K resulted in  $k_{\text{ext.}} = 1.3 \text{ m}^2\cdot\mu\text{mol}\cdot\text{s}^{-1}$ , which is in perfect agreement to the measured value ( $k = 1.3 \text{ m}^2\cdot\mu\text{mol}\cdot\text{s}^{-1}$ ). While this confirms that the  $p$ -xylene transport rate shows a first order rate dependence on the  $p$ -xylene surface concentration, it also indicates that the decrease of available pore openings by the presence of  $m$ -xylene leads to a transition from the kinetic to a diffusion-controlled regime at 453 K.

As mentioned above, pore blocking by  $m$ -xylene occurs because of the much larger residence time of  $m$ -xylene at the pore opening compared to the  $p$ -xylene pore entrance. From desorption experiments at temperatures between 373 and 453 K, an activation energy of  $58 \text{ kJ}\cdot\text{mol}^{-1}$  for  $m$ -xylene desorption from pore mouth sites was determined for MFI-27 (Figure S8.3). In consequence, a

## 8. Surface Effects determining Transport in Binary Xylene Mixtures

temperature increase from 373 to 453 K leads to a decrease in the *m*-xylene residence time at pore openings from 130s to 4s. At the same time, the *p*-xylene pore entrance time decreases from 6 s (373 K and 0.15 mbar *p*-xylene) to 0.5 – 2s (453 K and 4 – 2 mbar *p*-xylene), being in the same range as the *m*-xylene desorption rate. Consequently, an inhibition from pore blocking was not observed at 453 K.

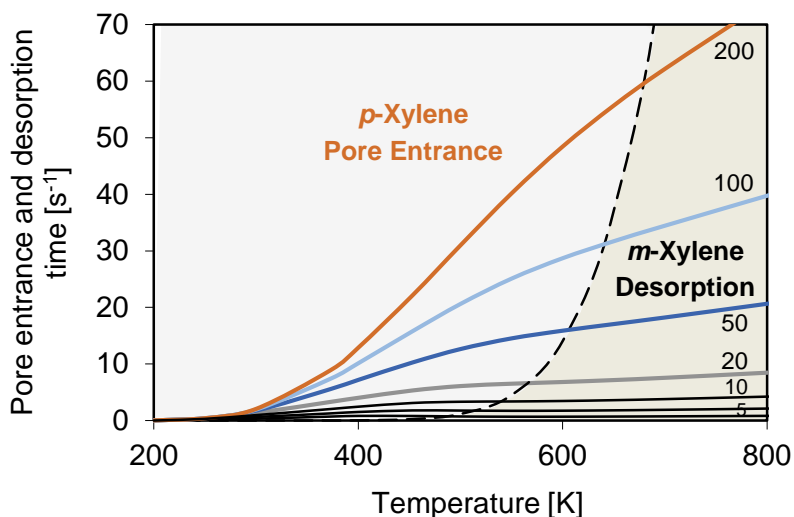


Figure 8.10: Calculated *p*-xylene pore entrance and *m*-xylene desorption times for various temperatures and *p*-xylene pressures. In grey areas the *p*-xylene pore entrance is faster, in orange areas the *m*-xylene desorption. Small numbers on the right side indicate *p*-xylene partial pressures in mbar.

The average pore entrance time depends on the *p*-xylene surface concentration and, therefore, on the *p*-xylene partial pressure in the gas phase. On the other hand, the average residence time of molecules on a surface is only a function of temperature, assuming a Langmuir type sorption model. The higher energy barrier for the *m*-xylene desorption compared to the *p*-xylene pore entrance (58 vs. 18 kJ·mol<sup>-1</sup>) leads to a less hindered system with increasing temperature. The temperature dependence of the *m*-xylene residence time and the *p*-xylene pore entrance time is illustrated in Figure 8.10. For temperatures below 500 K, *m*-xylene desorption is significantly slower compared to the *p*-xylene pore entrance for *p*-xylene partial pressures above 0.1 mbar, resulting in transport limitation in this temperature range (grey area in Figure 8.10). Above 670 K, the

## 8. Surface Effects determining Transport in Binary Xylene Mixtures

*p*-xylene pore entrance rate is lower than the *m*-xylene desorption rate and, thus, transport limitations from pore blocking of adsorbed *m*-xylene are not expected in this temperature range (beige area in Figure 8.10).

## 8.4. Conclusion

For binary xylene mixtures, *m*-xylene competes with *p*-xylene for sorption sites by stochastic competitive adsorption and reduces in this way the concentration of *p*-xylene on the surface. Under conditions when *m*-xylene desorbs much slower compared to the *p*-xylene pore entrance rate (low temperatures), the concentration of available pore openings for *p*-xylene transport is reduced effectively by pore blocking. Both contributions add up to a strong decrease in *p*-xylene transport rate in binary mixtures with *m*-xylene. This effect is stronger the lower the local interaction of the molecules with the surface is, i.e., smaller molecules like benzene instead of *p*-xylene, which due to a lower heat of adsorption, can be suppressed from the external surface more efficiently by a stronger adsorbing component like *m*-xylene. At elevated temperatures, the residence time of *m*-xylene is strongly reduced and, therefore, loses the ability to block pore openings for the *p*-xylene transport. Under these conditions, *m*-xylene does affect the pore entrance of *p*-xylene by reducing the surface concentration in a competitive manner, but not by reducing the concentration of available pore openings.

## 8.5. Supporting information

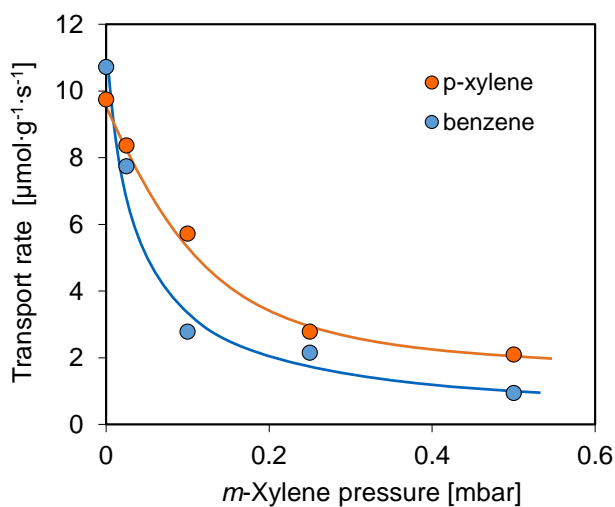


Figure S8.1: Comparison of *p*-xylene and benzene transport rates for Si-MFI in binary mixtures with *m*-xylene at 323 K. The partial pressure of *m*-xylene was varied at constant *p*-xylene or benzene partial pressure of 1.0 mbar.

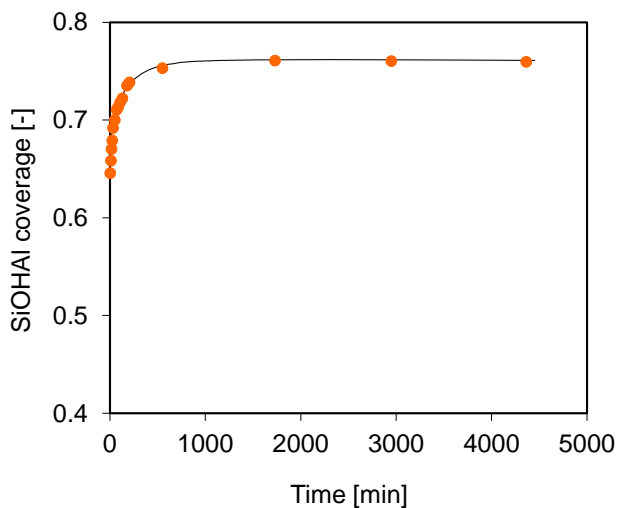


Figure S8.2: SiOHAl site coverage over the course of a *p*-xylene isomerization reaction (batch operation) at 453 K.

## 8. Surface Effects determining Transport in Binary Xylene Mixtures

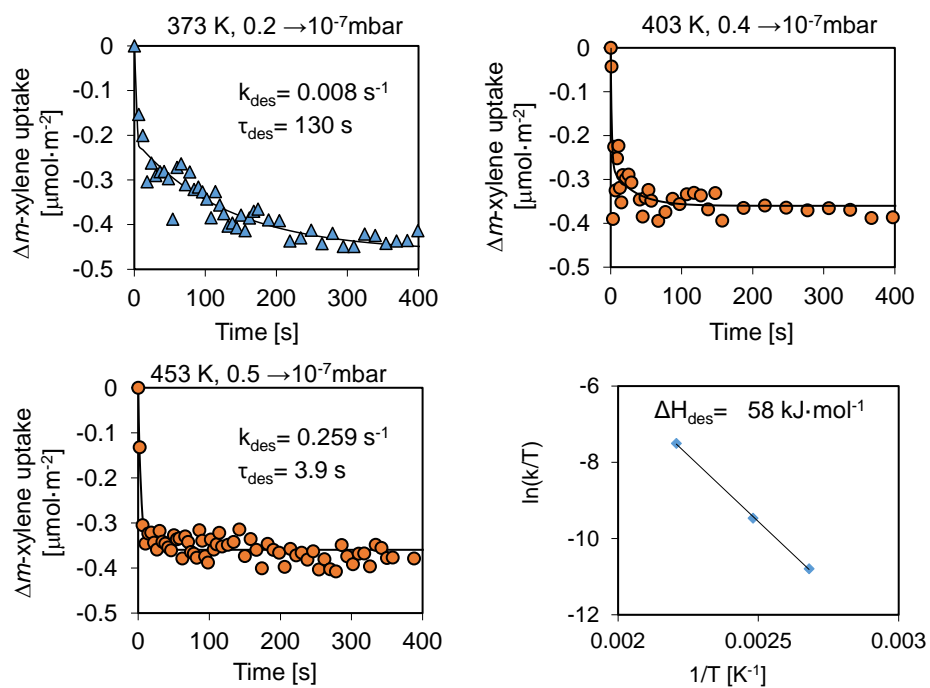


Figure S8.3: Desorption curves of *m*-xylene from the surface of MFI-27 to determine the energy barrier for the *m*-xylene desorption from the pore mouth site.

## 8.6. Associated content

This chapter is based on a peer reviewed article.

Reprinted (minor changes) with permission from (M. Baumgärtl, A. Jentys, and J. A. Lercher. "Surface Effects Determining Transport in Binary Xylene Mixtures." *The Journal of Physical Chemistry C* 124 (2020): 26814-26820.)  
Copyright (2020) American Chemical Society.

### Contributions

M. Baumgärtl did the zeolite synthesis, the transport experiments, adsorption isotherms, quantification, and calculations presented. T. Ikuno contributed the SEM images. M. Baumgärtl, A. Jentys and J.A. Lercher conceived the research. The manuscript was written through contributions of all authors.

### Acknowledgements

The financial support from the Deutsche Forschungsgemeinschaft DFG Project JE 260/12 is highly acknowledged.

## 9. Concluding Summary

Understanding mass transport of hydrocarbons in the nanoporous environment of zeolites is of great importance for a vast majority of industrially relevant processes. On the way from the gas phase to the catalytically active sites in the pore network, molecules must pass through a series of consecutive or parallel transport steps. For understanding the entire transport pathway, the individual transport steps and the parameters influencing them must be apprehended.

For the small MFI crystallites (< 250 nm) used in this study, the pore entrance step has been confirmed as the rate determining step for the xylene transport. The pore entrance rate has a first order dependence on the xylene concentration on the external surface and therefore increases with partial pressure. Due to a careful characterization of the external surface, equilibrium constants for the adsorption on different surface sites were feasible. This allowed for the determination of activation energies for the pore entrance with and without acid sites. An additional energetic contribution of 3 kJ/mol was measured for the adsorption of xylenes on Brønsted acid sites compared to a purely silicious material. This leads to a higher surface coverage at same partial pressure and therefore, to an enhanced pore entrance rate for zeolites with externally accessible acid sites.

For industrially applied processes, like the xylene isomerization over MFI, mixtures of xylene isomers are present. Due to the steric constraints of *m*- and *o*-xylene, transport in the pores of MFI is significantly slower for these isomers compared to *p*-xylene. For xylene mixtures, competitive adsorption on the external surface becomes a decisive factor determining the transport rate. Adding *m*-xylene to a *p*-xylene gas phase will reduce the para concentration on the external surface of the zeolite and lead to a reduced pore entrance rate compared to the single component system at same partial pressure. For conditions, where the desorption time of *m*-xylene is lower compared to the *p*-xylene pore entrance

(low temperatures and high pressures), *m*-xylene additionally blocks pore openings by quasi static adsorption. This additionally reduces the number of pore openings available for the pore entrance and therefore impedes the transport rate. As the activation energy for the desorption is higher compared the pore entrance, high temperatures favor the desorption and reduce transport limitations due to pore blocking.

# 10. Abschließende Zusammenfassung

Für eine Vielzahl großtechnisch relevanter Prozesse spielt der Transport von Kohlenwasserstoffen in der nanoporösen Umgebung von Zeolithen eine entscheidende Rolle. Auf dem Weg aus der Gasphase zu den katalytisch aktiven Zentren im Poreninneren müssen Moleküle eine Reihe aufeinanderfolgender oder parallel geschalteter Transportvorgänge durchlaufen. Um den gesamten Transportprozess zu verstehen, ist es wichtig die einzelnen Transportschritte und die Parameter, die diese beeinflussen zu begreifen.

Für die kleinen MFI Kristallite, welche in dieser Studie Verwendung fanden, konnte der Poreneintritt als geschwindigkeitsbestimmender Schritt für den Xylol Transport bestätigt werden. Dabei weist die Poreneintrittsrate eine Abhängigkeit erster Ordnung bezüglich der Oberflächenkonzentration an Xylol auf. Demzufolge wird die Poreneintrittsrate mit steigendem Partialdruck erhöht. Aufgrund einer genauen Charakterisierung der äußeren Oberfläche konnten Gleichgewichtskonstanten für die Adsorption von Xylol an verschiedenen Adsorptionszentren der äußeren Oberfläche bestimmt werden. Dadurch war es möglich Aktivierungsenergien für den Poreneintritt unter An- und Abwesenheit von Säurezentren zu bestimmen.

Für die Adsorption von Xylol an Brønsted Säurezentren wurde ein zusätzlicher energetischer Beitrag von 3 kJ/mol verglichen mit dem rein Silizium-basierten Material ermittelt. Diese erhöhte Adsorptionswärme führt zu einer höheren Oberflächenbedeckung bei gleichem Partialdruck und demzufolge zu einer erhöhten Poreneintrittsrate für Zeolithe mit extern zugänglichen Säurezentren.

Für industriell angewandte Prozesse wie der Xylol Isomerisierung auf MFI sind stets Gemische von Xylol Isomeren vorhanden. Aufgrund der sterischen Hinderung von *m*- und *o*-Xylol können diese verglichen mit *p*-Xylol nur sehr langsam in den MFI Poren diffundieren.

Für solche Gemische wird die Transportrate durch Kompetitive Adsorption an der äußeren Oberfläche entscheidend beeinflusst. Zugabe von *m*-Xylol zu einer *p*-Xylol Gasphase wird demzufolge die Oberflächenkonzentration von *p*-xylol aufgrund kompetitiver Adsorption mit *m*-xylol reduzieren und zu einer kleineren Poreneintrittsrate verglichen mit dem Einkomponentensystem führen.

Für Bedingungen bei denen der Poreneintritt von *p*-Xylol schneller als die Desorptionsrate von *m*-xylol ist, blockiert das adsorbierte *m*-Xylol Porenöffnungen für den *p*-Xylol Transport. Da dadurch die Anzahl an Porenöffnungen reduziert wird, verringert sich die Transportrate für den *p*-Xylol Poreneintritt weiter. Da die Aktivierungsenergie für die Desorption von der Oberfläche größer als die des Poreneintritts ist, können Transportlimitierungen durch Temperaturerhöhung verringert werden.

## References

1. Baerlocher, C., L.B. McCusker, and D.H. Olson, *Atlas of zeolite framework types*. 2007: Elsevier.
2. *Database of Zeolite Structures*.
3. *Structure Commission of the International Zeolite Association.*; Available from: <https://europe.iza-structure.org/>.
4. Meier, W. and C. Baerlocher, *Zeolite type frameworks: connectivities, configurations and conformations*, in *Structures and Structure Determination*. 1999, Springer. p. 141-161.
5. Weitkamp, J., *Zeolites and catalysis*. Solid state ionics, 2000. **131**(1-2): p. 175-188.
6. Auerbach, S.M., K.A. Carrado, and P.K. Dutta, *Handbook of Zeolite Science and Technology*. 2003, New York: Marcel Dekker.
7. Payra, P. and P.K. Dutta, *Zeolites: A Primer. Handbook of Zeolite Science and Technology*. 2003: Marcel Dekker, Inc.
8. Degnan, T., G. Chitnis, and P.H. Schipper, *History of ZSM-5 fluid catalytic cracking additive development at Mobil*. Microporous and Mesoporous materials, 2000. **35**: p. 245-252.
9. Tonetto, G., J. Atias, and H. de Lasa, *FCC catalysts with different zeolite crystallite sizes: acidity, structural properties and reactivity*. Applied Catalysis a- General, 2004. **270**(1-2): p. 9-25.
10. García-Martínez, J., et al., *Mesostructured zeolite Y—high hydrothermal stability and superior FCC catalytic performance*. Catalysis Science & Technology, 2012. **2**(5): p. 987-994.
11. Müller, S., et al., *Coke formation and deactivation pathways on H-ZSM-5 in the conversion of methanol to olefins*. Journal of Catalysis, 2015. **325**: p. 48-59.
12. Schulz, H., *“Coking” of zeolites during methanol conversion: Basic reactions of the MTO-, MTP- and MTG processes*. Catalysis Today, 2010. **154**(3-4): p. 183-194.
13. Lesthaeghe, D., et al., *Understanding the Failure of Direct C–C Coupling in the Zeolite-Catalyzed Methanol-to-Olefin Process*. Angewandte Chemie, 2006. **118**(11): p. 1746-1751.

14. Yashima, T., et al., *Alkylation on synthetic zeolites: III. Alkylation of toluene with methanol and formaldehyde on alkali cation exchanged zeolites*. Journal of Catalysis, 1972. **26**(3): p. 303-312.
15. Bellussi, G., et al., *Liquid-phase alkylation of benzene with light olefins catalyzed by  $\beta$ -zeolites*. Journal of Catalysis, 1995. **157**(1): p. 227-234.
16. Taarning, E., et al., *Zeolite-catalyzed isomerization of triose sugars*. ChemSusChem, 2009. **2**(7): p. 625-627.
17. Young, L., S. Butter, and W. Kaeding, *Shape selective reactions with zeolite catalysts: III. Selectivity in xylene isomerization, toluene-methanol alkylation, and toluene disproportionation over ZSM-5 zeolite catalysts*. Journal of Catalysis, 1982. **76**(2): p. 418-432.
18. Mirth, G., J. Cejka, and J.A. Lercher, *Transport and Isomerization of Xylenes over HZSM-5 Zeolites*. J. Catal., 1993. **139**: p. 24-33.
19. Gilot, P., M. Guyon, and B.R. Stanmore, *A review of NO<sub>x</sub> reduction on zeolitic catalysts under diesel exhaust conditions*. Fuel, 1997. **76**(6): p. 507-515.
20. Traa, Y., B. Burger, and J. Weitkamp, *Zeolite-based materials for the selective catalytic reduction of NO<sub>x</sub> with hydrocarbons*. Microporous and mesoporous materials, 1999. **30**(1): p. 3-41.
21. Bernardo, P., E. Drioli, and G. Golemme, *Membrane gas separation: a review/state of the art*. Industrial & engineering chemistry research, 2009. **48**(10): p. 4638-4663.
22. Kusakabe, K., et al., *Formation of a Y-type zeolite membrane on a porous  $\alpha$ -alumina tube for gas separation*. Industrial & engineering chemistry research, 1997. **36**(3): p. 649-655.
23. Riegler, N., *Insulation material*. 1996, Patent.
24. Mukhopadhyaya, P., et al. *Fibre-powder composite as core material for vacuum insulation panel*. in *9th international vacuum insulation symposium, London, UK*. 2009.
25. Fofana, I., et al., *Drying of transformer insulation using zeolite*. IEEE Electrical Insulation Magazine, 2004. **20**(1): p. 20-30.
26. Schöffmann, M., et al., *Speaker with grained zeolite material in deep-drawn foil resonance volume*. 2017, Google Patents.

27. Rose, J.A., *Zeolite bed leach septic system and method for wastewater treatment*. 2003, Google Patents.
28. Shi, J., et al., *Recent advances of pore system construction in zeolite-catalyzed chemical industry processes*. *Chemical Society Reviews*, 2015. **44**(24): p. 8877-8903.
29. Naber, J., et al., *Industrial applications of zeolite catalysis*, in *Studies in surface science and catalysis*. 1994, Elsevier. p. 2197-2219.
30. Yilmaz, B. and U. Müller, *Catalytic applications of zeolites in chemical industry*. *Topics in Catalysis*, 2009. **52**(6-7): p. 888-895.
31. Li, Y., L. Li, and J. Yu, *Applications of zeolites in sustainable chemistry*. *Chem*, 2017. **3**(6): p. 928-949.
32. Chorkendorff, I. and J.W. Niemantsverdriet, *Concepts of modern catalysis and kinetics*. 2017: John Wiley & Sons.
33. Davis, M.E. and R.F. Lobo, *Zeolite and molecular sieve synthesis*. *Chemistry of Materials*, 1992. **4**(4): p. 756-768.
34. Mortier, W., et al., *Bridging and terminal hydroxyls. A structural chemical and quantum chemical discussion*. *The Journal of Physical Chemistry*, 1984. **88**(5): p. 905-912.
35. Loeffler, E., et al., *Study of different states of nonframework aluminum in hydrothermally dealuminated HZSM-5 zeolites using diffuse reflectance infrared spectroscopy*. *Zeolites*, 1990. **10**(4): p. 266-271.
36. Kokotailo, G., et al., *Structure of synthetic zeolite ZSM-5*. *Nature*, 1978. **272**(5652): p. 437-438.
37. Barthomeuf, D., *Zeolite acidity dependence on structure and chemical environment. Correlations with catalysis*. *Materials Chemistry and Physics*, 1987. **17**(1-2): p. 49-71.
38. Barthomeuf, D., *Topology and maximum content of isolated species (Al, Ga, Fe, B, Si,...) in a zeolitic framework. An approach to acid catalysis*. *The Journal of Physical Chemistry*, 1993. **97**(39): p. 10092-10096.
39. Hunger, B., et al., *Characterization of acidic OH groups in zeolites of different types: An interpretation of NH<sub>3</sub>-TPD results in the light of confinement effects*. *The Journal of Physical Chemistry B*, 2002. **106**(15): p. 3882-3889.

40. Weitkamp, J. and L. Puppe, *Catalysis and zeolites: fundamentals and applications*. 2013: Springer Science & Business Media.
41. Janda, A. and A.T. Bell, *Effects of Si/Al Ratio on the Distribution of Framework Al and on the Rates of Alkane Monomolecular Cracking and Dehydrogenation in H-MFI*. Journal of the American Chemical Society, 2013. **135**(51): p. 19193-19207.
42. Uytterhoeven, J.B., L. Christner, and W.K. Hall, *Studies of the hydrogen held by solids. VIII. The decationated zeolites*. The Journal of Physical Chemistry, 1965. **69**(6): p. 2117-2126.
43. Barrer, R.M. and R.P. Townsend, *Transition metal ion exchange in zeolites. Part 1.—Thermodynamics of exchange of hydrated Mn<sup>2+</sup>, Co<sup>2+</sup>, Ni<sup>2+</sup>, Cu<sup>2+</sup> and Zn<sup>2+</sup> ions in ammonium mordenite*. Journal of the Chemical Society, Faraday Transactions 1: Physical Chemistry in Condensed Phases, 1976. **72**: p. 661-673.
44. Weisz, P. and V. Frilette, *Intracrystalline and molecular-shape-selective catalysis by zeolite salts*. The Journal of Physical Chemistry, 1960. **64**(3): p. 382-382.
45. Smit, B. and T.L. Maesen, *Towards a molecular understanding of shape selectivity*. Nature, 2008. **451**(7179): p. 671-678.
46. Menoufy, M., A. Nadia, and H. Ahmed, *Catalytic dewaxing for lube oil production*. Petroleum science and technology, 2009. **27**(6): p. 568-574.
47. Mirth, G. and J.A. Lercher, *On the Role of Product Isomerization for Shape Selective Toluene Methylation over HZSM5*. J. Catal. , 1994. **147**: p. 199-206.
48. Klemm, E., J. Wang, and G. Emig, *A Method for the Determination of Diffusion Coefficients in Product-Shape-Selective Catalysis on Zeolites under Reaction Conditions*. Chem. Eng. Sci. , 1997. **52**: p. 4329-4344.
49. Derouane, E.G., *Shape selectivity in catalysis by zeolites: The nest effect*. Journal of catalysis (Print), 1986. **100**(2): p. 541-544.
50. Sastre, G. and A. Corma, *The confinement effect in zeolites*. Journal of Molecular Catalysis A: Chemical, 2009. **305**(1-2): p. 3-7.
51. Eder, F. and J. Lercher, *On the role of the pore size and tortuosity for sorption of alkanes in molecular sieves*. The Journal of Physical Chemistry B, 1997. **101**(8): p. 1273-1278.

52. Onida, B., et al., *IR evidence that secondary interactions may hamper H-bonding at protonic sites in zeolites*. The Journal of Physical Chemistry B, 2002. **106**(41): p. 10518-10522.
53. Lercher, J.A. and A. Jentys, *Infrared and Raman spectroscopy for characterizing zeolites*. Studies in surface science and catalysis, 2007. **168**: p. 435-476.
54. Cejka, J., et al., *Introduction to zeolite molecular sieves*. 2007: Elsevier.
55. Rabo, J.A. and M.W. Schoonover, *Early discoveries in zeolite chemistry and catalysis at Union Carbide, and follow-up in industrial catalysis*. Applied Catalysis A: General, 2001. **222**(1-2): p. 261-275.
56. Zoubida, L. and B. Hichem, *The Nanostructure Zeolites MFI-Type ZSM5*. Nanocrystals and Nanostructures, 2018: p. 43-62.
57. Flanigen, E.M., et al., *Silicalite, a new hydrophobic crystalline silica molecular sieve*. Nature, 1978. **271**(5645): p. 512-516.
58. Mosallanejad, S., et al., *HCl adsorption on copper-modified ZSM-5: FTIR and DFT study*. The Journal of Physical Chemistry C, 2013. **117**(38): p. 19365-19372.
59. Kim, C.W., N.H. Heo, and K. Seff, *Framework Sites Preferred by Aluminum in Zeolite ZSM-5. Structure of a Fully Dehydrated, Fully Cs<sup>+</sup>-Exchanged ZSM-5 Crystal (MFI, Si/Al= 24)*. Journal of Physical Chemistry C, 2011. **115**(50): p. 24823-24838.
60. Olson, D., et al., *Crystal structure and structure-related properties of ZSM-5*. The Journal of Physical Chemistry, 1981. **85**(15): p. 2238-2243.
61. Tabak, S., F. Krambeck, and W. Garwood, *Conversion of propylene and butylene over ZSM-5 catalyst*. AIChE journal, 1986. **32**(9): p. 1526-1531.
62. EderMirth, G., H.D. Wanzelbock, and J.A. Lercher, *Zeolite induced chemical selectivity during toluene alkylation*. Catalysis by Microporous Materials, 1995. **94**: p. 449-455.
63. Kapteijn, F., et al., *Permeation and separation behaviour of a silicalite-1 membrane*. Catalysis Today, 1995. **25**(3-4): p. 213-218.
64. Kapteijn, F., et al., *Permeation and separation of light hydrocarbons through a silicalite-1 membrane: Application of the generalized Maxwell-Stefan equations*. The Chemical Engineering Journal and The Biochemical Engineering Journal, 1995. **57**(2): p. 145-153.

65. Bordiga, S., et al., *Reactivity of Ti (iv) species hosted in TS-1 towards H<sub>2</sub>O<sub>2</sub>–H<sub>2</sub>O solutions investigated by ab initio cluster and periodic approaches combined with experimental XANES and EXAFS data: a review and new highlights*. Physical Chemistry Chemical Physics, 2007. **9**(35): p. 4854-4878.
66. Vayssilov, G.N., *Structural and physicochemical features of titanium silicalites*. Catalysis Reviews, 1997. **39**(3): p. 209-251.
67. Cavani, F. and J.H. Teles, *Sustainability in catalytic oxidation: an alternative approach or a structural evolution?* ChemSusChem: Chemistry & Sustainability Energy & Materials, 2009. **2**(6): p. 508-534.
68. Bhan, A. and W. Nicholas Delgass, *Propane aromatization over HZSM-5 and Ga/HZSM-5 catalysts*. Catalysis Reviews, 2008. **50**(1): p. 19-151.
69. Al-Yassir, N., M. Akhtar, and S. Al-Khattaf, *Physicochemical properties and catalytic performance of galloaluminosilicate in aromatization of lower alkanes: a comparative study with Ga/HZSM-5*. Journal of Porous Materials, 2012. **19**(6): p. 943-960.
70. Xiao, H., et al., *Mechanistic insight to acidity effects of Ga/HZSM-5 on its activity for propane aromatization*. RSC advances, 2015. **5**(112): p. 92222-92233.
71. Zhang, T., et al., *Selective catalytic reduction of NO with NH<sub>3</sub> over HZSM-5-supported Fe–Cu nanocomposite catalysts: The Fe–Cu bimetallic effect*. Applied Catalysis B: Environmental, 2014. **148**: p. 520-531.
72. Sultana, A., et al., *Tuning the NO<sub>x</sub> conversion of Cu-Fe/ZSM-5 catalyst in NH<sub>3</sub>-SCR*. Catalysis Communications, 2013. **41**: p. 21-25.
73. Manes, M., *Activated carbon adsorption fundamentals*. Encyclopedia of environmental analysis and remediation, 1998. **1**: p. 26-68.
74. Hüffer, T. and T. Hofmann, *Sorption of non-polar organic compounds by micro-sized plastic particles in aqueous solution*. Environmental pollution, 2016. **214**: p. 194-201.
75. Logan, S.R. and D. Wilmer, *Fundamentals of chemical kinetics*. Vol. 10. 1996: Longman London.
76. Kurosawa, H. and A. Yamamoto, *Fundamentals of Molecular Catalysis*. Vol. 3. 2003, Amsterdam: Elsevier.

77. Langmuir, I., *The constitution and fundamental properties of solids and liquids. Part I. Solids*. Journal of the American chemical society, 1916. **38**(11): p. 2221-2295.
78. Atkins, P. and J. De Paula, *Elements of physical chemistry*. 2013: Oxford University Press, USA.
79. Krishna, R., T. Vlugt, and B. Smit, *Influence of isotherm inflection on diffusion in silicalite*. Chemical engineering science, 1999. **54**(12): p. 1751-1757.
80. Chiou, C.T., *Partition and adsorption of organic contaminants in environmental systems*. 2003: John Wiley & Sons.
81. Polanyi, M., *Adsorption of gases (vapors) by a solid non-volatile adsorbent*. Verh. Dtsch. Phys. Ges, 1916. **18**: p. 55-80.
82. Manes, M. and L.J. Hofer, *Application of the Polanyi adsorption potential theory to adsorption from solution on activated carbon*. The Journal of Physical Chemistry, 1969. **73**(3): p. 584-590.
83. Sposito, G., *Derivation of the Freundlich equation for ion exchange reactions in soils*. Soil Science Society of America Journal, 1980. **44**(3): p. 652-654.
84. Umpleby II, R.J., et al., *Application of the Freundlich adsorption isotherm in the characterization of molecularly imprinted polymers*. Analytica Chimica Acta, 2001. **435**(1): p. 35-42.
85. Kärger, J., D.M. Ruthven, and D.N. Theodorou, *Diffusion in Nanoporous Materials*. 2012, Weinheim: Wiley-VCH.
86. Brunauer, S., P.H. Emmett, and E. Teller, *Adsorption of gases in multimolecular layers*. Journal of the American chemical society, 1938. **60**(2): p. 309-319.
87. van Santen, R.A., et al., *Catalysis: an integrated approach*. Vol. 123. 2000: Elsevier.
88. Riazi, M. and R. Gupta, *Coal production and processing technology*. 2015: CRC press.
89. Barzetti, T., et al., *Pyridine and ammonia as probes for FTIR analysis of solid acid catalysts*. Journal of the Chemical Society, Faraday Transactions, 1996. **92**(8): p. 1401-1407.
90. Jacobs, P.A. and C. Heylen, *Active sites in zeolites: III. Selective poisoning of Bronsted sites on synthetic Y zeolites*. Journal of Catalysis, 1974. **34**(2): p. 267-274.

91. Topaloğlu Yazıcı, D. and C. Bilgic, *Determining the surface acidic properties of solid catalysts by amine titration using Hammett indicators and FTIR-pyridine adsorption methods*. Surface and Interface Analysis, 2010. **42**(6-7): p. 959-962.
92. al LAKISS, L., et al., *Probing the Brønsted acidity of the external surface of Faujasite type zeolites*. ChemPhysChem, 2020.
93. Kunkeler, P., R. Downing, and H. Van Bekkum, *The use of bulky molecules as probes for investigating the contributions of the external and internal pore-wall activities of zeolite catalysts*, in *Studies in Surface Science and Catalysis*. 2001, Elsevier. p. 987-1001.
94. Bolis, V., et al., *Adsorption and activation of ethene by zeolite-H-ZSM-5*. Journal of the Chemical Society, Faraday Transactions 1: Physical Chemistry in Condensed Phases, 1980. **76**: p. 1606-1616.
95. Majchrzak-Kucęba, I. and W. Nowak, *A thermogravimetric study of the adsorption of CO<sub>2</sub> on zeolites synthesized from fly ash*. Thermochimica Acta, 2005. **437**(1-2): p. 67-74.
96. Kärger, J., S. Vasenkov, and S.M. Auerbach, *Diffusion in zeolites*. Handbook of Zeolite Science and Technology, 2003: p. 341.
97. Kärger, J., et al., *A new view of diffusion in nanoporous materials*. Chemie Ingenieur Technik, 2010. **82**(6): p. 779-804.
98. Malek, K. and M.-O. Coppens, *Knudsen self-and Fickian diffusion in rough nanoporous media*. The Journal of chemical physics, 2003. **119**(5): p. 2801-2811.
99. Baerns, M., et al., *Technische chemie*. 2013: John Wiley & Sons.
100. Welty, J., G.L. Rorrer, and D.G. Foster, *Fundamentals of momentum, heat, and mass transfer*. 2020: John Wiley & Sons.
101. DEBOER, J.H., *The dynamical character of adsorption*. Vol. 76. 1953: LWW.
102. Ruthven, D.M., M. Eic, and E. Richard, *Diffusion of C<sub>8</sub> Aromatic Hydrocarbons in Silicalite*. Zeolites, 1991. **11**(7): p. 647-653.
103. Skoulidas, A.I. and D.S. Sholl, *Self-diffusion and transport diffusion of light gases in metal-organic framework materials assessed using molecular dynamics simulations*. The Journal of Physical Chemistry B, 2005. **109**(33): p. 15760-15768.
104. Hahn, K., J. Kärger, and V. Kukla, *Single-file diffusion observation*. Physical review letters, 1996. **76**(15): p. 2762.

105. Kärger, J., et al., *Single-file diffusion and reaction in zeolites*. Journal of Catalysis, 1992. **136**(2): p. 283-299.
106. Qi, X., et al., *Adsorptive Nature of Surface Barriers in MFI Nanocrystals*. Langmuir, 2019. **35**(38): p. 12407-12417.
107. Reitmeier, S.J., *Investigation of hydrocarbon transport phenomena on surface modified H-ZSM5 zeolites*. 2009, Technische Universität München.
108. Reitmeier, S., et al., *Influence of postsynthetic surface modification on shape selective transport of aromatic molecules in HZSM-5*. The Journal of Physical Chemistry C, 2009. **113**(34): p. 15355-15363.
109. Reitmeier, S.J., et al., *Enhancement of Sorption Processes in the Zeolite H-ZSM5 by Postsynthetic Surface Modification*. Angew. Chem., Int. Ed. , 2009. **48**: p. 533-538.
110. Song, L., Z.-L. Sun, and L.V. Rees, *Experimental and molecular simulation studies of adsorption and diffusion of cyclic hydrocarbons in silicalite-1*. Microporous and mesoporous materials, 2002. **55**(1): p. 31-49.
111. Song, L., et al., *Investigation of adsorption hysteresis in microporous materials*, in *Studies in Surface Science and Catalysis*. 2004, Elsevier. p. 1797-1803.
112. Yasuda, Y., *Frequency response method for study of the kinetic behavior of a gas-surface system. 1. Theoretical treatment*. The Journal of Physical Chemistry, 1976. **80**(17): p. 1867-1869.
113. Yasuda, Y., *Frequency-response method for investigation of gas-surface dynamic phenomena*. Heterogeneous Chemistry Reviews, 1994. **1**(2): p. 103-124.
114. Tsai, T.C., S.B. Liu, and I. Wang, *Disproportionation and Transalkylation of Alkylbenzenes over Zeolite Catalysts*. Appl. Catal. , 1999. **191**: p. 355-398.
115. Sun, X., et al., *The Role of Acid Strength of Zeolites in Liquid-Phase Alkylation of Benzene with Ethylene*. Catal. Lett. , 2004. **94**: p. 75-79.
116. Ivanova, I.I. and A. Corma, *An in Situ <sup>13</sup>C MAS NMR Study of Toluene Alkylation with Methanol over H-ZSM-11*. Stud. Surf. Sci. Catal., 1995. **97**: p. 27-34.
117. Weisz, P.B., *Molecular Shape Selective Catalysis*. Pure Appl. Chem. , 1980. **52**: p. 2091-2103.
118. Weitkamp, J., et al., *Direct Conversion of Aromatics into a Synthetic Steamcracker Feed using Bifunctional Zeolite Catalysts*. Chem. Commun. , 2000. **13**: p. 1133-1134.

119. Klemm, E., J. Wang, and G. Emig, *A Study of Shape Selectivity in Ethylation/Disproportionation of Ethylbenzene on ZSM-5 Zeolites using a Continuum and a Monte Carlo Method*. Chem. Eng. Sci., 1997. **52**: p. 3173-3182.
120. Csicsery, S.M., *Catalysis by Shape Selective Zeolites-Science and Technology*. Pure Appl. Chem., 1986. **58**: p. 841-856.
121. Krishna, R., *Describing the Diffusion of Guest Molecules Inside Porous Structures*. J. Phys. Chem. C 2009. **113**: p. 19756-19781.
122. Chmelik, C. and J. Kärger, *In situ Study on Molecular Diffusion Phenomena in Nanoporous Catalytic Solids*. Chem. Soc. Rev. , 2010. **39**: p. 4864-4884.
123. Caro, J., et al., *Molecular Mobility Measurement of Hydrocarbons in Zeolites by NMR Techniques*. Adv. Catal., 1993. **39**: p. 351-414.
124. Saint Remi, J.C., et al., *The Role of Crystal Diversity in Understanding Mass Transfer in Nanoporous Materials*. Nature mater., 2016. **15**: p. 401-409.
125. Teixeira, A.R., et al., *2D Surface Structures in Small Zeolite MFI Crystals*. Chem. Mater., 2015. **27**: p. 4650-4660.
126. Teixeira, A.R., et al., *On Asymmetric Surface Barriers in MFI Zeolites Revealed by Frequency Response*. J. Phys. Chem. C, 2014. **118**: p. 22166-22180.
127. Gobin, O.C., et al., *Comparison of the Transport of Aromatic Compounds in Small and Large MFI Particles*. Journal of Physical Chemistry C, 2009. **113**: p. 20435-20444.
128. Snurr, R.Q. and J. Kärger, *Molecular Simulations and NMR Measurements of Binary Diffusion in Zeolites*. J. Phys. Chem. B 1997. **101**: p. 6469-6473.
129. Karger, J. and D.M. Ruthven, *On the Comparison between Macroscopic and NMR Measurements of Intracrystalline Diffusion in Zeolites*. . Zeolites, 1989. **9**: p. 267-281.
130. Shah, D.B., S. Chokchai-Acha, and D.T. Hayhurst, *Measurements of Transport Rates of C<sub>4</sub> Hydrocarbons across a Single-Crystal Silicalite Membrane*. J. Chem. Soc. Faraday Trans. , 1993. **89**: p. 3161-3167.
131. Roque-Matherbe, R. and V. Ivanov, *Study of Diffusion and Counter-Diffusion of Para- and Ortho-Xylene in H-SSZ-24 and H-ZSM-11 zeolites*. Microporous Mesoporous Mater., 2001. **47**: p. 25-38.

132. Brandani, S., M. Jama, and D. Ruthven, *Diffusion, Self-Diffusion and Counter-Diffusion of Benzene and p-Xylene in Silicalite*. Microporous and Mesoporous Materials, 2000. **35**: p. 283-300.
133. Zheng, S., A. Jentys, and J.A. Lercher, *Xylene Isomerization with Surface-Modified HZSM-5 Zeolite Catalysts: An in situ IR Study*. J. Catal. , 2006. **241**: p. 304-311.
134. Niessen, W. and H.G. Karge, *Diffusion of p-Xylene in Single and Binary Systems in Zeolites Investigated by FTIR Spectroscopy*. Microporous Materials, 1993. **1**: p. 1-8.
135. Kolvenbach, R., et al., *A Comparative Study of Diffusion of Benzene/p-Xylene Mixtures in MFI Particles, Pellets and Grown Membranes*. Catal. Today 2011. **168**: p. 147-157.
136. Song, L. and L.V.C. Rees, *Adsorption and Diffusion of Cyclic Hydrocarbon in MFI-Type Zeolites Studied by Gravimetric and Frequency-Response Techniques*. Microporous Mesoporous Mater., 2000. **35**: p. 301-314.
137. Gobin, O.C., et al., *Diffusion Pathways of Benzene, Toluene and p-Xylene in MFI*. . Microporous and Mesoporous Materials, 2009. **125**: p. 3-10.
138. Schreiber, M.W., et al., *Hydrodeoxygenation of Fatty Acid Esters Catalyzed by Ni on Nano-Sized MFI Type Zeolites*. Catal. Sci. Technol., 2016. **6**: p. 7976-7984.
139. Rueden, C.T., J. Schindelin, and M.C. Hiner, *ImageJ2: ImageJ for the Next Generation of Scientific Image Data*. BMC Bioinformatics 2017. **187**: p. 529.
140. Inomata, M., et al., *Benzene-Filled Pore Method: A Method of Measuring External Surface Areas Applicable to Zeolites with Low-to-High Si-to-Al Ratios*. J. Catal., 1986. **100**: p. 264-269.
141. Fu, D., et al., *Highly Oriented Growth of Catalytically Active Zeolite ZSM-5 Films with a Broad Range of Si/Al Ratios*. Angew. Chem., Int. Ed., 2017. **56**: p. 11217-11221.
142. Stavitski, E., et al., *Intergrowth Structure of Zeolite Crystals and Pore Orientation of Individual Subunits Revealed by Electron Backscatter Diffraction/Focused Ion Beam Experiments*. Angew. Chem., Int. Ed., 2008. **47**: p. 5637-5640.
143. Sprung, C. and B.M. Weckhuysen, *Differences in the Location of Guest Molecules within Zeolite Pores As Revealed by Multilaser Excitation Confocal Fluorescence*

- Microscopy: Which Molecule Is Where?* J. Am. Chem. Soc., 2015. **137**: p. 1916-1928.
144. Karwacki, L., et al., *Morphology-Dependent Zeolite Intergrowth Structures Leading to Distinct Internal and Outer-Surface Molecular Diffusion Barriers.* Nature mat., 2009. **8**: p. 959-965.
145. Hendriks, F.C., et al., *Probing Zeolite Crystal Architecture and Structural Imperfections using Differently Sized Fluorescent Organic Probe Molecules.* Chem. – Eur. J., 2017. **23**: p. 6305-6314.
146. Gueudré, L., et al., *Micro-Imaging by Interference Microscopy: A Case Study of Orientation-Dependent Guest Diffusion in MFI-Type Zeolite Host Crystals.* Materials, 2012. **5**: p. 721-740.
147. Ristanovic, Z., et al., *Intergrowth Structure and Aluminium Zoning of a Zeolite ZSM-5 Crystal as Resolved by Synchrotron-Based Micro X-Ray Diffraction Imaging.* Angew. Chem., Int. Ed., 2013. **52**: p. 13382-13386.
148. Fasano, M., et al., *Interplay between Hydrophilicity and Surface Barriers on Water Transport in Zeolite Membranes.* nature com., 2016. **7**: p. 12762-12770.
149. Liu, F., et al., *ZSM-5 Zeolite Single Crystals with b-Axis-Aligned Mesoporous Channels as an Efficient Catalyst for Conversion of Bulky Organic Molecules.* J. Am. Chem. Soc., 2012. **134**: p. 4557-4560.
150. Pham, T.C., H.S. Kim, and K.B. Yoon, *Growth of Uniformly Oriented Silica MFI and BEA Zeolite Films on Substrates.* Science, 2011. **334**: p. 1533-1538.
151. Snyder, M.A. and M. Tsapatsis, *Hierarchical Nanomanufacturing: From Shaped Zeolite Nanoparticles to High-Performance Separation Membranes.* Angew. Chem., Int. Ed., 2007. **46**: p. 7560-7573.
152. Reitmeier, S.J., et al., *Surface Transport Processes and Sticking Probability of Aromatic Molecules in HZSM-5.* J. Phys. Chem. C 2008. **113**: p. 2538-2544.
153. Kim, D., et al., *para-Xylene Ultra-Selective Zeolite MFI Membranes Fabricated from Nanosheet Monolayers at the Air–Water Interface.* Angew. Chem. Int. Ed., 2018. **57**: p. 480-485.
154. Xomeritakis, G. and M. Tsapatsis, *Permeation of Aromatic Isomer Vapors through Oriented MFI-Type Membranes Made by Secondary Growth.* Chem. Mater., 1999. **11**: p. 875-878.

155. Baertsch, C.D., et al., *Permeation of Aromatic Hydrocarbon Vapors through Silicalite-Zeolite Membranes*. J. Phys. Chem., 1996. **100**(18): p. 7676-7679.
156. Bowen, H.J.M., *Tables of interatomic Distances and Configurations in Molecules and Ions*. 1964: Burlington House, London
157. Bellat, J.-P. and M.-H. Simonot-Grange, *Adsorption of Gaseous p-Xylene and m-Xylene on NaY, KY, and BaY Zeolites. Part 2: Modeling. Enthalpies and Entropies of Adsorption*. Zeolites, 1995. **15**: p. 219-227.
158. Mukti, R.R., A. Jentys, and J.A. Lercher, *Orientation of Alkyl-Substituted Aromatic Molecules during Sorption in the Pores of HZSM-5 Zeolites*. Journal of Physical Chemistry C, 2007. **111**: p. 3973-3980.
159. Jentys, A., et al., *Energetic and Entropic Contributions Controlling the Sorption of Benzene in Zeolites*. Microporous and Mesoporous Materials, 2006. **90**: p. 284-292.
160. Weitkamp, J. and L. Puppe, eds. *Catalysis and Zeolites: Fundamentals and Applications*. 1999, Springer Science & Business Media: Berlin Heidelberg.
161. Chen, N.Y., T.F. Degnan Jr, and C.M. Smith, *Molecular Transport and Reaction in Zeolites: Design and Application of Shape Selective Catalysis*. 1994, New York: John Wiley & Sons.
162. Beyer, H., et al., *Catalysis by Microporous Materials*. Vol. 94. 1995, Amsterdam: Elsevier.
163. Haag, W.O., R.M. Lago, and P.B. Weisz, *Transport and Reactivity of Hydrocarbon Molecules in a Shape-Selective Zeolite*. Faraday Discussions of the Chemical Society, 1981. **72**(0): p. 317-330.
164. Haynes, H.W., *Mass Transport Characteristics of Zeolite Cracking Catalysts*. 1978: Department of Energy.
165. Hartmann, M., *Hierarchical Zeolites: A Proven Strategy to Combine Shape Selectivity with Efficient Mass Transport*. Angewandte Chemie International Edition, 2004. **43**(44): p. 5880-5882.
166. Zikanova, A., M. Bülow, and H. Schlotter, *Intracrystalline Diffusion of Benzene in ZSM-5 and Silicalite*. Zeolites, 1987. **7**(2): p. 115-118.
167. Masuda, T., et al., *The Influence of Acid Sites on Intracrystalline Diffusivities within MFI-Type Zeolites*. Microporous and Mesoporous Materials, 1998. **23**(3-4): p. 157-167.

168. Koriabkina, A.O., et al., *Influence of the Acid Sites on the Intracrystalline Diffusion of Hexanes and Their Mixtures within MFI-Zeolites*. Journal of Physical Chemistry B, 2002. **106**(37): p. 9559-9566.
169. Baumgärtl, M., A. Jentys, and J.A. Lercher, *Understanding Elementary Steps of Transport of Xylene Mixtures in ZSM-5 Zeolites*. Journal of Physical Chemistry C, 2018. **123**(13): p. 8092-8100.
170. Wan, Z., et al., *Direct Synthesis of Hierarchical ZSM-5 Zeolite and Its Performance in Catalyzing Methanol to Gasoline Conversion*. Industrial & Engineering Chemistry Research, 2014. **53**(50): p. 19471-19478.
171. Schallmoser, S., et al., *Impact of the local Environment of Brønsted Acid Sites in ZSM-5 on the Catalytic Activity in n-Pentane Cracking*. J. Catal., 2014. **316**: p. 93–102.
172. Maier, S.M., A. Jentys, and J.A. Lercher, *Steaming of Zeolite BEA and its Effect on Acidity: A Comparative NMR and IR Spectroscopic Study*. Journal of Physical Chemistry C, 2011. **115**(16): p. 8005-8013.
173. Tukur, N.M. and S. Al-Khattaf, *Catalytic Transformation of 1,3,5-Trimethylbenzene over a USY Zeolite Catalyst*. Energy & Fuels, 2007. **21**(5): p. 2499-2508.
174. Yokoi, T., et al., *Control of the Al Distribution in the Framework of ZSM-5 Zeolite and its Evaluation by Solid-State NMR Technique and Catalytic Properties*. Journal of Physical Chemistry C, 2015. **119**(27): p. 15303-15315.
175. Pérez-Ramírez, J., et al., *Hierarchical zeolites: enhanced utilisation of microporous crystals in catalysis by advances in materials design*. Chemical Society Reviews, 2008. **37**(11): p. 2530-2542.
176. Kumar, P., et al., *One-dimensional Intergrowths in Two-Dimensional Zeolite Nanosheets and their Effect on Ultra-Selective Transport*. Nature materials, 2020. **19**(4): p. 443-449.
177. Beschmann, K., S. Fuchs, and L. Riekert, *Kinetics of Sorption of Benzene and n-Paraffins in Large Crystals of MFI Zeolites*. Zeolites, 1990. **10**(8): p. 798-801.
178. Baumgärtl, M., A. Jentys, and J.A. Lercher, *Influence of Acid Sites on Xylene Transport in MFI Type Zeolites*. Journal of Physical Chemistry C, 2020. **124**(7): p. 4134-4140.

# List of Figures

Figure 1.1: Selection of secondary building blocks adapted from Baerlocher et al. [1] The corners thereby represent T-atoms, the bonds oxygen bridges. ....	2
Figure 1.2: Selection of industrially important zeolite framework types and the composite building blocks they are built of. [2, 3] .....	3
Figure 1.3: Average pore size of commonly used zeolite frameworks. [2, 3, 6, 7].....	4
Figure 1.4: Turnover frequencies for n-pentane cracking on various zeolites as a function of pore size. Data adapted from [49]. .....	9
Figure 1.5: a) Shift of OH stretching vibrations of SiOH and SiOHA1 (HZSM-5) for adsorption of various molecules. Summarized data from [53, 55]. b) Sterical constrains of pore influencing distance of interaction between benzene and SiOHA1 group. ....	10
Figure 1.6: The MFI framework is built of (I) Type 5-1 SBUs, which form larger composite building blocks (II). Interconnection of these CBBs results in (III) pentasil chains and (VI) layers of tetrahedra. [57].....	11
Figure 1.7: Schematic representation of the MFI framework with straight (blue) and sinusoidal (red) channel. [57] .....	12
Figure 2.1: Langmuir adsorption isotherms for equilibrium constants of 100 (orange), 1000 (blue) and 10000 (green). .....	15
Figure 2.2: Dual site Langmuir adsorption model with sites 1 (orange) and 2 (blue). The concentration of sites is stated as $c_1:c_2 = 3:2$ .....	17
Figure 2.3: Competitive Langmuir adsorption for molecules A and B. A constant partial pressure of B with increasing partial pressure of A is applied. ....	17
Figure 2.4: Nitrogen adsorption isotherm and illustration of surface coverage with increasing adsorbent pressure. Complete pore condensation is not reached for this example. [88].....	22
Figure 3.1: a) Concentration gradient induces flux of molecules along the x-axis (non-equilibrium situation). b) Equal distributed of identical molecules (constant concentration	

along x-axis) with right half molecules labeled (grey). Equal fluxes of labeled and unlabeled molecules in opposite directions canceling out.....	26
Figure 3.2: Schematic representation of <i>p</i> -xylene hopping between local energy minima on a surface.....	30
Figure 3.3: Schematic representation of a surface barrier. Note that the surface barrier thickness <i>l</i> is enlarged for better illustration.....	32
Figure 4.1: Schematic representation of the data acquisition of infrared spectra in rapid scan mode during transport measurements. [107] .....	35
Figure 4.2: Example of time resolved infrared spectra of <i>p</i> -xylene adsorbed on HZSM-5 acquired by time resolved infrared spectroscopy described in Figure 4.1. ....	36
Figure 4.3: Exemplary time resolved concentration profile for <i>p</i> -xylene adsorption on HZSM-5 derived by integration of C-C stretching vibrations of time resolved infrared spectra (Figure 4.2).....	36
Figure 4.4: Modulation (Magnet signal) and pressure response (Baratron signal) for a frequency response experiment with <i>p</i> -xylene sorption on HZSM-5. a) Series of multiple modulations and b) magnification for closer look at the phase lag and amplitude. ....	39
Figure 4.5: Frequency response spectra for crystallites with a half thickness of 250 nm for a) a single transport process with a diffusion coefficient of $1 \cdot 10^{-15} \text{ m}^2\text{s}^{-1}$ and b) two independent transport processes with diffusion coefficients of $D_1=1 \cdot 10^{-14} \text{ m}^2\text{s}^{-1}$ (blue) and $D_2=2 \cdot 10^{-16} \text{ m}^2\text{s}^{-1}$ (orange). The spectra were calculated according to a planar sheet model. ....	41
Figure 4.6: a) Langmuir adsorption isotherm on two distinct sorption sites and desorption curves for sudden pressure drops from $p/p_0=100$ to 0.02 (desorption primarily from site 1) and from $p/p_0=0.02$ to vacuum (desorption primarily from site 2). ....	43
Figure 6.1: Schematic representation of the MFI unit cell (left) and the crystallite model representing the determined ratio of 1 : 1.4 : 1.5 : 1 between x : y : z : h axis and the location of straight and sinusoidal pore openings (right). ....	50
Figure 6.2: Scanning electron microscopy image of the siliceous MFI sample. The white scale bar represents 200 nm.....	54

Figure 6.3: Concentration change profile for <i>p</i> -xylene (calculated from the C–C stretching vibrational bands) adsorbed on siliceous MFI induced by square wave pressure perturbations with a modulation frequency of $1/25 \text{ s}^{-1}$ .....	55
Figure 6.4: a) Change in <i>p</i> -xylene sorption rate during $\pm 4 \%$ volume modulation measured via fast time-resolved infrared spectroscopy as function of the <i>m</i> -xylene partial pressure at constant <i>p</i> -xylene partial pressure of 0.150 mbar. A sample concentration profile used for rate determination is shown in the supporting information (Figure S7.4). b) Adsorption isotherms of <i>m</i> -xylene on siliceous MFI at 373 K measured at constant <i>p</i> -xylene partial pressure of 0.150 mbar. For measuring the <i>m</i> -xylene uptake on the external surface ( <i>m</i> -xylene outside) and inside the channels ( <i>m</i> -xylene inside) separately, the deposition procedure described for diffusion experiments was applied.....	56
Figure 6.5: Frequency response curves for 0.150 mbar <i>p</i> -xylene adsorbed on siliceous MFI at 373 K and the fit with a dual planar sheet model including an additional surface adsorption contribution.....	57
Figure 6.6: a) Out phase functions for siliceous MFI equilibrated with 0.150 mbar <i>p</i> -xylene at <i>m</i> -xylene partial pressures indicated b) Characteristic out phase functions for straight (straight line: $K_1$ ) and sinusoidal channel (dashed line: $K_2$ ) channel pore entrance at <i>m</i> -xylene partial pressures indicated using a dual planar sheet approach. The individual frequency response curves are shown in the supporting information (Figure S7.5). ....	59
Figure 6.7: Overall (filled symbol) as well as channel specific (open symbols) <i>p</i> -xylene sorption rates on Siliceous MFI as function of the number of available pore openings.	62
Figure 6.8: <i>p</i> -Xylene isotherm on siliceous MFI measured (open symbols) at 373 K and fit using a Langmuir type isotherm (full line). A pressure change from 0.144 to 0.156 mbar resulted in concentration change of adsorbed <i>p</i> -xylene on siliceous MFI of $3.1 \mu\text{mol}\cdot\text{g}^{-1}$ .....	63
Figure 6.9: Comparison of straight channel pore entrance rates derived via fast time resolved IR and frequency response method.....	65
Figure 6.10: Siliceous MFI zeolite model with surface adsorbed <i>m</i> -xylene; a) adsorption in straight pore openings, b) sinusoidal pore openings, c) cut sinusoidal pore openings. ....	66

Figure 7.1: Xylene concentration profiles measured by infrared spectroscopy for a) <i>p</i> -xylene transport, b) <i>m</i> -xylene transport and c) <i>p</i> -xylene subtracted by <i>m</i> -xylene transport (pore entrance contribution). .....	79
Figure 7.2: Scanning electron microscopy images of a) Si-MFI b) MFI-27 and c) MFI-45. ....	81
Figure 7.3: a) <i>p</i> -Xylene sorption isotherms for adsorption on Si-MFI (black) and MFI-45 (blue) and MFI-27 (orange) b) Decrease of SiOHAl sites (vibration at 3610 cm <sup>-1</sup> ) on MFI-45 and MFI-27 with <i>p</i> -xylene adsorption. ....	82
Figure 7.4: Illustration of the external surface of an MFI zeolite, indicating the location of the two different sorption sites at 1) the pore opening (PO) and 2) the non-porous section of the external surface. ....	83
Figure 7.5: <i>m</i> -Xylene adsorption isotherms at 323, 343 and 373 K fitted by a dual Langmuir model (contributions for external surface without and with pore openings) for adsorption on a) Si-MFI and b) MFI-27 and c) MFI-45. The colored curves correspond to the <i>m</i> -xylene contribution adsorbed at the pore openings, the black line to the total uptake on the external surface. A direct comparison between MFI-27 and Si-MFI isotherms is included in the supporting information (Figure S5). As higher pressures and temperatures favor <i>m</i> -xylene pore entrances, the range above 1 mbar was not included in the calculations. This is indicated by the dashed line above 1 mbar. ....	84
Figure 7.6: a) Dependency of equilibrium constants on acid site concentration per pore opening and temperature on Si-MFI (square), MFI-45 (circle) and MFI-27 (triangle). Extrapolated values to [BAS] <sub>external</sub> /[PO]=1 are given as open circles. b) van't Hoff plot for equilibrium constants extrapolated to [BAS] <sub>external</sub> /[PO]=1. ....	85
Figure 7.7: Concentration profile for <i>p</i> -xylene adsorbed on Si-MFI (open squares), MFI-45 (open triangles) and MFI-27 (filled circles). Adsorption process induced by square wave pressure perturbations with a modulation frequency of 1/16 s <sup>-1</sup> at a starting pressure of <i>p</i> -xylene of 0.3 mbar and 373 K. ....	86
Figure 7.8: Normalized <i>p</i> -xylene pore entrance rates as a function of <i>p</i> -xylene surface concentration for Si-MFI (orange circles, $k = 0.24 \text{ m}^2 \mu\text{mol} \cdot \text{s}$ ), MFI-45 (black triangles, $k = 0.29 \text{ m}^2 \mu\text{mol} \cdot \text{s}$ ) and MFI-27 (blue squares, $k = 0.35 \text{ m}^2 \mu\text{mol} \cdot \text{s}$ ) at 373 K. ....	87

Figure 7.9: a) Dependence of rate constants on acid site concentration per pore opening and temperature determined from Si-MFI (square), MFI-45 (full circle) and MFI-27 (triangle). Extrapolated values to $[\text{BAS}]_{\text{external}}/\text{PO}=1$ are given as open circles. b) Eyring plot for rate constants extrapolated to $[\text{BAS}]_{\text{external}}/\text{PO}=1$ .....	88
Figure 7.10: Energy profiles for the <i>p</i> -xylene transport into the micropores of MFI zeolites. <i>p</i> -Xylene transport involving a SiOHAl site on the surface (black) and on the purely siliceous material (blue) are included. ....	89
Figure 7.11: Relative increase in pore entrance rate in presence of externally accessible acid sites as function of temperature and pressure. $r_{\text{BAS}}$ is the pore entrance rate for $[\text{BAS}]_{\text{external}}/[\text{PO}]=1$ . A detailed description of the rate calculation is shown in the supporting information. ....	90
Figure 8.1: Scanning electron microscopy images of a) Si-MFI b) MFI-27 and c) Si-MFI/LC (larger crystallite). ....	104
Figure 8.2: Influence of <i>m</i> -xylene partial pressure on <i>p</i> -xylene transport rate for Si-MFI (open symbols) and MFI-27 (orange symbols) at constant <i>p</i> -xylene partial pressure of 0.150 mbar. <i>m</i> -Xylene is located at the external surface due to short exposure time. .	106
Figure 8.3: a) Competitive adsorption isotherm for <i>p</i> -xylene adsorption at the external surface for a constant <i>p</i> -xylene partial pressure of 0.15 mbar at 373 K. The isotherm was calculated with a Langmuir model based on the equilibrium constants derived in section 3.4. b) <i>p</i> -xylene transport rate for constant <i>p</i> -xylene pressure (0.15mbar) as function of the <i>p</i> -Xylene external surface concentration at 373K (combination of Figure 2 and 3a). Dashed lines represent the rate dependence found for the pure <i>p</i> -xylene situation for MFI-27 (orange) and Si-MFI (white). Note that the two points showing the estimated rate dependence on <i>p</i> -xylene for MFI-27 and Si-MFI (dashed lines) are measured without <i>m</i> -xylene. ....	107
Figure 8.4: a) <i>m</i> -Xylene surface adsorption isotherm on Si-MFI (black) fitted with a dual site Langmuir adsorption model including a site at the pore opening (blue) and at the external surface (red) at 373 K. Blue and orange marked areas indicate the pressure range for the two desorption experiments. Concentration profiles for the <i>m</i> -xylene desorption induced by a pressure decrease b) from 0.1 to $10^{-7}$ mbar and c) 5.8 to 1.6 mbar for Si-MFI. ....	109

- Figure 8.5: a) Infrared spectra of MFI-27 (parent material, dashed line) and T<sup>t</sup>BP modified sample (solid line). A slight decrease of the SiOHAl vibration ( $3610\text{ cm}^{-1}$ ) as well as the presence of the tert-butyl species, indicated by C–H and C–C stretching vibrations ( $2900\text{--}3030\text{ cm}^{-1}$  and  $1450\text{--}1510\text{ cm}^{-1}$ , respectively). b) Concentration profile for *p*-xylene adsorbed on the parent (open symbols) and T<sup>t</sup>BP modified sample (filled symbols) from a starting pressure of *p*-xylene of 0.150 mbar. .... 110
- Figure 8.6: *p*-Xylene transport rate at 373 K and in presence of 0.15 mbar *p*-xylene and varying *m*-xylene partial pressures normalized to the concentration of available pore openings as function of the *p*-xylene surface concentration. Dashed lines represent the rate dependence found for the pure *p*-xylene system for MFI-27 (orange) and Si-MFI (black). [180] The corresponding *m*-xylene pressures in mbar are indicated. .... 111
- Figure 8.7: Normalized pore entrance rates vs. *p*-xylene surface concentration for two purely siliceous MFI samples with different concentration of pore openings due to different crystallite size. .... 112
- Figure 8.8: *p*-Xylene isomerization at 453 K and an initial *p*-xylene partial pressure of 4 mbar. a) Concentration profile for *p*-xylene (red), *m*-xylene (blue) and *o*-xylene (green) adsorbed on MFI-27 and b) in the gas phase during the reaction..... 113
- Figure 8.9: a) Evolution of *p*-xylene transport rate with reaction time. b) *p*-Xylene pore entrance rate normalized to the *p*-xylene concentration on the external surface..... 114
- Figure 8.10: Calculated *p*-xylene pore entrance and *m*-xylene desorption times for various temperatures and *p*-xylene pressures. In grey areas the *p*-xylene pore entrance is faster, in orange areas the *m*-xylene desorption. Small numbers on the right side indicate *p*-xylene partial pressures in mbar..... 115

# List of Tables

Table 6.1: Sorption time constants and available pore openings for <i>p</i> -xylene transport into straight and sinusoidal pore openings at varying <i>m</i> -xylene and constant <i>p</i> -xylene (0.150 mbar) partial pressure. ....	61
Table 6.2: Calculated (frequency response) and measured (fast time-resolved IR) <i>p</i> -xylene sorption rates at varying <i>m</i> -xylene and constant <i>p</i> -xylene (0.150 mbar) partial pressure. ....	62
Table 6.3: Changes in the surface adsorption rate derived via statistical thermodynamics, as well as total surface coverages $\theta$ for low (1) and high (2) pressure state during volume modulation. ....	65
Table 7.1: Equilibrium constants for <i>m</i> -xylene adsorption at MFI pore openings for Si-MFI, MFI-45 and MFI-27 as well as a hypothetical sample with $[BAS]_{\text{external}}/[PO]=1$ . 85	85
Table 7.2: Adsorption enthalpies and entropies for <i>p</i> -xylene adsorption at MFI pore openings (PO) with and without acid sites present. ....	86
Table 7.3: Rate constants for <i>p</i> -xylene pore entrance for Si-MFI, MFI-45 and MFI-27 as well as a hypothetical sample with $[BAS]/[PO]=1$ . ....	88
Table 7.4: Apparent and true transition state entropies, enthalpies, and free energies for the <i>p</i> -xylene pore entrance with and without a SiOHAl sites present at the pore opening. ....	88
Table 8.1: Physicochemical properties of investigated samples. ....	104
Table 8.2: Concentration of pore openings for investigated samples. ....	105
Table 8.3: Rate constants and average residence times for <i>m</i> -xylene on the outer surface of Si-MFI. Adsorption rate constants were derived from equilibrium constants according to $K = k_{\text{ads}}/k_{\text{des}}$ . ....	108